

Water: its influence on the formation and crystallization of amorphous calcium carbonate

Thèse N° 9778

Présentée le 18 décembre 2019

à la Faculté des sciences et techniques de l'ingénieur
Laboratoire de la matière molle
Programme doctoral en science et génie des matériaux

pour l'obtention du grade de Docteur ès Sciences

par

Huachuan DU

Acceptée sur proposition du jury

Prof. V. Michaud, présidente du jury
Prof. E. Amstad, directrice de thèse
Prof. H. Cölfen, rapporteur
Prof. M. Niederberger, rapporteur
Prof. F. Stellacci, rapporteur

2019

The true value of a man is not determined by his possession, supposed or real, of
truth, but rather by his sincere exertion to get to the truth.

— Gotthold Ephraim Lessing

To my beloved wife Chenyue and my parents Qiong and Guizhou

Acknowledgements

In this moment, I would like to express my sincere gratitude to many people who have supported me during my PhD.

First, I want to thank my supervisor Prof. Esther Amstad for offering me the chance to have such a wonderful journey. It is her who introduced me to the fascinating field of bio-mineralization. It was great to have her to be my supervisor. During my exploration in this field, she was always willing to help me when I needed. She was very positive and communicated with me in an encouraging way, which was an indispensable comfort and support for me when the project did not go well. She always has a lot of creative ideas that I really admire her for. She taught me so much on writing good scientific papers. She spent many efforts in helping me develop my personal career. Under the guidance of her, I became more confident to become an independent researcher.

I would also thank all the members of SMaL. For me, SMaL is not only a place where I work but also a family that I belong to. Gianluca and Antoine are our first generation of PhDs. They must be given most of the credits for starting an amazing group atmosphere, where every member is very close and kind to each other. Mathias, who is not only my excellent office mate but also best friend. We had many fruitful discussions on science, study, career, family, life, etc. I am surprised that we two share so many common opinions even though we grew up with different cultural backgrounds. I also feel so lucky having the chance to be the group mate and friend of Mercedes, Jui-Chia, Johan, Armend, Bjoern, Aysu, Irvine, Michael, Alvaro, and Matteo. We had many wonderful experiences and happy moments together, which made me feel like home.

Certainly, I want to thank all my excellent collaborators. The beam scientists at PHOENIX beamline in PSI, Dr. Thomas Huthwelker, Dr. Camelia Borca, Dr. Jacinta Xto and Dr. Katja Henzler, remarkably contributed to the synchrotron and *in situ*

FTIR experiments. I especially thank Jacinta, who is one of the only few students who work on biomineralization in Switzerland. I enjoyed our insightful discussions on different topics of biomineralization so much that I was always excited to go to meet her in PSI. I also want to thank Anna Murello and Prof. Francesco Stellacci, whose strong expertise in AFM allowed me to gain crucial information about my ACC particles. An indispensable acknowledgment should be given to all the students that I have supervised, especially Alice Cont, Clémence Courrégelongue and Alan Böhlen. Without the contribution from them, my PhD work cannot be accomplished in a good shape. This work involved various characterization techniques. Luckily, the valuable help and support from Dr. Pierre Mettraux, Dr. Thomas La Grange, Dr. Reuben Yeo, Dr. David Bi, Dr. Arnaud Magrez, Danièle Laub, Fabienne Bobard, Jacques Morisod, Prof. Véronique Michaud, Dr. Adrien Demongeot, Dr. Robin Nigon and Dr. Robin Amacher at EPFL, enables achieving this goal.

Importantly, I would thank all the members of my PhD thesis jury for their insightful discussions and encouraging feedback. I also want to express my acknowledgment to everyone in the biomineralization community. Inspired by them, I felt braver when I independently explored this field during my PhD. I am proud of being the member of this community. Especially, I want to thank Prof. Jim De Yoreo, Dr. Alejandro Fernandez-Martinez, Prof. Helmut Cölfen, Prof. Kato Takashi, Prof. Derk Joester, Prof. Nico Sommerdijk, Prof. Stephan E. Wolf and Dr. Matthias Kellermeier. I highly appreciate their valuable encouragement and insightful discussions. I also acknowledge the feedback from Prof. Michele Ceriotti in my annual presentations. I am grateful to Prof. Harm-Anton Klok for his kind support during my post-doc fellowship application. I would also thank my friends that I meet in Switzerland: Suyi, Youyou, Jing, Xiaoyu, Zhi, Wei, Chaoqun, Justin, Xiao, Xiaopeng, Oliver, Enzo, Vince, Fabio, Gianni. We had many great experiences and memories that essentially decorate the life of my PhD.

Mainly, I would thank my parents Qiong and Guizhou. It is not easy for them to geographically stay so far from their only child. But they have been always encouraging me to pursue my dream wherever I am. Without their love, devotion and understanding, I could not even have had the chance to start my journey here. I am also very grateful to the parents of my wife, Angela Hongzhen and Claude. It was so lucky for me to be part of their family. With their kindness, wisdom and warm heart, they are a great example worth learning in my life. Last but not the least, I would like to thank my beloved wife Chenyue. The best achievement that I have made during my PhD is that she married to me. She was like a light in the dark shining her love into my life.

She was always the source of my positive energy, happiness, and courage. With her love and support, I am confident to meet any challenges in my life.

Abstract

Nature produces CaCO_3 -based materials that display fascinating mechanical properties. These properties are a result of the exquisite control over the formation of CaCO_3 crystals that nature possesses. Such a high level of control is likely achieved, at least in parts, by controlling the crystallization of CaCO_3 via a transient phase, amorphous CaCO_3 (ACC), with certain soluble additives and insoluble organic scaffolds present in living organisms. Inspired by the excellent properties of natural CaCO_3 -based materials, a lot of research has been devoted to the fabrication of synthetic counterparts with similar properties. Yet, we are far from obtaining the same degree of control over the properties of these synthetic materials. A contributing reason for this inferior control is our incomplete understanding of the influence of the processing conditions, soluble additives, and insoluble scaffolds on the formation of CaCO_3 and thereby the composition, structure and properties of resulting materials.

This thesis is devoted to gaining a better understanding of the early stages of the CaCO_3 formation. To achieve this goal, we introduce a new, organic solvent-free method to quench this process with a high temporal resolution. We produce ACC particles using a microfluidic spray-dryer and characterize them with different techniques. This method allows us to demonstrate that the amount of mobile water contained in ACC particles increases during their growth. As a result of the higher amount of mobile water, larger particles display a lower kinetic stability against the temperature-induced crystallization than smaller counterparts. We also reveal that certain additives reduce the amount of mobile water contained in ACC particles, thereby increasing their kinetic stability if exposed to elevated temperatures. To study the influence of additives on the kinetic stability of ACC against crystallization in more detail, we expose ACC particles functionalized with different additives to a humid environment or elevated pressures. We monitor the evolution of the structure and degree of hydration of these ACC particles during their crystallization. We show that the humidity-induced crystal-

lization of ACC follows a distinctly different pathway than the pressure-induced one. In both pathways, the amount of water and its mobility that depends on its interaction strength with additives can influence the crystallization kinetics of ACC. The resulting CaCO_3 crystals display a difference in their size, morphology, orientation, and structure. To process ACC particles into bulk CaCO_3 -based materials that possess similar mechanical properties to natural ones, insoluble organic scaffolds that offer a control over the local composition and structures of these materials across multiple length scales are typically required. To open up new possibilities of achieving this goal, we develop a new method to fabricate two dimensional (2D) structured hydrogel sheets. These 2D structured hydrogel sheets are composed of self-assembled, crosslinked hexagonal prismatic hydrogel particles. Using this method, we can vary the microscale structure and composition of these hydrogel sheets with the size, composition and arrangement of individual particles, their surface morphology with the polymerization conditions, and their mechanical properties with the crosslink density.

Keywords: *bio-inspired materials, CaCO_3 , ACC, crystallization, water, soluble additives, insoluble organic scaffolds.*

Résumé

La nature produit des matériaux à base de CaCO_3 qui présentent des propriétés mécaniques fascinantes. Ces propriétés sont le résultat d'un contrôle exquis sur la formation des cristaux de CaCO_3 que la nature possède. Un tel niveau élevé de contrôle est probablement atteint, au moins en partie, en contrôlant la cristallisation du CaCO_3 via une phase transitoire, le CaCO_3 amorphe (ACC), avec certains additifs solubles et des échafaudages organiques insolubles présents dans les organismes vivants. Inspiré par les excellentes propriétés des matériaux naturels à base de CaCO_3 , de nombreuses recherches ont été consacrées à la fabrication d'équivalents synthétiques aux propriétés similaires. Pourtant, nous sommes loin d'obtenir le même degré de contrôle sur les propriétés de ces matériaux synthétiques. Une des raisons de ce contrôle inférieur est notre compréhension incomplète de l'influence des conditions de transformation, des additifs solubles et des échafaudages insolubles sur la formation du CaCO_3 et donc sur la composition, la structure et les propriétés des matériaux obtenus.

Cette thèse est consacrée à une meilleure compréhension des premières étapes de la formation du CaCO_3 . Pour atteindre cet objectif, nous introduisons une nouvelle méthode sans solvant organique pour éteindre ce processus avec une résolution temporelle élevée. Nous produisons des particules ACC à l'aide d'un atomiseur microfluidique et les caractérisons avec différentes techniques. Cette méthode nous permet de démontrer que la quantité d'eau mobile contenue dans les particules ACC augmente pendant leur croissance. En raison de la plus grande quantité d'eau mobile, les particules plus grosses présentent une stabilité cinétique plus faible contre la cristallisation induite par la température que les particules plus petites. Nous révélons également que certains additifs réduisent la quantité d'eau mobile contenue dans les particules de ACC, augmentant ainsi leur stabilité cinétique en cas d'exposition à des températures élevées. Pour étudier plus en détail l'influence des additifs sur la stabilité cinétique de l'ACC contre la cristallisation, nous exposons des particules

d'ACC fonctionnalisées avec différents additifs à un environnement humide ou à des pressions élevées. Nous surveillons l'évolution de la structure et du degré d'hydratation de ces particules ACC pendant leur cristallisation. Nous montrons que la cristallisation induite par l'humidité de l'ACC suit une voie nettement différente de celle induite par la pression. Dans les deux voies, la quantité d'eau et sa mobilité qui dépend de sa force d'interaction avec les additifs peuvent influencer la cinétique de cristallisation du ACC. Les cristaux CaCO_3 résultants présentent une différence en leur taille, morphologie, orientation et structure. Pour transformer les particules ACC en matériaux en vrac à base de CaCO_3 qui possèdent des propriétés mécaniques similaires à celles des matériaux naturels, des échafaudages organiques insolubles qui permettent de contrôler la composition et les structures locales de ces matériaux sur plusieurs échelles de longueur sont généralement nécessaires. Afin d'ouvrir de nouvelles possibilités pour atteindre cet objectif, nous développons une nouvelle méthode de fabrication de feuilles d'hydrogel structurées en deux dimensions (2D). Ces feuilles d'hydrogel 2D structurées sont composées de particules d'hydrogel prismatiques hexagonales réticulées et auto-assemblées. En utilisant cette méthode, nous pouvons varier la structure microscopique et la composition de ces feuilles d'hydrogel avec la taille, la composition et la disposition des particules individuelles, leur morphologie de surface avec les conditions de polymérisation, et leurs propriétés mécaniques avec la densité de réticulation.

Mots-clés : *matériaux inspirés du bio, CaCO_3 , ACC, cristallisation, eau, additifs solubles, échafaudages organiques insolubles.*

Contents

1	Introduction	1
1.1	Formation of ACC	4
1.2	Structure and hydration of ACC	9
1.2.1	Characterizations of the structure of ACC	10
1.2.2	Influence of the hydration of ACC on its structure	14
1.3	Crystallization of ACC	16
1.3.1	Solid-state transformation	17
1.3.2	Dissolution-reprecipitation	20
1.4	Influence of soluble additives	23
1.4.1	Magnesium ions	23
1.4.2	Other low molecular weight additives	27
1.4.3	High molecular weight additives	30
1.5	Influence of insoluble organic scaffolds	33
2	Materials and Methods	37
2.1	Materials	38
2.2	Studying the formation and crystallization of ACC using a spray dryer	39
2.2.1	Production of ACC particles using a spray dryer	39
2.2.2	Characterizations of as-produced ACC particles	41
2.2.3	Dehydration and crystallization of ACC particles	42
2.2.4	Electron beam-induced decomposition of ACC particles	44
2.3	Studying the influence of additives on the humidity- and pressure- induced crystallization of ACC	45
2.3.1	Production of ACC particles using a bulk solution method	45
2.3.2	Characterization of as-produced ACC particles	46
2.3.3	Pressure-induced crystallization of ACC particles	47
2.3.4	Humidity-induced crystallization of ACC particles	47
2.4	Fabricating 2D hexagonal prismatic granular hydrogel sheets	48
2.4.1	Production of drops	48

Contents

2.4.2	Self-assembly of hydrogel microparticles	49
2.4.3	Self-assembly and polymerization of drops	50
2.4.4	Characterizations	51
3	Influence of the Formation Time on the Degree of Hydration and Stability of ACC	53
3.1	Introduction	54
3.2	Results	56
3.2.1	Production of ACC particles through spray-drying	56
3.2.2	Influence of the formation time on the degree of hydration of ACC particles	57
3.2.3	Mobility of water contained in ACC particles	64
3.2.4	Influence of mobile water on the stability of ACC particles . . .	67
3.2.5	Influence of poly(acrylic acid) on the stability of ACC particles	69
3.3	Discussion	71
3.4	Conclusion	73
4	Influence of the Additives on the Humidity- and Pressure- Induced Crystallization of ACC	75
4.1	Introduction	76
4.2	Results	78
4.2.1	Synthesis and characterization of ACC particles	78
4.2.2	Humidity-induced crystallization kinetics	80
4.2.3	Crystals obtained from the humidity-induced crystallization .	88
4.2.4	Pressure-induced crystallization kinetics	90
4.2.5	Crystals obtained from the pressure-induced crystallization .	97
4.3	Discussion	98
4.3.1	Kinetic stability of ACC	98
4.3.2	Size, morphology, orientation and structure of CaCO ₃ crystals	100
4.4	Conclusion	102
5	Fabrication of 2D Hexagonal Prismatic Granular Hydrogel Sheets	105
5.1	Introduction	106
5.2	Results and Discussion	107
5.2.1	Fabrication of granular hydrogel sheets	107
5.2.2	Mechanical properties of hydrogel sheets	111
5.2.3	Structure, morphology and composition of hydrogel sheets . .	114

5.3 Conclusion	117
6 Conclusion and Outlook	119
Appendix A Abbreviations	123
Appendix B Symbols	127
Appendix C List of Figures	131
Appendix D Curriculum Vitae	135
Bibliography	139

1 Introduction

* * * * *

This chapter is adapted from our review papers entitled: **(a)** “Water: How does it influence the CaCO_3 formation?,” authored by H. Du and E. Amstad, and published in *Angewandte Chemie International Edition*, May 2019,[1] and **(b)** “Nacre-inspired Hard and Tough Materials,” authored by H. Du, U. Steiner, and E. Amstad, and published in *CHIMIA International Journal for Chemistry*, vol. 73, pp. 29–34, Feb. 2019.[2]

* * * * *

In this chapter, we provide an overview over the current understanding of the influence of processing conditions, soluble additives, and insoluble organic scaffolds on the different stages of the CaCO_3 formation. In the first part of this chapter, we describe different formation and crystallization mechanisms of ACC that have been proposed. Within this framework, we relate different processing conditions to the structure, hydration, crystallization kinetics of ACC and hence, the structure and morphology of the resulting crystals. In the second part of this chapter, we summarize the influence of soluble additives and insoluble scaffolds on the formation of CaCO_3 .

Contents

1.1	Formation of ACC	4
1.2	Structure and hydration of ACC	9
1.2.1	Characterizations of the structure of ACC	10
1.2.2	Influence of the hydration of ACC on its structure	14
1.3	Crystallization of ACC	16
1.3.1	Solid-state transformation	17
1.3.2	Dissolution-reprecipitation	20
1.4	Influence of soluble additives	23
1.4.1	Magnesium ions	23
1.4.2	Other low molecular weight additives	27
1.4.3	High molecular weight additives	30
1.5	Influence of insoluble organic scaffolds	33

Nature fabricates biomineral-based materials with a fascinating combination of properties from a limited number of elements.[3] This wide range of properties that can be accessed by nature is enabled by its tight control over the hierarchical structure and local composition of biominerals.[4, 5] A prominent example of biominerals that nature uses to build exceptionally strong and tough materials is CaCO_3 . Strong and tough CaCO_3 -based materials, such as nacre, can be formed by nature because it possesses an exquisite control over the timing, orientation, size, and morphology of the forming CaCO_3 . [6–10] Moreover, it can precisely control the structure of CaCO_3 even though numerous polymorphs, including an amorphous form, three anhydrous, and three hydrated crystalline forms exist.[11] This level of control is likely in parts related to the crystallization pathway of CaCO_3 and the ability of certain soluble additives and insoluble organic scaffolds present in natural organisms to influence it.[6–10]

Inspired by the fascinating properties of natural CaCO_3 -based materials, a lot of research has been devoted to gaining a better understanding of the crystallization pathway of CaCO_3 in nature.[14–17] It has been suggested that these CaCO_3 crystals form via ACC phases that act as transient precursors. In many organisms such as the sea urchins,[12, 14, 15, 17–19] crayfishes,[20, 21] corals,[22] and gastropods,[23] these transient precursors are stored in designated reservoirs that serve as a tempo-

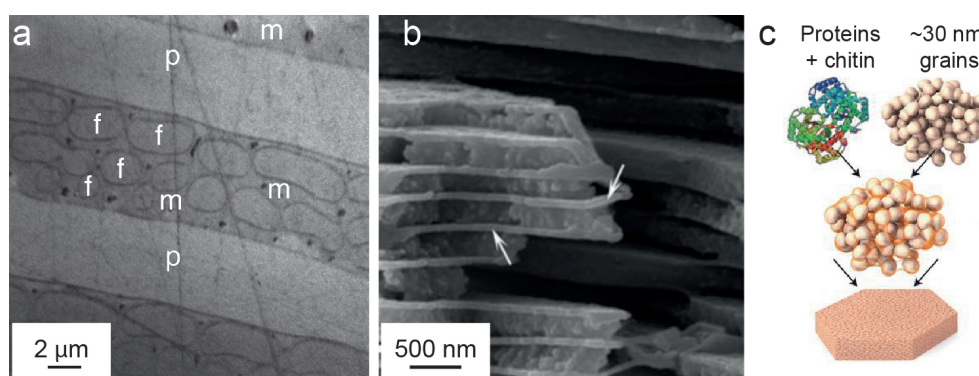


Figure 1.1 – Examples of natural CaCO_3 -based materials. (a) Polarized light microscopy image of a cross section of a sea urchin tooth, which is composed of plates (p), fibers (f), and polycrystalline matrix (m). Gray levels of the image correspond to different angles between the linear polarization vector and the c -axis of CaCO_3 crystals.[12] (b) SEM image of nacre contained in cephalopod *N. pompilius* with arrows pointing to the organic interlayers.[13] (c) Schematic illustration of the composition and structure of the platelets made of nano-crystalline aragonite grains that are separated by β -chitin and acidic proteins.[5]

ral storage of Ca^{2+} ions. They are transported to the desired location before being rapidly transformed into CaCO_3 crystals. This crystallization pathway usually results in CaCO_3 crystals that display a well-defined orientation. For example, the calcite crystals that form in the sea urchin teeth all have the same orientation, as shown in Figure 1.1a.[12] This preferential orientation is crucial for the mechanical strength of these teeth.[19] Moreover, the crystallization pathway via ACC precursors allows certain organisms to rapidly fabricate or repair load-bearing structures on demand. For example, freshwater crayfish usually store protein-stabilized ACC in their gastroliths and use it to build their exoskeleton during molting.[20, 21]

The presence of soluble additives and insoluble organic scaffolds can significantly influence the crystallization process of CaCO_3 via the ACC pathway such that they offer control over the local composition and hierarchical structure of the resulting natural CaCO_3 -based materials.[8, 9, 16] As a result, they enable the outstanding mechanical properties observed in many natural CaCO_3 -based materials.[5, 8, 19] An illustrative, well-studied example is nacre, one of the toughest known biomaterials.[4, 5, 24] Indeed, nacre has been shown to form through the ACC pathway.[23] It is composed of layered platelets made of aragonite, one of the metastable anhydrous crystalline CaCO_3 polymorphs, that are interspaced with thin organic layers composed of insoluble β -chitin and silk fibroins, as shown in Figure 1.1b.[5, 13, 23] Each platelet is

made of aragonite nano-grains that all possess the same orientation and are separated by β -chitin and soluble acidic proteins, as shown in Figure 1.1c.[5, 25] The presence of soluble additives and insoluble organic scaffolds is crucial for the mechanical properties of nacre: They enable plastic deformation of aragonite platelets if subjected to mechanical loads, thereby significantly increasing their fracture toughness.[4, 5, 24, 26, 27]

These examples hint at the importance of the crystallization route of CaCO_3 crystals via ACC precursors and the presence of soluble additives and insoluble organic scaffolds for the mechanical properties of these materials. However, how nature uses additives and organic scaffolds to control the formation of CaCO_3 , including the formation, stabilization, and crystallization of ACC, as well as the composition, size, structure, morphology, and properties of the resulting crystals, is not fully understood.[8, 9] This incomplete understanding prevents us from gaining a similar degree of control over the structure and hence properties of synthetic CaCO_3 -based counterparts.

To gain a better understanding of the CaCO_3 formation, CaCO_3 crystals have been produced in the laboratory where processing conditions have been systematically varied in the presence and absence of additives or organic scaffolds. Particular attention has been paid to the influence of the formation time, the solute concentration, pH, temperature, solvent, and additives present in the solutions, and the surface chemistry and confinement of organic scaffolds during the formation of CaCO_3 . All these parameters have been demonstrated to influence different stages of the CaCO_3 formation, thereby affecting the composition, structure, morphology, and properties of the resulting crystals, as summarized below.

1.1 Formation of ACC

In synthetic systems, CaCO_3 is produced through precipitation reactions occurring between Ca^{2+} and CO_3^{2-} ions. The rate at which CaCO_3 forms depends on the production methods. A fast method to produce CaCO_3 is direct mixing of an aqueous solution containing Ca^{2+} ions with one containing CO_3^{2-} ions.[28–31] The reaction rate can be reduced by slowing down the diffusion of Ca^{2+} and CO_3^{2-} ions. This can be achieved, for example, by placing a membrane[32–34] or hydrogel plug[35–37] between one solution containing Ca^{2+} ions and the other containing CO_3^{2-} ions. Similarly, the reaction rate is slowed down if CO_3^{2-} ions are slowly generated in a Ca^{2+} -containing

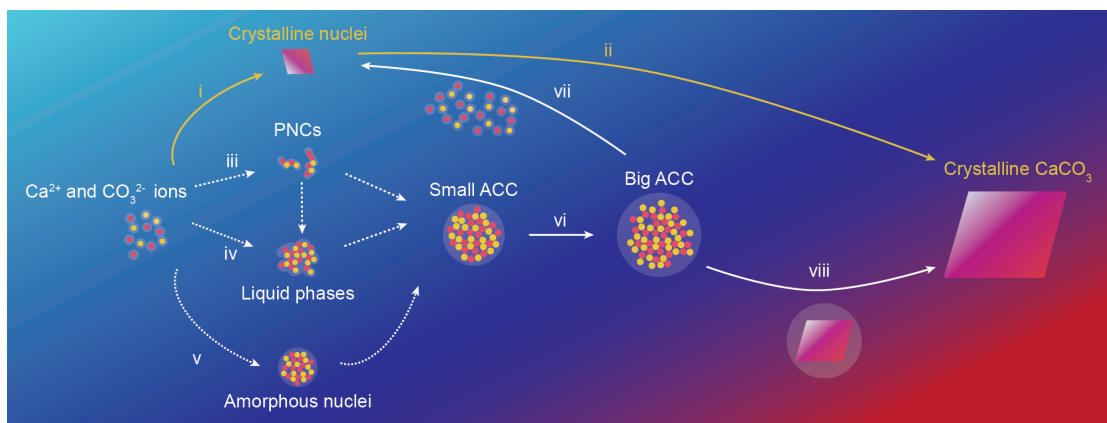


Figure 1.2 – Schematic illustration of proposed mechanisms of CaCO₃ formation. CaCO₃ is most often formed from aqueous solutions containing Ca²⁺ and CO₃²⁻ ions. (i, ii) Crystalline CaCO₃ nuclei can form and grow into big crystals through ion-by-ion attachment following the classical nucleation theory (CNT), if the solutions are supersaturated with respect to any crystalline CaCO₃ phase but undersaturated with respect to that of ACC. However, in most synthetic systems, the solutions are supersaturated also with respect to ACC such that the first phase that forms is typically ACC. ACC particles can form through different mechanisms: (iii) Counter ions associate with each other such that they form highly hydrated chain-like ion clusters, so-called prenucleation clusters (PNCs). PNCs subsequently aggregate, thereby forming liquid phases or small ACC particles. (iv) An aqueous solution containing Ca²⁺ and CO₃²⁻ ions undergoes a spinodal or binodal liquid-liquid phase separation to form a solute-rich liquid phase where ACC particles form through dehydration of the liquid phase or nucleation from the liquid phase. (v) ACC nuclei directly form in the aqueous solution. (vi) The formed small ACC particles grow until they transform into crystals. This transformation can occur through a (vii) dissolution-reprecipitation mechanism if ACC is in contact with free water or (viii) solid-state transformation if ACC is not in contact with free water.

solution from other carbon sources. Carbonate ions can be formed from gaseous CO₂ that is directly introduced into a Ca(OH)₂-containing aqueous solution to precipitate CaCO₃. [38–41] Similarly, carbonate ions can be continuously produced for example through the decomposition of ammonium carbonate. [42–44] Another commonly used route to slowly produce CaCO₃ is the Kitano method where an aqueous solution saturated with Ca(HCO₃)₂ is stored in an open vial. During the storage of this solution, Ca(HCO₃)₂ decomposes into CaCO₃ by releasing CO₂. [45–48].

In these production processes, CaCO₃ crystals can form through different pathways, as schematically summarized in Figure 1.2. If the concentration of Ca²⁺ and CO₃²⁻ ions in the solutions are sufficiently low such that the solutions are supersaturated

Introduction

with respect to any crystalline CaCO_3 phase but undersaturated with respect to ACC, the formation of CaCO_3 crystals usually follows the classical nucleation and growth pathway.[49–51] In this case, crystalline CaCO_3 nuclei form and subsequently grow into larger crystals via an ion-by-ion attachment process. However, in most synthetic systems, the solutions are supersaturated with respect to ACC such that the first phase that forms is typically ACC.[30, 52–55] The mechanisms of the ACC formation are still debated and most likely depend on the exact processing conditions.[56–59] Different types of intermediate species, such as PNCs and liquid precursors have been reported to precede the ACC formation, as summarized in Figure 1.3.[46, 56, 60–62] Prenucleation clusters have been observed in undersaturated and supersaturated solutions using titration experiments, as exemplified in Figure 1.3a.[60] In addition, clusters with a well-defined diameter of around 2 nm have been observed with analytical ultracentrifugation (AUC),[60] cryogenic transmission electron microscopy (cryo-TEM),[48] and small angle X-ray scattering (SAXS).[63, 64] These experimental findings are supported by molecular dynamics (MD) simulations that indicate that PNCs are dynamically ordered liquid-like oxyanion polymers (DOLLOPs) composed of alternating Ca^{2+} and CO_3^{2-} ions, as shown in Figure 1.3b.[65]

Experiments and simulations suggest that the formation of PNCs, their stability and dynamic behavior is strongly influenced by water molecules that are associated with these clusters.[65, 66] Based on these observations, it was suggested that ACC forms through the aggregation of PNCs following a non-classical route.[56, 60] However, more recent experimental studies and MD simulations do not provide evidence for the existence of significant amounts of PNCs.[57, 67, 68] Even if PNCs were present under certain experimental conditions, their role in the formation of ACC requires further clarification.[57] For example, these intermediate clusters have originally been proposed to be thermodynamically stable and decrease the nucleation barrier for the formation of CaCO_3 crystals.[60] This contrasts with more recent work indicating that the height of the nucleation barrier increases if PNCs are thermodynamically stable.[57, 69]

Early stages of the CaCO_3 formation are often accompanied by the observation that certain liquid-like precipitates form, as shown in Figure 1.3c.[40, 44, 46, 61] These precipitates have been reported to be a result of a spinodal or binodal liquid-liquid phase separation that occurs over a range of temperatures and solute concentrations, as schematically shown in Figure 1.3d.[46, 62, 70] Recently, this liquid-liquid phase separation was suggested to form through the aggregation of PNCs, which was accom-

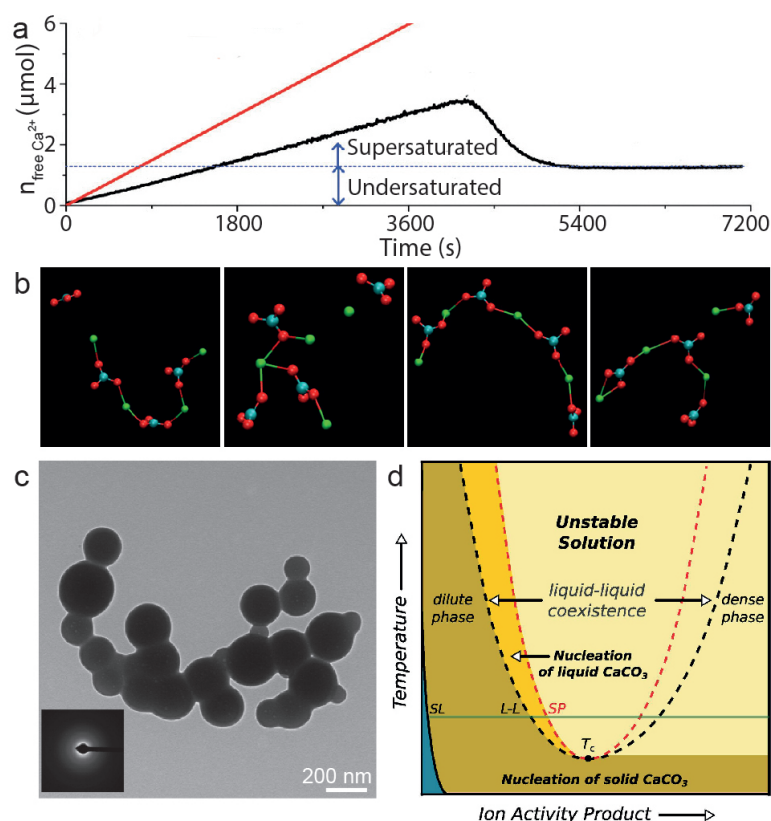


Figure 1.3 – Formation of ACC through non-classical routes. (a) Evolution of the amount of free Ca^{2+} ions measured with a calcium ion-selective electrode when an aqueous solution containing 10 mM CaCl_2 is added to a carbonate buffer at pH = 9.25 at a rate of $10 \mu\text{L}\cdot\text{min}^{-1}$, indicated in black. The total amount of Ca^{2+} ions added to the solution is indicated in red. These results suggest that a significant amount of Ca^{2+} ions is bound by CO_3^{2-} ions to form PNCs both, in solutions that are undersaturated and supersaturated with respect to ACC.[60] (b) Examples of the structures of the PNCs composed of four pairs of Ca^{2+} and CO_3^{2-} ions obtained with MD simulations. Calcium atoms are indicated in green, carbon atoms in blue, and oxygen atoms in red.[65] (c) Cryo-TEM image of liquid-like CaCO_3 phases obtained by freezing a levitated drop composed of a saturated $\text{Ca}(\text{HCO}_3)_2$ solution with liquid ethane.[46] (d) Phase diagram of aqueous solutions containing Ca^{2+} and CO_3^{2-} ions. The solubility of all crystalline CaCO_3 polymorphs is approximated to be the same and indicated as SL. The liquid-liquid coexistence region is indicated by the L-L line, the spinodal decomposition region by the SP line.[62]

panied by a reduction in the mobility of water as measured with THz spectroscopy.[71] The solute-rich liquid phase, which corresponds to the liquid-like precipitates, can be stabilized with additives including Mg^{2+} , [72] poly(aspartic acid) (PAsp), [44, 71, 73] poly(acrylic acid) (PAA), [71] and certain proteins such as ovalbumin. [74] However, how such solute-rich liquid phases transform into ACC is still unknown. A recent study suggested that the solute-rich liquid phase is composed of an assembly of polymer-stabilized ACC nanoclusters. Because of the small sizes of these clusters and their repulsive surfaces, ACC nanoclusters macroscopically display a liquid-like behavior. [75] These results suggest that the liquid-like phase is essentially a variant of ACC particles encompassing a high amount of water, well in agreement with previous reports that observed different types of ACC with different hydration. [31, 40, 76, 77] From these observations, it is questionable if the introduction of a liquid-liquid phase separation that precedes the ACC formation is necessary to describe the early stages of the CaCO_3 formation.

Several studies suggest that the ACC formation can be described using the CNT. [68, 78] The preferential formation of the ACC phase over its crystalline counterparts during the early stages of the CaCO_3 formation might be thermodynamically driven: MD simulations indicate that the free energy of ACC particles whose diameters do not exceed a few nanometers is below that of their crystalline counterparts. [79, 80] Hence, ACC is the thermodynamically most stable phase during early stages of the CaCO_3 formation. A contributing reason for the lower free energy of the amorphous phase in small particles is its lower surface energy that is approximately $0.33 \text{ J}\cdot\text{m}^{-2}$. [81] If ACC particles are sufficiently small, such that their surface-to-volume ratio is high, the lower surface energy outweighs the higher bulk energy of the amorphous phase compared to any of the crystalline ones. [82] Molecular dynamics simulations suggest that the thermodynamic stability of ACC phases might be further increased by water that is incorporated in ACC phases and decreases their bulk free energy. [80] The preferential formation of ACC can also be kinetically driven: [8] The lower surface energy of ACC [81] results in a smaller energy barrier for nucleation, thereby accelerating the nucleation of the amorphous phase. [82] The faster formation of small amorphous particles compared to crystalline counterparts is supported by MD simulations. [80, 83]

Small ACC nanoparticles with diameters of a few nm rapidly grow or agglomerate into bigger ones. [68, 80, 84, 85] This growth or agglomeration reduces their surface-to-volume ratio such that, at some point, the free energy of ACC particles is expected to exceed that of the crystalline polymorphs. [80] The higher free energy of the ACC

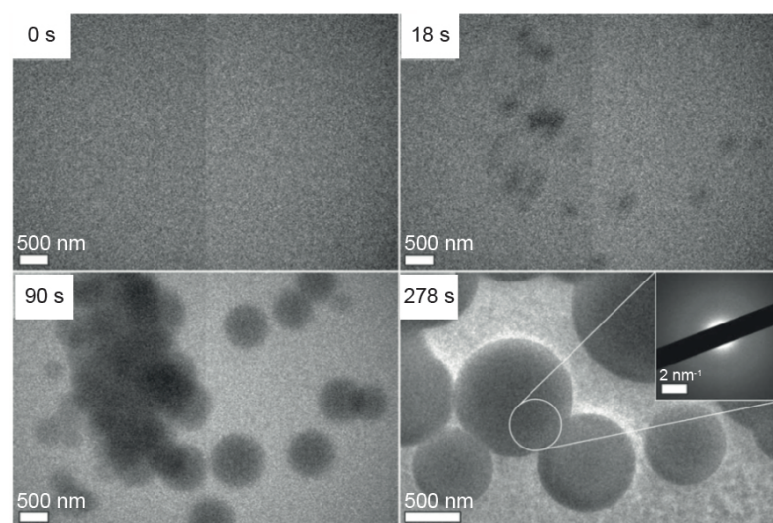


Figure 1.4 – Growth of ACC particles in aqueous solutions. Time-lapse TEM images of the growth of ACC particles obtained with *in situ* liquid cell TEM.[31]

phase is supported by calorimetric measurements that neglect the small entropy contribution. For example, the enthalpy of ACC particles with diameters above 45 nm is $3 \text{ to } 15 \pm 3 \text{ kJ} \cdot \text{mol}^{-1}$ higher than that of calcite, indicating that ACC particles of these sizes are metastable.[28, 86–88] Despite their metastability, ACC particles can still grow into particles with diameters reaching up to several μm within only a few seconds to minutes, as shown in Figure 1.4.[29, 31, 43, 53, 89] However, the driving forces for the growth of ACC particles are still unknown. Interestingly, the presence of ACC particles possessing different hydrations was recently observed during their formation using *in situ* liquid cell transmission electron microscopy (TEM).[31] Whether the hydration of ACC influences its formation and growth remains to be determined.

1.2 Structure and hydration of ACC

The formation of ACC is influenced by processing conditions including the solute concentration,[62, 70, 78, 85] pH,[60, 68] temperature,[62, 68, 70, 78] solvent,[90] and confinement.[91] These conditions also influence the structure and hydration of the resulting ACC particles.[76, 80, 90, 92–94] To investigate how processing conditions influence the structure and hydration of ACC, a thorough characterization of these parameters is key.[76, 95, 96] A variety of techniques that are most commonly used to characterize the structure of ACC are summarized here. These techniques enabled more detailed information of the local structure of ACC and its correlation with the

hydration of ACC.

1.2.1 Characterizations of the structure of ACC

Amorphous particles do not possess any long-range order such that they do not display distinct diffraction peaks if characterized with light, electron beams, and X-rays.[16, 92] This feature is distinctly different from crystals and allows to experimentally easily identify the amorphous structure of particles, for example using X-ray diffraction (XRD) where diffusive and broad peaks are observed.[76, 87] The amorphous structure of CaCO_3 particles can also be characterized on a single particle level using select area electron diffraction (SAED) in TEM.[92]

Complementary information on the structure of CaCO_3 particles and their composition can conveniently be extracted from vibrational spectroscopy measurements such as Fourier-transform infrared (FTIR) and Raman spectroscopy. The carbonate ions contained in ACC possess a different symmetry compared to those contained in crystals such that they have a different photon absorption behavior. For example, ACC has a ν_2 out-of-plane bending absorption peak around 860 cm^{-1} and no ν_4 in-plane bending absorption peak in its IR spectra while calcite has a ν_2 peak around 874 cm^{-1} and a ν_4 peak at 712 cm^{-1} , as shown in Figure 1.5a. In addition, ACC usually contains water in its structure that results in a broad absorption peak in the region of $2750\text{--}3600\text{ cm}^{-1}$ and a small absorption peak around 1640 cm^{-1} . [33, 90] These peaks are absent in anhydrous crystalline samples. Similarly, ACC displays Raman features that are distinctly different from its crystalline counterparts: ACC has an intense broad peak around 1085 cm^{-1} and a broad featureless hump around $140\text{--}300\text{ cm}^{-1}$, whereas crystalline CaCO_3 displays sharp peaks in these regions, as shown in Figure 1.5b.[97–99] In addition, crystalline CaCO_3 has a broad absorption peak in the range of $700\text{--}750\text{ cm}^{-1}$ that is absent in ACC.

A powerful tool to more closely probe the chemical environment of CO_3^{2-} contained in CaCO_3 is ^{13}C solid-state nuclear magnetic resonance (NMR) spectroscopy. Information on the structure of CaCO_3 can be extracted from the width of the ^{13}C peak measured with magic angle spinning (MAS) ^{13}C NMR spectroscopy. The ^{13}C peak measured for ACC is much broader than that of crystalline CaCO_3 : The line width of the ^{13}C peak measured for ACC is around 3.6 ppm and only around 0.3 ppm for calcite, as shown in Figure 1.5c.[76, 100] Additional information on the structure of CaCO_3 , including its hydration,[93, 100] might be extracted from the ^{13}C chemical

shift measured with MAS ^{13}C NMR spectroscopy.[90, 92, 93, 101] However, the chemical shifts measured for ACC relative to calcite vary: Some studies measure variations up to 1 ppm[92, 101, 102] whereas others do not observe any shifts.[76, 100, 103] A possible reason for these observed differences in ^{13}C chemical shifts might be varying hydrations of ACC particles that are produced under different processing conditions. Indeed, careful analysis of the ^{13}C chemical shift anisotropy (CSA) parameters performed using 2D $^{13}\text{C}\{^1\text{H}\}$ cross-polarization phase adjusted spinning sideband (CP PASS) NMR spectroscopy reveals that the C atoms contained in CO_3^{2-} ions of hydrated ACC form hydrogen bonds with water molecules.[103] These hydrogen bonds shift the C atoms away from the centroid of the O_3 triangular plane. This positional offset of the C atoms likely contributes to the observed ^{13}C chemical shift of ACC.

A commonly employed technique that offers more insights into the local structure of ACC particles is X-ray absorption spectroscopy (XAS). The coordination shells of the Ca atoms can be characterized with Ca K-edge XAS measurements.[104, 105] The region encompassing the main absorption peak, the X-ray absorption near-edge structure (XANES), provides qualitative information on the symmetry of the nearest neighbors of Ca atoms.[16, 105, 106] The different symmetries present in the structure of amorphous and crystalline CaCO_3 phases result in distinctly different absorption patterns. For example, Ca K-edge XANES spectra of ACC consist of a single main absorption peak around 4049 eV that does not contain any shoulder around 4045 eV. This main peak is partially convoluted with a small pre-edge peak around 4040 eV. By contrast, calcite results in two absorption peaks located around 4050 eV and 4060 eV, as shown in Figure 1.5d.[76] Its first main absorption peak encompasses a shoulder around 4045 eV and does not contain any pre-edge peak. More quantitative information on the ACC short-range order can be extracted from the Ca K-edge extended X-ray absorption fine structure (EXAFS) by fitting the undulations measured in these regions, as shown in Figure 1.5e.[16, 76, 105, 106] This analysis reveals information on the average coordination number (CN) of O atoms around Ca atoms as well as the average distance (R) between O and Ca atoms. CN of ACC varies from 2 to 7 but is most frequently around 6.[76, 92, 93, 107, 108] R of ACC is typically around 2.4 Å,[76, 92, 93, 107, 108] well in agreement with values obtained from ^{43}Ca NMR[109] and MD simulations.[80, 109, 110] These results suggest that ACC has a characteristic short-range order. Whether the small differences in the short-range order are a result of the different hydrations of ACC particles produced under different processing conditions remains to be shown. However, it is clear that variations of

the values for CN and R introduced by using different fitting procedures of EXAFS data are significant.[76, 96] This uncertainty in the data analysis makes it difficult to unequivocally relate differences in the hydrations of ACC phases to their structural variations.

Information on the local structure of ACC can also be extracted from a pair distribution function (PDF) analysis that is performed on total scattering data.[76, 111] This analysis indicates that ACC possesses short- and medium- range order up to a length scale of 10 Å.[76, 108] In particular, PDF spectra of ACC particles reveal a prominent feature at 2.4 Å that corresponds to the first Ca-O coordination shell, in good agreement with EXAFS results,[76, 107] as shown in Figure 1.5f.[76] Fits of the PDF spectra of X-ray and neutron total scattering results indicate that CN of oxygen atoms contained in the first coordination shell averages at 7, well in agreement with EXAFS results.[112] The majority of the oxygen atoms located in the first coordination shell originate from carbonate ions and the rest from water.[112] In addition, PDF data reveal two characteristic features in the medium-range length scale: One around $R = 4$ Å that can mainly be attributed to the Ca...Ca correlations and the other around $R = 6$ Å that can primarily be attributed to the Ca...O correlations.[96]

Several in-depth experimental studies reveal that the local structure of ACC displays similarities to that of one of the crystalline polymorphs of CaCO_3 , which might be related to the transformation of ACC into a crystal.[92, 93, 95, 101, 107, 113] These similarities have also been observed in MD simulations.[83, 114] In addition, MD simulations reveal that other structural features of ACC, including the orientational order[79, 115] and the distribution of angles of the nearest-neighboring atoms,[116] are similar to those of its crystalline counterparts. However, all these similarities are subtle and in certain experimental studies they are even inexistent[76, 90, 94] such that they are debated. A possible reason for the variations in the reported results of the local structure of ACC particles might be related to differences in their processing conditions[90, 92–94] and therefore their hydrations.[93] For example, if ACC particles are synthesized at increasing pHs, the intensity of the PDF peak at 3.7 Å grows on the expense of the peak at 4.1 Å, as shown in Figure 1.5g.[94] However, it remains to be investigated how the processing conditions influence the hydration of ACC.

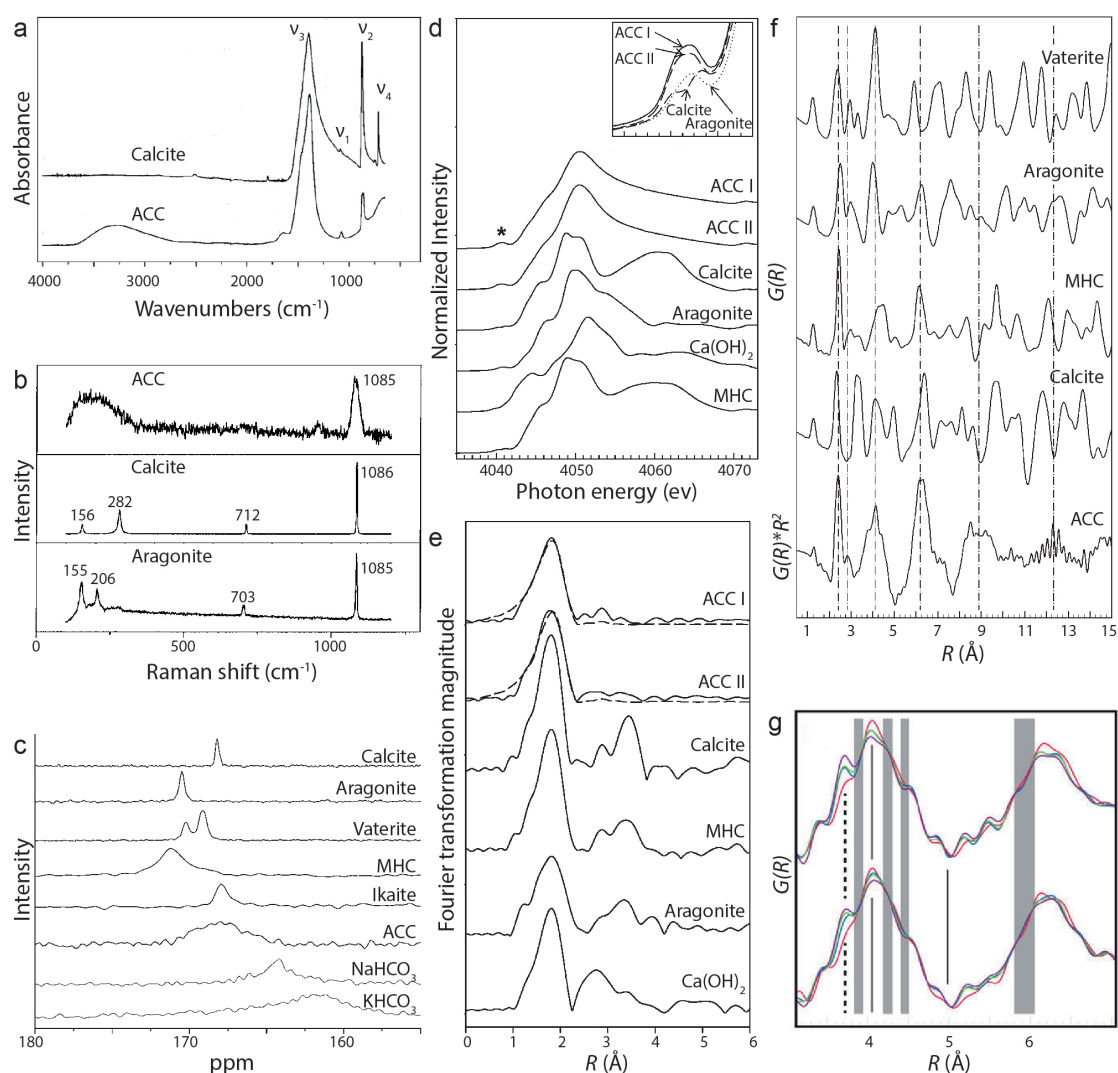


Figure 1.5 – Characterizations of the structure of ACC. (a) FTIR spectra of ACC particles and calcite.[54] The ν_1 peak corresponds to the symmetric stretching vibration, the ν_2 peak to the out-of-plane bending vibration, the ν_3 peak to the antisymmetric stretching vibration, and the ν_4 peak to the in-plane bending vibration of carbonate group. (b) Raman spectra of ACC, calcite, and aragonite.[98] (c) ^{13}C MAS solid-state NMR spectra of different CaCO_3 phases including ACC, vaterite, aragonite, calcite, monohydrocalcite (MHC), and ikaite, as well as two reference compounds, sodium hydrogencarbonate and potassium hydrogencarbonate.[100] (d) Ca K-edge XANES spectra of ACC particles that are synthesized through two different methods and four reference samples including calcite, aragonite, Ca(OH)_2 , and MHC with (e) the corresponding measured (solid line) and fitted (dashed line) Fourier Transforms of the EXAFS undulations in R -space. The peak at $\sim 1.8 \text{ \AA}$ measured for ACC samples after the correction for phase shift corresponds to a Ca-O distance of $\sim 2.4 \text{ \AA}$. [76] (f) PDF analysis of ACC and four different crystalline CaCO_3 phases. [76] (g) Zoom-ins of PDFs measured for ACC particles synthesized at pH=10.6 (red), pH=12.2 (blue), pH=12.5 (green), and pH=12.7 (violet). [94]

1.2.2 Influence of the hydration of ACC on its structure

Nature frequently produces anhydrous ACC.[16] By contrast, most synthetic ACC encompasses water; this water influences the stability of ACC against crystallization.[40, 86, 87] The amount of water contained in ACC depends on the processing conditions: The degree of hydration (n) of ACC, $\text{CaCO}_3 \cdot n\text{H}_2\text{O}$, has been reported to range from 0.4 to 1.6.[40, 76, 77, 81, 87, 92, 100, 108, 117] Molecular dynamics simulations and experiments reveal that the vast majority of water molecules is incorporated into the structure of ACC.[76, 112] Most of this water is directly bound to Ca atoms:[109, 112] 16-22% of the oxygen atoms contained in the first Ca coordination shell originate from water molecules.[110, 112] Similarly, water molecules form hydrogen bonds with the oxygen atoms contained in carbonate ions. Indeed, hydrogen bonds formed between water and carbonate ions are more favorable than those between two water molecules.[112, 118] These water-carbonate hydrogen bonds cause an in-plane displacement of carbon atoms contained in CO_3^{2-} away from the centroid of the O_3 triangle.[103] This distortion hampers the re-arrangement of ions, thereby stabilizing the ACC against crystallization.[103]

To obtain a better understanding of the distribution of water within ACC, a three dimensional (3D) atomic ACC model has been developed on the basis of the PDF analysis. This model indicates that ACC consists of a nano-porous Ca-rich matrix encompassing a percolating network of channels that are filled with CO_3^{2-} ions and water, as shown in Figure 1.6a.[96] The surrounding matrix encompasses H_2O molecules that strongly interact with Ca^{2+} ions such that these molecules have a low mobility.[96, 110, 119] By contrast, the nanochannels contain water molecules that form weaker hydrogen bonds with CO_3^{2-} such that their mobility is much higher.[96, 110, 119] This result is consistent with experimental ^1H solid-state NMR measurements that reveal two types of water molecules possessing a distinctly different mobility.[76] The two different types of water molecules can also be analyzed with thermogravimetric analysis (TGA) where weakly interacting, mobile water evaporates at much lower temperatures than the strongly interacting, rigid water.[108, 120, 121] Due to the different binding strengths, the mobile water can be removed from ACC particles through freeze drying, in stark contrast to the rigid water.[122, 123]

The existence of two types of water molecules possessing a distinctly different mobility within ACC is well accepted and has been confirmed with simulations and experiments.[76, 118, 120, 121] However, the dimensions of nano-channels that are

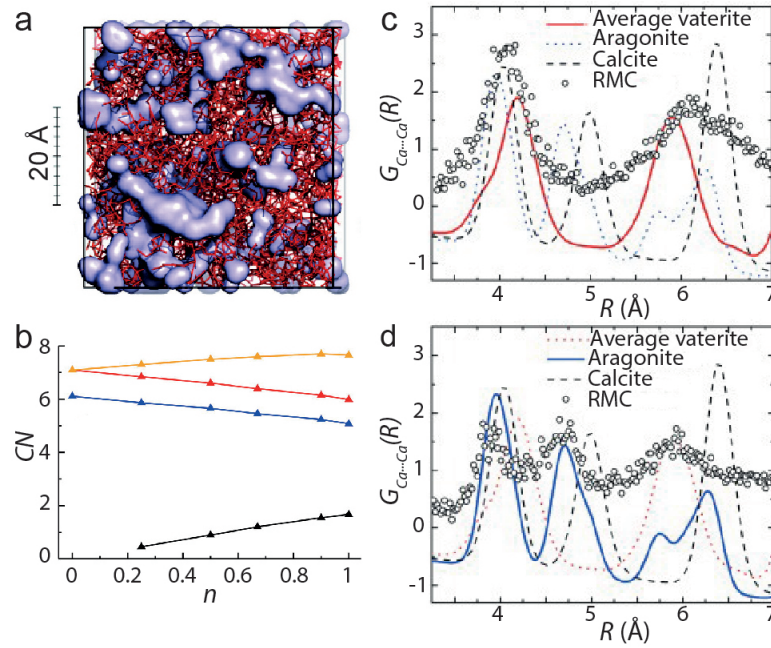


Figure 1.6 – Hydration of ACC and its influence on the short- and medium- range order of ACC. (a) Stereo representation of an atomic 3D model of the nanoporous structure of ACC. The Ca-rich frameworks are indicated by the red sticks, the water-rich nanochannels by the blue surfaces.[96] (b) CN of the O (orange) and C (blue) atoms within the first coordination shell of Ca as a function of n of ACC determined by MD simulations. The O atoms contributed by water molecules are indicated in black, those contributed by carbonate ions in red.[114] (c, d) Ca...Ca correlations in (c) as-synthesized ACC particles and (d) those exposed to a pressure of 11.9 GPa obtained from reverse Monte-Carlo (RMC) modelling of their PDFs. They are compared to that of calcite, aragonite, and vaterite at ambient pressure.[124]

filled with mobile water are debated.[96, 111, 112] This uncertainty might be related to the dynamic nature of these channels: MD simulations reveal that nano-channels shrink with time due to ion re-arrangements.[109, 114] These results imply that even if such channels exist during early stages of the ACC formation, they disappear on time scales that are difficult to access experimentally. Hence, experimental evidence of these nano-channels is missing.

The formation of mobile water-rich channels as big as a few nm is still debated. However, it is clear that mobile water molecules form a percolating network if n of ACC is sufficiently high.[112, 118] Simulations suggest that percolating water networks form if n of ACC exceeds 0.8.[118] If n falls below this threshold value, the mobility of water molecules and ions significantly decreases.[118] This observation suggests that

the majority of water contained in ACC with n below 0.8 is rigid. This suggestion is in line with TGA results where n measured for ACC samples that have been treated at temperatures around 100 °C to remove the mobile water is below 0.8.[76, 121]

Water contained in ACC particles can influence their short- and medium- range order. A dehydration of ACC is thus accompanied by a re-arrangement of ions, as indicated by MD simulations.[110, 114, 118, 119] During dehydration, H₂O molecules present in the first Ca-O coordination shell are replaced by CO₃²⁻ groups. As a result of this exchange, the values of CN and R for the first Ca-O coordination shell remain nearly constant, as shown in Figure 1.6b.[112, 114] Hence, it is difficult to experimentally quantify structural differences for ACC particles possessing different n with commonly used methods such as Ca K-edge EXAFS. Yet, these differences can be qualitatively assessed by comparing PDF spectra of ACC particles subjected to elevated temperatures or pressures, where their n changes *in situ*. [86, 124] For example, structural changes in ACC could be observed with PDF if the dehydration is induced with uniaxial pressures as high as 12 GPa. This dehydration is accompanied by a re-arrangement of ions into a structure that displays some resemblance with aragonite, as demonstrated with PDF in Figures 1.6c-d.[124] These results are consistent with those obtained from MD simulations where the denser structure of partially or fully dehydrated ACC is observed to display some resemblance with one of the anhydrous crystalline CaCO₃ polymorphs.[114–116, 119]

Some processing conditions, including the pH,[92–94] solvent,[90] and temperature[93] of the solution from which ACC is produced influence the water-ion interactions within ACC.[81, 93] Hence, these parameters are expected to influence the ratio of mobile to rigid water present in ACC and therefore its local structure. Interestingly, many ACC particles produced under varying processing conditions possess a similar degree of hydration. This observation suggests that the degree of hydration is insufficient to characterize ACC. Instead, the ratio of mobile to rigid water that is an often overlooked but high relevant must also be considered.

1.3 Crystallization of ACC

Amorphous CaCO₃ particles with diameters exceeding a few nanometers are metastable[28, 86–88] and therefore tend to transform into crystals with time.[31, 125, 126] This crystallization can be accelerated if particles are immersed in bulk

solutions[29, 30, 40, 53, 54, 81, 122] or exposed to elevated temperatures [28, 81, 86, 87, 121, 122, 127, 128], pressures[129, 130] and humidity.[40, 86, 121, 123, 131, 132] The kinetics of this crystallization and the structure and morphology of the resulting crystals can be significantly influenced by the crystallization pathway.[77, 81, 86, 121] Different ACC crystallization pathways have been proposed in the last decade, as schematically summarized in Figure 1.2. A particularly important parameter that determines the crystallization pathway is the presence of free water in the crystallization environment: In the presence of free water, crystallization often occurs through a dissolution-precipitation pathway. By contrast, in the absence of free water in the crystallization environment, ACC particles typically crystallize through a solid-state transformation. In these two crystallization pathways, the propensity of ACC particles to crystallize primarily depends on their kinetic stability that is, at least in parts, influenced by the hydration of ACC, as summarized below.

1.3.1 Solid-state transformation

To convert ACC particles into crystals via a solid-state transformation, they must be dehydrated before anhydrous crystalline nuclei form.[77, 114] The dehydration process of ACC was initially proposed to be thermodynamically favored because the enthalpy of hydrated ACC particles measured with isothermal acid solution calorimetry was higher than that of anhydrous ones measured with differential scanning calorimetry (DSC).[87] This thermodynamic argument has often been used to describe the solid-state transformation of biogenic ACC under ambient conditions.[17, 23, 87, 133, 134] However, more recent experiments that assessed the enthalpy of ACC before and after its dehydration using the same technique reveal that dehydrated ACC particles possess a higher enthalpy.[86, 108] These more recent experimental results are supported by MD simulations that suggest the dehydration to be thermodynamically unfavorable, as shown in Figure 1.7a.[80, 114, 118] To overcome the energy penalty associated with the dehydration, ACC must be exposed to an external energy source, for example, elevated temperatures.[81, 86, 94, 121]

Dehydration of ACC is associated with a re-arrangement of ions contained in ACC.[86, 108, 112, 114, 118] This re-arrangement is kinetically hindered by the interactions between water and ions contained in ACC, which decrease the mobility of water and ions.[96, 103, 114] In the early stage of dehydration where n of ACC is high and a significant amount of water is mobile, water can be removed relatively

easily.[76, 110, 114, 119] With progressing dehydration, the interactions between water and ions contained in ACC become stronger such that the energy barrier for further water removal increases.[114] For example, when n of ACC decreases from 1.4 to 1, the activation energy barrier (E_A) for dehydration increases from $50 \text{ kJ}\cdot\text{mol}^{-1}$ to $120 \text{ kJ}\cdot\text{mol}^{-1}$, as shown in Figure 1.7b.[77] When n reaches values below the percolation threshold, for example 0.8, E_A for further water removal increases even more rapidly.[118] This strong increase in E_A might be related to the need for substantial ion re-arrangements required to remove additional water.[108, 118] For example, when n is around 0.2, where the majority of water is rigid[76, 121] and hence strongly bound,[96, 114, 118] E_A for water removal is as high as $250 \text{ kJ}\cdot\text{mol}^{-1}$. [77] Once E_A for the removal of the remaining water is overcome such that ACC is fully dehydrated, crystalline CaCO_3 nuclei form and grow by consuming the amorphous matrix.[77] Indeed, E_A to dehydrate ACC with $n = 0.2$ is significantly higher than of the crystallization of anhydrous ACC[77] such that the dehydration is the rate-limiting step of the solid-state transformation of ACC. E_A to dehydrate ACC depends on the ion-water interactions within ACC and hence, on the ratio of mobile to rigid water contained in it. These results suggest that the kinetic stability of ACC against solid-state transformation depends on the ratio of mobile to rigid water.

The free energy of ACC particles decreases with increasing degrees of hydration such that their thermodynamic stability increases.[118] However, the stability of ACC particles against crystallization, typically expressed as their lifetime or the critical crystallization temperature, refers to their kinetic rather than their thermodynamic stability. These two stabilities are not directly related to each other: For example, the enthalpy of ACC particles increases with an increasing pH of the solution from which they are synthesized, such that their thermodynamic stability decreases.[28] Nevertheless, their kinetic stability, measured as the critical crystallization temperature, increases.[28]

The kinetic stability of ACC against solid-state transformation is mainly determined by E_A of its dehydration. With an increasing n , the mobility of ions increases, thereby facilitating their re-arrangement and reducing this E_A . [118] Hence, the kinetic stability of ACC particles against solid-state transformation decreases with an increasing n . [40, 121] This is exemplified by the lower temperature required to induce the solid-state crystallization: As-synthesized hydrated ACC particles crystallize at 277°C , whereas those that have been partially dehydrated through annealing crystallize at 321°C . [121] In addition, the kinetic stability of ACC particles against solid-state transformation depends on their processing conditions such as the pH and solute

1.3. Crystallization of ACC

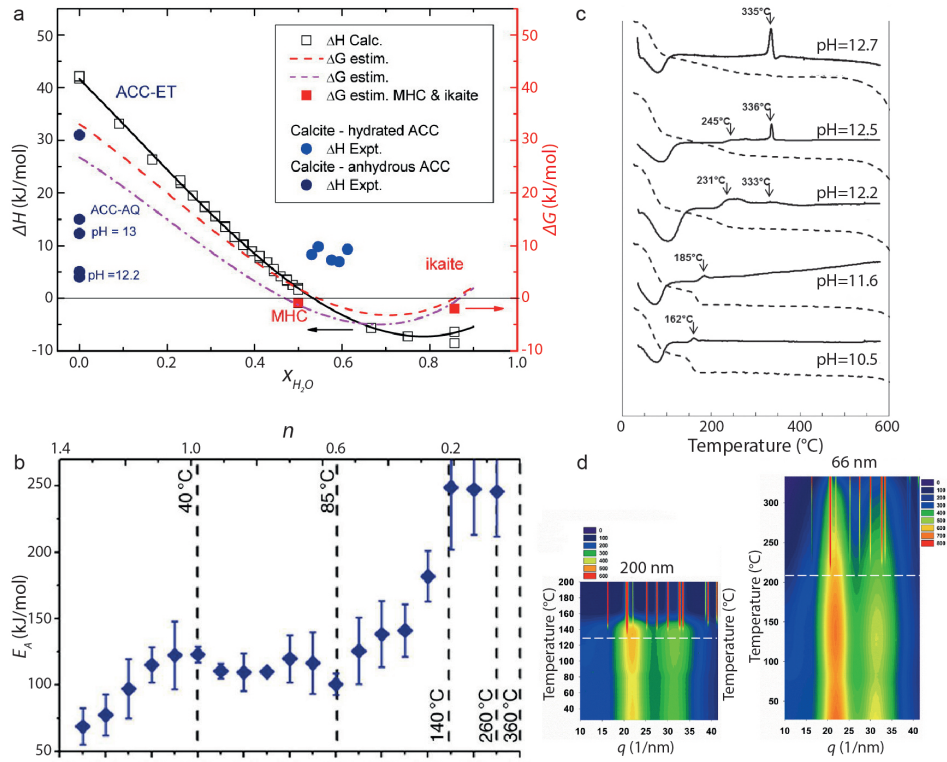


Figure 1.7 – Solid-state transformation of ACC. (a) Enthalpy (ΔH) and free energy (ΔG) of ACC particles relative to calcite as a function of the molar fraction of water (χ_{H_2O}) contained in ACC obtained by MD simulations.[118] (b) E_A of the dehydration process of ACC as a function of its n . [77] (c) DSC (solid line) and TGA (dashed line) analysis of ACC particles synthesized at different pHs.[94] (d) Contour plots of the wide-angle X-ray scattering (WAXS) intensity of ACC particles with different sizes while being heated as a function of the scattering vector (q) and temperatures. When the solute concentration increases from 5 mM to 100 mM, the average diameter of the resulting ACC particles decreases from 200 nm to 66 nm. The critical crystallization temperatures are indicated by the white dashed lines.[81]

concentration.[28, 94, 108] For example, if the pH of the synthesis solution increases from 10.6 to 12.7, the kinetic stability of the resulting ACC particles, measured as their critical crystallization temperature, increases from 162 °C to 335 °C, as shown in Figure 1.7c.[94] Similarly, if the concentration of solutes present during the ACC synthesis increases from 5 mM to 100 mM, the critical crystallization temperature of the resulting ACC particles increases from 130 °C to 220 °C, as shown in Figure 1.7d.[81] This increase in kinetic stability was assigned to a decrease in the particle size: As the pH or solute concentration increase, the degree of supersaturation of the solution increases such that ACC particles with smaller sizes are produced.[81] The surface energy of ACC is below that of any of the crystalline counterparts, such that smaller

ACC particles, which have a higher surface-to-volume ratio, are thermodynamically more stable than larger ones.[81] However, it is unlikely that the higher kinetic stability of smaller ACC particles is related to their higher thermodynamic stability. Instead, these small ACC particles display a different dehydration behavior than larger particles that have a similar degree of hydration.[81] This observation implies that the particle size might influence the ratio of rigid to mobile water contained in ACC and thereby the kinetic stability of ACC against solid-state transformation. However, experimental evidence to support this implication is still lacking.

Similarly, if ACC particles crystallize at elevated pressures, their kinetic stability against crystallization can be influenced by their degree of hydration. For example, ACC particles containing 10 wt% H₂O crystallize if loaded with 800 MPa, whereas those containing 21 wt% H₂O already crystallize if subjected to 240 MPa.[129] However, it remains unclear whether the pressure-induced crystallization occurs through a solid-state transformation. The structure of CaCO₃ crystals obtained from the pressure-induced crystallization is distinctly different from that obtained from the temperature-induced one: The crystallization of ACC at elevated pressures results in a mixture of metastable vaterite and stable calcite,[129, 130] whereas that at elevated temperatures only produces calcite.[81, 92, 121] This difference in the structure of the resulting CaCO₃ crystals might be related to the different crystallization kinetics in these two crystallization processes. Indeed, if the applied pressures decrease[129] such that the crystallization kinetics is reduced, the fraction of vaterite present in the mixture formed after the pressure-induced crystallization increases.

1.3.2 Dissolution-reprecipitation

If ACC particles are exposed to bulk aqueous solutions, they tend to dissolve. The resulting solutions become supersaturated with respect to the crystalline phases and CaCO₃ crystals start to precipitate.[81, 121] This dissolution-reprecipitation pathway has been extensively demonstrated using different techniques such as X-ray microscopy,[53] titration,[81] electron microscopy,[40] isotope tracing,[135] and time-resolved SAXS and WAXS,[30] as exemplified in Figure 1.8a. It has also been suggested that the dissolution of ACC particles at room temperature is preceded by their dehydration.[29, 40, 54, 77, 133, 134] However, the very high activation energies of the ACC dehydration, which range from 50 to 250 kJ·mol⁻¹, [77] kinetically hinder this process such that it is questionable if ACC particles dehydrate before they dissolve in

bulk solutions.

If ACC particles crystallize through a dissolution-reprecipitation pathway, their kinetic against crystallization is primarily determined by their dissolution rate as well as the nucleation and growth rate of new crystals. According to the Noyes-Whitney equation,[136] the dissolution rate can be expressed as,

$$r_{dis} = A \frac{D_{ion}}{l(C_s - C_b)} \quad (1.1)$$

where r_{dis} is the dissolution rate, A the surface area of ACC particles, l the distance over which Ca^{2+} and CO_3^{2-} ion concentration gradients exists, D_{ion} the diffusion coefficient of ions, C_s the saturation concentration of ions with respect to the solubility of ACC, and C_b the concentration of ions in bulk solutions. These parameters and hence the dissolution kinetics can be influenced by the size[81] and n [40] of ACC particles as well as the crystallization conditions such as the pH,[60, 137] temperature,[33, 68] and solvent[90, 138, 139] of bulk solutions. For example, if the ethanol volume fraction in the solution increases from 76 vol% to 98 vol%, the time required to dissolve ACC particles and form crystals increases from 1.5 h to 4 days.[138] If all the water is replaced by ethanol, the crystallization time even increases to 7 days.[139] Similarly, ACC particles with smaller sizes, which are produced from solutions possessing a higher degree of supersaturation, display an increased ACC dissolution rate compared to larger counterparts.[81, 140] As a result, the kinetic stability of small particles in bulk solutions is lower than that of bigger ones.[81] Interestingly, the kinetic stability of ACC particles increases with increasing pHs of the synthesis solution[94, 139] although their solubility increases[60, 137, 141] and their size decreases,[81] as shown in Figure 1.8b. This increase in the kinetic stability likely is related to the high concentration of hydroxide ions, present at high pHs that slows down the formation of new crystals.[94] These examples illustrate that the kinetic stability of ACC against dissolution and the formation of new CaCO_3 crystals in bulk solutions is a complex interplay between multiple factors. Further studies are warranted to relate the influence of the different processing conditions to the dissolution of ACC particles as well as the nucleation and growth of new crystals.

The structure of CaCO_3 crystals that form from bulk solutions containing ACC particles is primarily governed by the kinetics of their dissolution and that of the new crystal formation.[40, 81, 135] The dissolution kinetics influences the local degree of

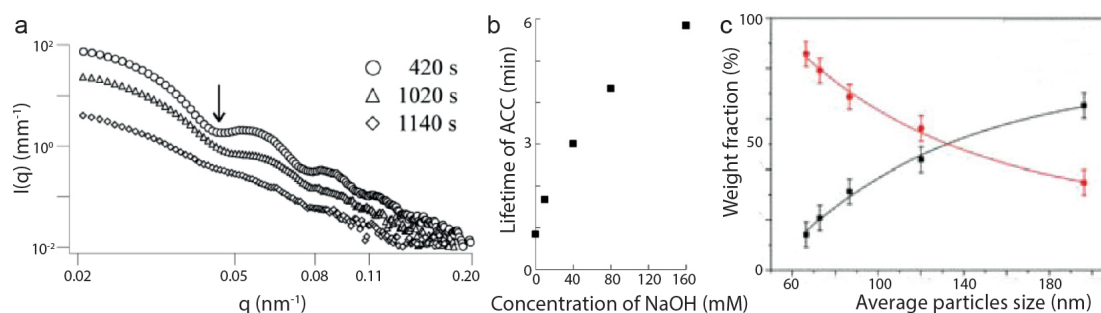


Figure 1.8 – Crystallization of ACC through a dissolution-reprecipitation pathway. (a) Radially averaged SAXS scattering profiles at different times after mixing a solution containing 9 mM CaCl_2 and one containing 9 mM Na_2CO_3 . The spherical form factor indicated with an arrow shifts toward larger scattering angles, indicating the dissolution of ACC particles.[30] (b) Influence of the NaOH concentration on the lifetime of ACC dispersed in aqueous solutions.[94] (c) Weight fraction of calcite (black) and vaterite (red) formed from ACC particles dispersed in aqueous solutions as a function of the size of particles.[81]

supersaturation with respect to one of the crystalline CaCO_3 polymorphs. Hence, it also influences the kinetics of nucleation and growth of new crystals.[81, 137, 139] For example, within the same observation time, small ACC particles that quickly dissolve preferentially transform into vaterite, whereas larger ACC particles that dissolve more slowly tend to transform into calcite, as shown in Figure 1.8c.[81] However, if ACC particles are left in solution for an extended amount of time, the final crystals always attain the thermodynamically most favorable structure, calcite.[29, 54, 94]

If ACC particles are exposed to humid air where the amount of free water is significantly smaller compared to bulk solutions, they have been suggested to crystallize through a local dissolution-reprecipitation pathway. In this case, water contained in the humid air is absorbed by the surfaces of ACC particles and partially dissolve them. This is in stark contrast with the complete dissolution in the case of crystallization in bulk solutions. The partial dissolution process locally results in a supersaturated solution from which new CaCO_3 crystals start to form.[40, 121, 123] Because the dissolution kinetics of ACC particles scales with the rate of water absorbed by their surface, their kinetic stability decreases with an increasing humidity.[121, 123] For example, if ACC particles are stored at a relative humidity (RH) of 35%, they are stable against crystallization for more than 4 hours, whereas they crystallize within 1 hour if the relative humidity is increased to 90%.[121] Similarly, the crystallization kinetics increases with an increasing degree of hydration of ACC.[86, 117] For example, if ACC particles

are freeze dried to remove the mobile water contained in them and subsequently stored under reduced pressures or in gas-tight vials, they remain amorphous for more than 150 days.[123] The much lower amount of water available to dissolve ACC also delays the crystallization kinetics of CaCO_3 : If transformed under these conditions, metastable crystalline phases, such as aragonite can form; these metastable polymorphs do not form in bulk solutions at room temperature in the absence of any additive.[123]

1.4 Influence of soluble additives

Most ACC found in nature contains various soluble additives, such as Mg^{2+} and acidic proteins containing carboxyl or phosphate groups.[16] The roles of these additives in the formation of CaCO_3 have been extensively investigated in last decades, as has been summarized in excellent reviews.[6, 142] These additives can influence the formation[143–145] of ACC, its structure,[16, 104, 105] and stability,[86, 122, 138, 146] as well as the composition, morphology, structure, and mechanical properties of the resulting crystals.[8, 10, 147, 148] This improved understanding leads to a rapidly increasing use of additives to tune the formation as well as crystallization of ACC formation and thereby the properties of synthetic CaCO_3 -based materials.[34, 44, 149–156] Some recent progress in studying the influence of the most commonly employed additives is summarized below.

1.4.1 Magnesium ions

If ACC is formed from a highly supersaturated solution containing Ca^{2+} , CO_3^{2-} , and Mg^{2+} ions, an ACC phase encompassing Mg^{2+} (Mg-ACC) phase usually precipitates first.[11, 131, 157–160] The formation of Mg-ACC is thermodynamically favored over that of pure ACC[161] because the charge density of Mg^{2+} is higher than that of Ca^{2+} , [162, 163] enabling a stronger interaction of the Mg-ACC phase with water.[164] This strong interaction increases the amount of water contained in the amorphous phase[165] such that the free energy of Mg-ACC is lower compared to pure ACC. However, the kinetics of the nucleation and growth of Mg-ACC is not significantly affected by the incorporation of Mg^{2+} [166]

The composition of the Mg-ACC phase, namely the amount of Mg^{2+} that is incorporated into it, depends on the solute concentration[167] and the solution pH.[168] In

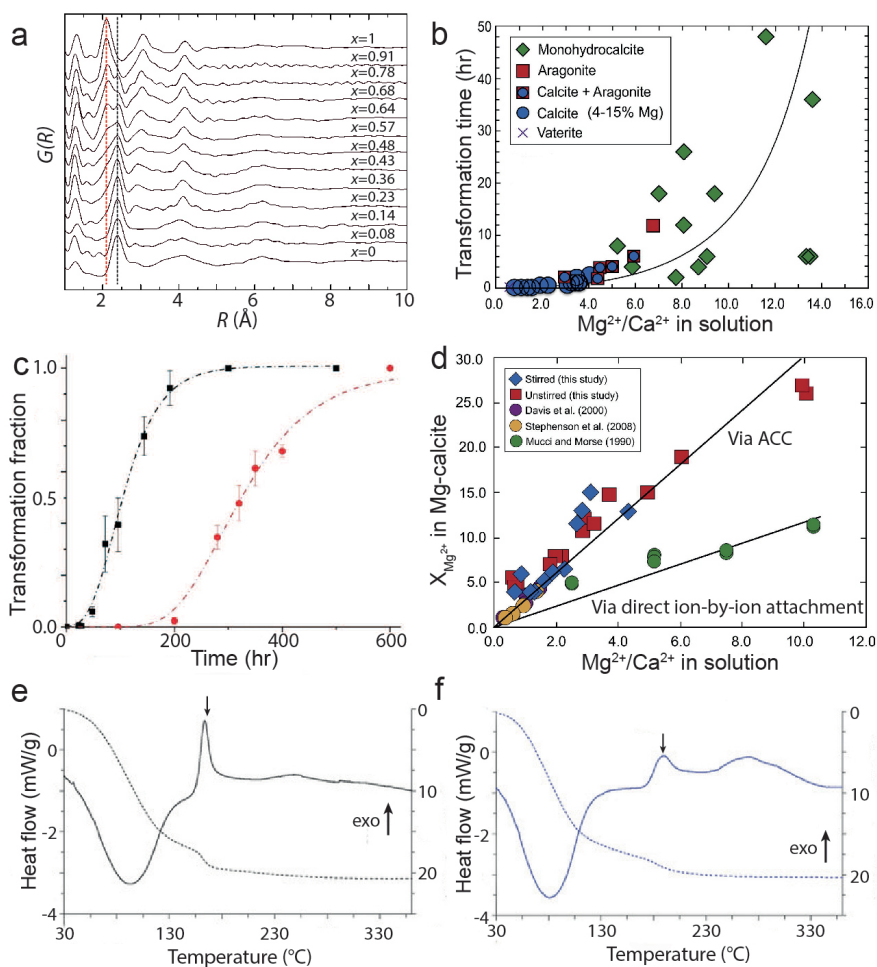


Figure 1.9 – Influence of Mg^{2+} on the formation of $CaCO_3$. (a) PDFs of the Mg-ACC ($Ca_{1-\chi}Mg_{\chi}CO_3 \cdot nH_2O$) with different molar fractions of incorporated Mg^{2+} ions (χ). The first Mg-O coordination shell is indicated with a red line and the first Ca-O coordination shell with a black line. Their peak positions are independent of χ , indicating that there is no change of the short-range order around Ca or Mg atoms upon incorporation of Mg^{2+} ions into ACC.[161] (b) Influence of the molar ratio of $Mg^{2+}:Ca^{2+}$ in the aqueous solutions on the kinetic stability of Mg-ACC particles against the transformation into different crystalline $CaCO_3$ polymorphs.[159] (c) Evolution of the crystallization of pure ACC (black) and Mg-ACC (red), synthesized from a solution containing a molar ratio of $Mg^{2+}:Ca^{2+}$ of 1:10, as a function of the time stored in a $RH \sim 50\%$. [131] (d) Influence of the molar ratio of $Mg^{2+}:Ca^{2+}$ contained in solution on χ of the resulting Mg-calcite ($Ca_{1-\chi}Mg_{\chi}CO_3$) crystals formed through ion-by-ion attachment and from Mg-ACC precursors. χ present in the resulting Mg-calcite are approximately three-fold lower if produced through ion-by-ion attachment in the absence of Mg-ACC precursors.[159] (e, f) DSC (solid line) and TGA (dashed line) analysis of (e) pure ACC and (f) Mg-ACC containing 2.4 mol% Mg^{2+} . The critical crystallization temperatures are marked with arrows.[86]

addition, the amount of incorporated Mg^{2+} depends on the molar ratio of $\text{Mg}^{2+}:\text{Ca}^{2+}$ contained in the solution.[157, 159, 167, 168] Nevertheless, the Mg addition is not stoichiometric but the ratio of $\text{Mg}^{2+}:\text{Ca}^{2+}$ in Mg-ACC particles is always below that of the solution from which they are produced. The preferential incorporation of Ca^{2+} over Mg^{2+} into Mg-ACC might be caused by the slow dehydration kinetics of Mg^{2+} ions that delays their inclusion.[161, 169] In line with this hypothesis, the incorporation kinetics and hence, the fraction of incorporated ions increases with increasing radii of divalent cations such that the incorporation efficiency into ACC increases from Mg^{2+} to Sr^{2+} to Ba^{2+} . [170]

Due to the difference in the ionic radii of Ca^{2+} and Mg^{2+} , the structure of ACC is expected to change upon incorporation of Mg^{2+} . The *CN* and *R* of the first Ca-O coordination shell of Mg-ACC has been reported to be distinctly different from that of pure ACC, as determined with Ca K-edge EXAFS.[106] This is in contrast with more recent ^{43}Ca NMR[109] and ^{13}C NMR[168] studies that provide no evidence for any change in the short-range order of ACC around Ca atoms upon incorporation of Mg^{2+} . Indeed, PDF analysis suggests that the structure of Mg-ACC is a mixture of pure ACC and pure amorphous magnesium carbonate (AMC) nanoclusters, as shown in Figure 1.9a.[161] If the χ of Mg-ACC is below 0.48, ACC and AMC nanoclusters are homogeneously distributed within the amorphous particles.[161, 168] By contrast, their distribution must be further assessed if χ is higher.[161, 168]

Magnesium ions are often employed to increase the stability of ACC against crystallization in bulk solutions. Indeed, the lifetime of Mg-ACC particles increases with an increasing molar fraction of Mg^{2+} in solution that also leads to an increased concentration of Mg^{2+} in Mg-ACC, as shown in Figure 1.9b.[157, 159] The increased lifetime of Mg-ACC has been related to its reduced free energy compared to pure ACC.[161] However, the lifetime of ACC is solely related to the dissolution and crystallization kinetics and hence, it is in a first approximation independent of the thermodynamic stability of these particles. Indeed, the lifetime of AMC is longer than that of ACC, despite its lower thermodynamic stability.[161] The observed increased lifetime of Mg-ACC has been related to the higher dehydration energy of Mg^{2+} compared to that of Ca^{2+} that slows down the dehydration of the amorphous phase prior to its crystallization.[111, 161, 171, 172] However, the high activation energy associated with the dehydration kinetically hinders this process such that it is unlikely to occur in the presence of bulk solutions at room temperature. Instead, Mg-ACC particles that are in contact with bulk solutions dissolve and new crystals forms from the supersaturated

solution.[135] In this case, the observed delay in the crystallization of Mg-ACC must be related to its retarded kinetics of dissolution and the delayed nucleation and growth of new crystals. This delay can be caused by Mg^{2+} ions present in Mg-ACC as well as in the bulk solution. The lower free energy of Mg-ACC is expected to reduce its solubility in aqueous solutions,[40, 161] thereby slowing down its dissolution. However, this expectation could not have been confirmed: The dissolution profiles of pure ACC and Mg-ACC are very similar if particles are dispersed in pure water.[122] Remarkably, the addition of a small amount of free Mg^{2+} ions into water significantly delays the dissolution of pure ACC particles.[164] These results indicate that the dissolution kinetics is mainly influenced by free Mg^{2+} ions present in bulk solutions rather than those contained in Mg-ACC. Free Mg^{2+} ions can also influence the growth kinetics of new crystals: These ions can adsorb onto the surfaces of newly formed crystals, thereby delaying or even inhibiting their growth.[49] Hence, the crystallization kinetics of the amorphous phase can be slowed down by free Mg^{2+} ions.[122, 157] As a result of the delayed crystallization kinetics of Mg-ACC particles observed in the presence of free Mg^{2+} ions, these particles are more stable against crystallization than pure ACC ones not only in bulk solutions but also if stored in a humid environment, as shown in Figure 1.9c.[86, 131, 161, 167]

Additives such as Mg^{2+} influence the crystallization kinetics of ACC in the presence of free water. In addition, they affect the structure of the resulting crystals. If the ratio of $\text{Mg}^{2+}:\text{Ca}^{2+}$ in the aqueous solution is high, Mg-ACC preferentially transforms into aragonite or MHC, as shown in Figure 1.9b.[157, 159] By contrast, if the ratio of $\text{Mg}^{2+}:\text{Ca}^{2+}$ is low, Mg-ACC preferentially transforms into Mg-calcite.[157, 159] Remarkably, χ of Mg-calcite crystals is always identical to that of Mg-ACC precursors.[159] This good correlation suggests that Mg-ACC strongly influences the formation of Mg-calcite. Its influence most likely is related to the ratio of $\text{Mg}^{2+}:\text{Ca}^{2+}$ ions present in the locally supersaturated solution that scales with that of dissolved Mg-ACC particles.[159] By contrast, if Mg-calcite is produced from solutions that are undersaturated relative to Mg-ACC but supersaturated relative to calcite, Mg-calcite directly forms through ion-by-ion attachment without the formation of any Mg-ACC intermediates. In this case, χ of Mg-calcite is approximately three-fold reduced compared to that in particles produced via Mg-ACC precursors, as shown in Figure 1.9d.[159] This comparison demonstrates that higher amounts of Mg^{2+} can be incorporated into Mg-calcite particles if they form through the dissolution-reprecipitation of Mg-ACC. The amount of incorporated Mg^{2+} influences the properties of Mg-calcite crystals and hence, is an

important parameter that needs to be closely controlled if materials with well-defined properties want to be synthesized.[131, 157, 160, 173, 174]

The incorporation of Mg^{2+} into ACC also delays its solid-state transformation: The strong interactions between Mg^{2+} and water molecules reduce the mobility of water,[165, 169, 175] thereby increasing the fraction of rigid water contained in Mg-ACC compared to that contained in ACC.[165] As a result of this stronger interactions, E_A for the dehydration of Mg-ACC is higher than that of pure ACC such that the temperature where Mg-ACC starts to crystallize is higher.[86, 122] For example, ACC containing 2.4 mol% Mg^{2+} starts to crystallize around 190 °C, while pure ACC crystallizes around 160 °C, as shown in Figures 1.9e-f.[86] Despite the different crystallization temperatures, the structure of the resulting crystals is usually the same: calcite.[86, 122]

1.4.2 Other low molecular weight additives

Apart from Mg^{2+} , many other low molecular weight additives are well known to influence the ACC formation. These additives typically contain functional groups that display a high affinity to Ca^{2+} . [143, 145] For example, citrate (CIT), which contains carboxylic groups, has been reported to favor the formation and stabilization of CaCO_3 PNCs, thereby delaying the nucleation of ACC particles.[143, 145] Yet, this additive does not change the critical degree of supersaturation for the nucleation of ACC particles such that it does not noticeably influence the size of the resulting ACC particles.[176] A similar behavior has been observed for other carboxyl-containing molecules such as aspartic acid (Asp) and glycine (Gly).[170, 177]

Atomic absorption spectroscopy (AAS), TGA, and X-ray photoelectron spectroscopy (XPS) suggest that carboxyl-containing low molecular weight additives are contained within the ACC particles or associated with their surfaces.[122, 176, 177] By contrast, amino acid analysis did not reveal any traces of Asp within ACC particles.[170] These results imply that Asp is preferentially adsorbed at the surface of particles from which it can be removed by a thorough wash. This implication is supported by PDF analysis that does not reveal any significant structural difference of ACC particles upon their functionalization with Asp, Gly, or CIT.[176, 177] However, to conclusively determine the location of low molecular weight additives that are associated with ACC particles, further studies are warranted.

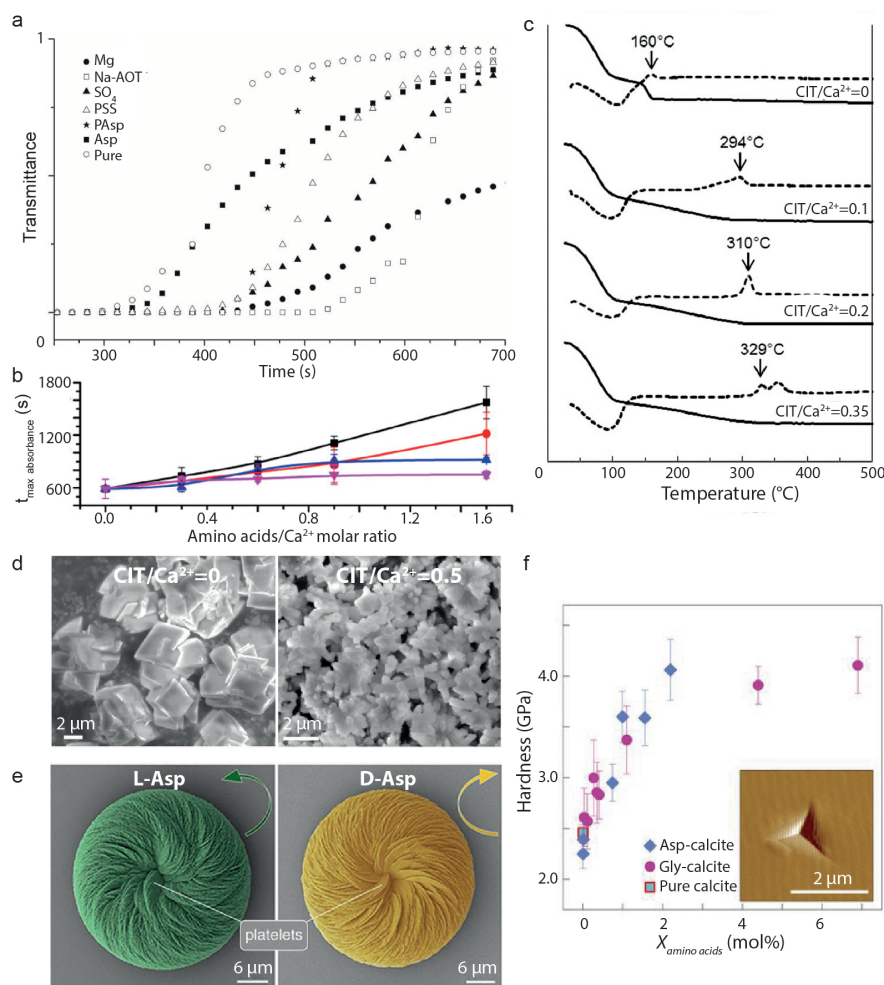


Figure 1.10 – Influence of other low molecular weight additives on the formation of CaCO₃. (a) Evolution of the UV-vis transmittance recovery as a function of time after an aqueous solution containing 1 M CaCl₂ is mixed with one containing 1 M Na₂CO₃ in the presence of 200 ppm poly(styrene sulfonate) (PSS), Asp, PAsp, bis(2-ethylhexyl)sulfosuccinate (AOT), 10 mM Mg²⁺, or 2 mM SO₄²⁻. The longer the recovery time of the transmittance is, the higher is the kinetic stability of ACC particles against crystallization in bulk solutions.[122] (b) Influence of the molar ratio of amino acids and Ca²⁺ ions on the lifetime of ACC particles dispersed in aqueous solutions measured for Asp (black), glutamic acid (red), asparagine (blue), and valine (purple).[178] (c) TGA (solid line) and DSC (dashed line) analysis of ACC particles synthesized in the presence of different amounts of CIT. The critical crystallization temperatures are marked with arrows.[176] (d) SEM images of calcite crystals formed from ACC particles in the presence of different amounts of CIT.[176] (e) SEM images of toroid vaterite crystals formed in the presence of L-Asp that spiral counterclockwise (green) and D-Asp that spiral clockwise (brown).[179] (f) Influence of the molar fraction of Asp (blue) and Gly (purple) that is incorporated into calcite single crystals on their hardness. A scanning force microscopy image showing the plastic deformation of additive-functionalized calcite is shown in the inset.[150]

Phosphates display a distinctly different behavior: They favor the formation of CaCO_3 -rich liquid phases during the liquid-liquid phase separation or stabilize these phases once they formed.[145, 170] Thereby, these additives increase the critical supersaturation concentration where nucleation of ACC occurs.[143, 145] Based on FTIR and ^{31}P solid-state NMR analysis, it has been suggested that PO_4^{3-} ions are molecularly dispersed in the resulting ACC particles.[128, 170] However, these additives do not significantly influence the short- and medium-range order of ACC. The only slight structural difference that could be observed with PDF was a broadening of the peak around 4.1 Å.[86]

Many low molecular weight additives that possess a high affinity to Ca^{2+} increase the kinetic stability of ACC particles if dispersed in bulk solutions, as shown in Figure 1.10a.[122] In particular, PO_4^{3-} , [86] SO_4^{2-} , [122] and carboxyl-containing molecules including CIT,[176] phytic acid,[180] and amino acids such as Gly,[177] Asp,[122, 177] phosphoserine,[181] and phosphothreonine[181] have been reported to strongly increase the lifetime of ACC particles. The increased kinetic stability of these particles must be related to a delayed dissolution of ACC or a retarded formation of CaCO_3 crystals. The influence of low molecular additives on the dissolution rate of ACC particles remains unclear. By contrast, many of these additives, including PO_4^{3-} , [182, 183] SO_4^{2-} , [29, 183] CIT,[183] and Asp[184, 185] are known to slow down or even inhibit the growth of crystals by adsorbing on their surfaces. Indeed, the kinetic stability of ACC against crystallization in the presence of free water increases with increasing ability of these additives to inhibit crystal growth. As a result of this correlation, the stability of ACC particles sequentially increases if functionalized with valine, asparagine, glutamic acid, and Asp due to their increasing affinity towards the CaCO_3 crystal surface, as shown in Figure 1.10b.[178]

Certain low molecular weight additives also delay the crystallization of ACC particles that are not in contact with free water and hence undergo a solid-state transformation. These additives do not significantly change the structure or overall degree of hydration of ACC.[86, 122, 170, 176, 177] Instead, they strongly interact with water contained in ACC, thereby reducing its mobility and hence increasing the energy barrier for dehydration.[86, 128, 176] As a result, these additives enhance the stability of ACC against solid-state transformation such that the temperature required to initiate crystallization is significantly higher.[86, 122, 128, 176] For example, pure ACC transforms into calcite at 160 °C, whereas ACC particles that are synthesized in the presence of 35 mol% CIT only crystallize above 329 °C, as shown in Figure 1.10c.[176] Similar in-

creases in the critical crystallization temperature have been reported for ACC particles functionalized with PO_4^{3-} [86, 128] and Asp. [122]

Certain low molecular weight additives not only increase the stability of ACC, but also influence the size, structure, morphology, and properties of the resulting CaCO_3 crystals. For example, if high concentrations of CIT are present in bulk solutions, ACC preferentially transforms into the stable calcite rather than the metastable vaterite phase because CIT delays or even inhibits the growth of vaterite. [176, 186] As the CIT concentration increases, the size of the final calcite crystals decreases and their morphology changes from typical rhombohedra to elongated spheroids with rougher surfaces, as exemplified in the SEM images in Figure 1.10d. [176, 186] Remarkably, some organic additives, such as alanine, α -amino butyric acid, proline, or valine with a defined chirality can control the structure of the resulting crystals. [187] The presence of amino acids that possess a defined chirality, including Asp or glutamic acid, can even result in the formation of CaCO_3 crystals with chiral morphologies. [179, 185] For example, spiraling vaterite crystals with a well-defined chiral direction can form in the presence of L- or D- Asp, as shown in Figure 1.10e. [179] Moreover, these low molecular weight additives can influence the mechanical properties of the resulting crystals: If 7 mol% Gly or 4 mol% Asp are incorporated into calcite single crystals, their hardness increases two-fold, as shown in Figure 1.10f. [150]

1.4.3 High molecular weight additives

The formation of ACC is also influenced by certain high molecular weight soluble additives. By analogy to the influential low molecular weight additives, these polymeric additives possess functional groups with a high affinity to Ca^{2+} . A prominent example is PAA that strongly interacts with Ca^{2+} ions, thereby decreasing the degree of supersaturation of the solution and hence delaying the nucleation of ACC. [143] Sulfonate groups have a lower affinity towards Ca^{2+} than carboxylic groups such that the influence of sulfonate-containing additives such as PSS on the ACC formation kinetics [145] and their stability against crystallization [138] is lower than that of carboxyl-containing counterparts, such as PAA.

The attractive interaction between these additives and Ca^{2+} also leads to the formation of additive- Ca^{2+} complexes with a well-defined morphology. For example, the presence of PAA in Ca^{2+} containing solutions leads to the formation of crosslinked Ca-PAA polymer networks, as shown in Figure 1.11a. [53] This Ca-PAA system has

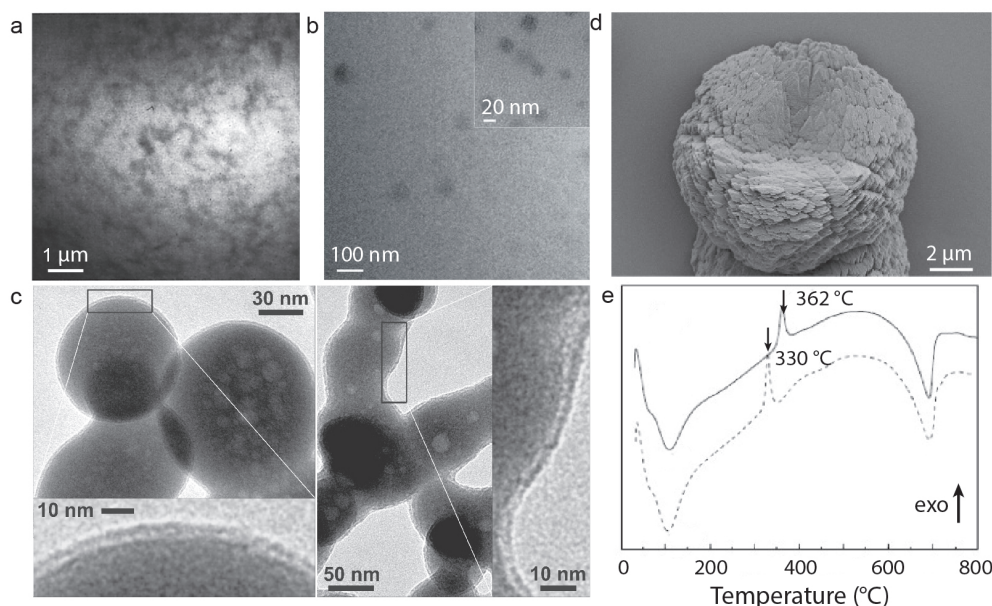


Figure 1.11 – Influence of high molecular weight additives on the formation of CaCO_3 . (a) X-ray microscopy image of Ca-PAA complexes.[53] (b) TEM images of Ca-PSS globules.[43] (c) TEM images of ACC particles coated with a silica shell.[190] (d) SEM image of a calcite crystal synthesized from an aqueous solution containing 5 mM Ca^{2+} ions in the presence of $0.5 \text{ g}\cdot\text{L}^{-1}$ PSS displaying a concave surface.[191] (e) DSC analysis of PSS-functionalized ACC particles that are synthesized in solutions encompassing a molar ratio of PSS:Ca of 1:4 (solid line) and 1:32 (dashed line). The critical crystallization temperatures are marked with arrows.[138]

recently been exploited to fabricate the physically-crosslinked hydrogels that are self-healable.[188, 189] Similarly, the presence of PSS in Ca^{2+} containing solutions leads to the formation of spherical globules, as shown in Figure 1.11b.[43] These complexes can also restrict the ion transport, thereby delaying the formation of ACC.[53]

Certain high molecular weight organic additives, such as PAsp,[44, 73] poly(arginine),[170] poly(allylamine hydro-chloride),[192] and ovalbumin[74] not only interact with Ca^{2+} or CO_3^{2-} ions but also induce the formation of CaCO_3 -rich liquid phases, namely Polymer-Induced Liquid Precursors (PILP) phases,[8, 44] or stabilize these phases after they formed.[71, 73, 74] In addition, these and many other high molecular weight additives containing multiple charged groups delay the ACC formation through one or a combination of these mechanisms.[145, 193–195]

High molecular weight additives are likely too big to be incorporated into ACC particles, such that they adsorb on their surfaces.[43, 53, 84, 196] Hence, they can also

be added after ACC particles are synthesized. Indeed, it has been demonstrated that PAsp stabilizes ACC particles more efficiently against crystallization if it is added to the suspension after the ACC particles have been synthesized.[196] In both cases, the kinetic stability of ACC particles against dissolution-reprecipitation increases with the concentration of high molecular weight additives present in the solution during their synthesis.[53, 61, 196] The resulting additive shell delays or even inhibits the ACC dissolution, if it is in contact with bulk water.[53, 61] It also hinders the diffusion of ions from the dissolving ACC particles to the forming CaCO_3 crystals, thereby retarding their growth.[43, 196] Similarly, ACC particles,[77, 190] or even PNCs[197] can be stabilized by coating them with an inorganic shell, silica, as shown in Figure 1.11c. In addition, the growth of the CaCO_3 crystals can be further slowed down if certain organic additives, such as PAsp,[198] that display a high affinity to the crystal surfaces are present. These results indicate that certain high molecular weight additives stabilize ACC particles by reducing the kinetics of the dissolution-reprecipitation process.

Some high molecular weight additives also influence the structure, size, and morphology of the resulting CaCO_3 crystals. For example, at low concentrations, PAsp promotes the formation of calcite.[196] With an increasing PAsp concentration, the size of calcite crystals decreases and their morphology changes from typical rhombohedra that possess smooth facets to those with rounded and rough surfaces.[198] If the PAsp concentration is further increased, vaterite forms.[196] A similar effect on the morphology of calcite is observed in the presence of PSS: At high PSS concentrations, faces of the calcite crystals, which are typically flat, become concave, as shown in Figure 1.11d.[191, 199] Certain high molecular weight additives also influence the kinetic stability of ACC against solid-state transformation, though they do not significantly change the degree of hydration of ACC.[122, 138, 170, 196] For example, the critical crystallization temperature of ACC particles increases from 277 °C to 362 °C if they are synthesized from a bulk solution containing a PSS : Ca ratio of 1:4, as shown in Figure 1.11e.[138] Similarly, the crystallization temperature of PAA-functionalized ACC particles increases with an increasing amount of PAA added during their synthesis.[138] Despite these observed differences in the kinetic stability, the mechanism how these additives influence the solid-state transformation is still unclear.

In summary, many additives strongly influence the formation of ACC and hence, its structure, hydration, and stability against crystallization. These additives also influence the size, structure, morphology, and hence, the properties of the result-

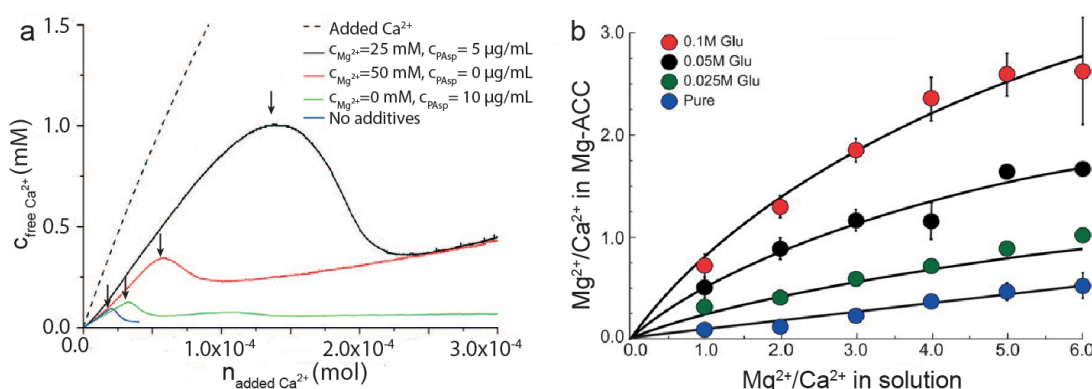


Figure 1.12 – Synergistic effects of multiple types of additives on the formation and composition of ACC. (a) Evolution of the concentration of free Ca^{2+} ions in a carbonate-buffered solution (pH = 9.75) upon continuous addition of a CaCl_2 -containing solution that does not contain any additives (blue) and contains PAsp (green), Mg^{2+} (red), or PAsp and Mg^{2+} (black). The total concentration of Ca^{2+} ions added to the solution is indicated by the dashed line. The points where ACC starts to form are marked with arrows.[200] (b) The molar ratio of Mg^{2+} and Ca^{2+} in Mg-ACC as a function of that in a solution that does not contain any additional additives (blue) and contains 0.025 M glutamic acid (green), 0.05 M glutamic acid (black), or 0.1 M glutamic acid (red).[201]

ing CaCO_3 crystals. If multiple types of additives are simultaneously present during the crystallization of CaCO_3 , an even closer control over the crystallization process can be achieved. For example, the formation of ACC is delayed more efficiently if Mg^{2+} is added to PAsp-containing solutions that are supersaturated with respect to ACC, as shown in Figure 1.12a.[200] Similarly, the amount of Mg^{2+} that is incorporated in Mg-ACC and hence, also in Mg-calcite, increases if certain low molecular weight carboxyl-containing additives are present during its synthesis, as shown in Figure 1.12b.[201] The increased Mg^{2+} concentration influences the mechanical properties of Mg-calcite.[174, 202] A better understanding of potential synergistic effects of different additives on the composition, structure, hydration, and crystallization of ACC would further our understanding on the CaCO_3 crystallization in nature. This understanding would also offer a better control over the crystallization process and hence the structure and properties of the resulting CaCO_3 -based materials.

1.5 Influence of insoluble organic scaffolds

To better understand the influence of insoluble organic scaffolds on the formation process of CaCO_3 , 2D organic substrates have been extensively studied. If appro-

priate additives such as PAA[203, 204] or PAsp[205] are used to functionalize ACC particles, the wettability of these particles[44, 206] is significantly enhanced such that they form continuous films that subsequently transform into crystalline ones on the substrate.[207–209] In this case, the structure of CaCO_3 films can be influenced by the composition of the organic substrate. For example, ACC particles preferentially transform into calcite films on hydroxyl-presenting surfaces like cellulose, whereas they principally transform into vaterite films on amine-presenting surfaces like chitosan, if PAA is present.[203] The structure of CaCO_3 films also depends on the crosslink density of the organic substrate: Vaterite films form on styrylpyridinium-modified poly(vinyl alcohol) (PVA) films if their crosslink density is sufficiently low and calcite films form if the crosslink density exceeds a threshold value.[154]

Similarly, the orientation of CaCO_3 crystals can be influenced by the composition of the organic substrate. This feature was explored to form crystalline CaCO_3 films with orientations that alternatively change over short length scales,[154, 210, 211] using a substrate made of polyrotaxane-modified PVA[211] or poly[(vinyl alcohol)-co-(vinyl acetate)],[154] as shown in Figures 1.13a-b. The orientation of CaCO_3 crystals also depends on the conformation of the polymers contained in the substrate and hence its stiffness: The *c*-axis of vaterite films produced on poly(*N*-isopropylacrylamide) brushes is oriented parallel to the substrate if grown at temperatures above the lower critical solution temperature (LCST), $T > \text{LCST}$, whereas it is oriented perpendicular to the substrate if grown at $T < \text{LCST}$. [212] Hence, certain insoluble organic substrates can offer a simultaneous control over the structure and orientation of CaCO_3 films. However, the exact mechanism by which it influences the structure and orientation of crystals remains unclear.

The formation of CaCO_3 crystals on the surfaces of insoluble organic substrate in the presence of soluble additives results in an additional benefit: It offers control over the shape of the resulting CaCO_3 . Taking advantage of this feature, CaCO_3 crystals with well-defined shapes were grown on patterned substrates made of photoresist,[152] polymer brushes containing carboxylic acid groups,[215] urease,[216] and poly(hydroxyethyl methacrylate-block-methylphenylsilane-block-hydroxyethyl methacrylate) copolymer.[217] Similarly, the shape of CaCO_3 crystals can also be controlled in three dimensions using 3D organic scaffolds with well-defined sizes and structures, such as epoxy resin membranes,[218] poly(2-hydroxyl methacrylate) hydrogels,[219], polymeric track-etched membranes,[34, 149, 214] self-assembled poly(styrene)-block-poly(isoprene) copolymers,[220], liquid crystalline

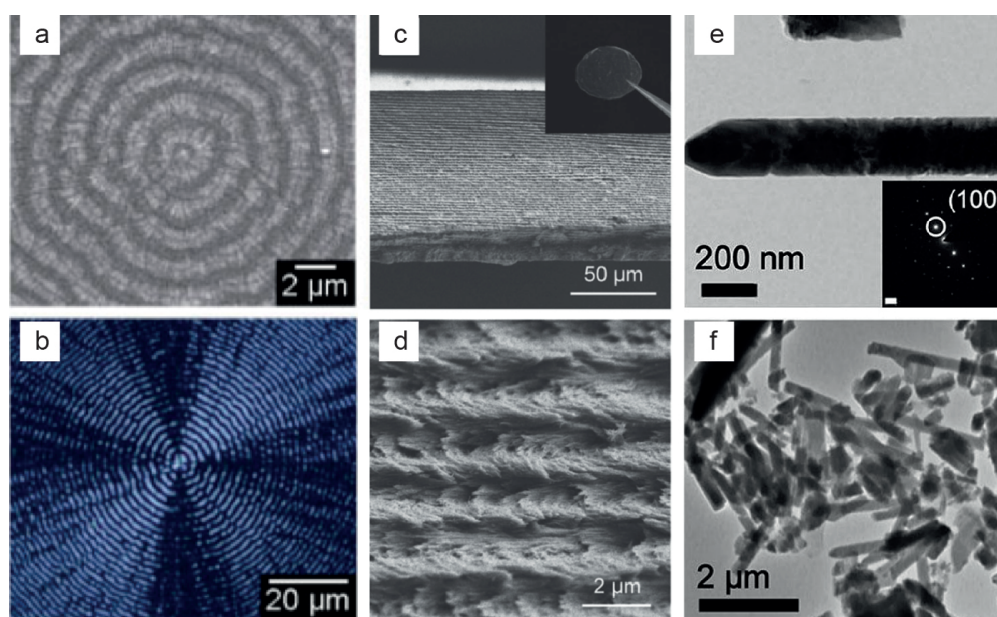


Figure 1.13 – Influence of insoluble organic scaffolds on the formation and composition of ACC. (a) SEM and (b) polarized light microscopy images of calcite films grown on a poly[(vinyl alcohol)-co-(vinyl acetate)] polymer substrate.[154] (c, d) SEM images of the cross section of CaCO_3 crystals grown on a liquid crystalline chitin/PAA film.[213] (e) TEM image and SAED pattern of single-crystalline vaterite nanowires formed within a Millipore track-etched membrane.[214]. (f) TEM image of a mixture of calcite and vaterite polycrystals formed within a Sterlitech track-etched membrane.[214]

chitin whiskers,[221], layered β -chitin matrix,[151] and de-mineralized natural organic scaffolds.[222]. For example, if ACC particles crystallize within liquid-crystalline chitin whiskers in the presence of PAA, a 3D chitin/ CaCO_3 composite with helical structures form, as shown in Figures 1.13c-d.[213]

During the formation of CaCO_3 crystals in the organic scaffolds, the formed ACC particles are often confined within the pores of insoluble organic scaffolds and hence, display an enhanced kinetic stability against crystallization.[34, 149, 214] The confinement restricts the transport of dissolved ions away from the ACC surface and hence, slows down the dissolution of ACC[223] as well as the nucleation and growth of new crystals.[224] As a result of this slower crystallization kinetics, the confinement provided by the organic scaffolds enables arresting crystals in a metastable form that displays an unusual morphology and a well-defined orientation; these effects depend on the surface chemistry of the confinement as well as their size.[149, 214] For example, if ACC particles are confined in nanopores of track-etched membranes

Introduction

that are produced from different manufacturers and thereby possess different surface chemistry, they can transform into CaCO_3 crystals with distinctly different morphology and orientations: In membranes purchased from Millipore single-crystalline vaterite nanowires form, whereas in membranes purchased from Sterlitech a mixture of calcite and vaterite polycrystals form under identical conditions, as shown in Figures 1.13e-f. [214] In addition, it has been shown that a reduced size of the nanopores of track-etched membranes promotes the formation of single-crystalline aragonite nanowires.[149]

These examples nicely demonstrate possibilities to control the formation of CaCO_3 crystals and thereby the structure and properties of CaCO_3 -based materials, through tuning the chemical composition, stiffness, structure, and pore size of insoluble organic scaffolds in the presence or absence of soluble additives.

2 Materials and Methods

This chapter is adapted from the experimental sections of our papers entitled: **(a)** “Amorphous CaCO_3 : Influence of the Formation Time on Its Degree of Hydration and Stability,” authored by H. Du, M. Steinacher, C. Borca, T. Huthwelker, A. Murello, E. Stellacci, and E. Amstad, and published in Journal of the American Chemical Society, vol. 140, pp. 14289–14299, Oct. 2018,[225], **(b)** “Additives: Their Influence on the Humidity- and Pressure- Induced Crystallization of Amorphous CaCO_3 ,” authored by H. Du, C. Courrégelongue, J. Xto, A. Böhlen, M. Steinacher, C. Borca, T. Huthwelker, and E. Amstad, and submitted in Oct. 2019.[226] and **(c)** “Fabrication of Hexagonal-Prismatic Granular Hydrogel Sheets,” authored by H. Du, A. Cont, M. Steinacher, and E. Amstad, and published in Langmuir, vol. 34, pp. 3459–3466, Mar. 2018.[227]

In this chapter, we describe the different experimental methods that are used to produce unfunctionalized ACC particles and those functionalized with a variety of soluble additives. We monitor the crystallization of these particles using various characterization techniques while employing different processing conditions, including elevated temperatures, humidity and pressures to induce the crystallization. Moreover, we detail the experimental approach to fabricate 2D structured organic scaffolds using emulsion drops as templates.

Contents

2.1	Materials	38
2.2	Studying the formation and crystallization of ACC using a spray dryer	39
2.2.1	Production of ACC particles using a spray dryer	39
2.2.2	Characterizations of as-produced ACC particles	41
2.2.3	Dehydration and crystallization of ACC particles	42
2.2.4	Electron beam-induced decomposition of ACC particles	44
2.3	Studying the influence of additives on the humidity- and pressure-induced crystallization of ACC	45
2.3.1	Production of ACC particles using a bulk solution method	45
2.3.2	Characterization of as-produced ACC particles	46
2.3.3	Pressure-induced crystallization of ACC particles	47
2.3.4	Humidity-induced crystallization of ACC particles	47
2.4	Fabricating 2D hexagonal prismatic granular hydrogel sheets	48
2.4.1	Production of drops	48
2.4.2	Self-assembly of hydrogel microparticles	49
2.4.3	Self-assembly and polymerization of drops	50
2.4.4	Characterizations	51

2.1 Materials

All the reagents are used as received. Calcium hydroxide (ACS reagent, $\geq 95.0\%$), calcite (ACS reagent, $\geq 99.0\%$), ethanol ($\geq 99.8\%$), glycine (ReagentPlus, $\geq 99.0\%$), citric acid (ACS reagent, $\geq 99.5\%$), acrylic acid (99%, anhydrous), magnesium chloride hexahydrate (ACS reagent, 99.0-102.0%), poly(acrylic acid) ($M_w \sim 100,000$ Da, 35 wt% in H_2O), poly(acrylic acid) ($M_w \sim 15,000$ Da, 35 wt% in H_2O), poly(acrylic acid) ($M_w \sim 450,000$ Da, powder), poly(allylamine) ($M_w \sim 15,000$ Da, 15 wt% in H_2O), poly(sodium 4-styrenesulfonate) ($M_w \sim 70,000$ Da, powder), poly(ethylene glycol) diacrylate ($M_n \sim 700$ Da), trichloro(1H,1H,2H,2H-perfluorooctyl)silane (97%), trichlorododecylsilane ($\geq 95.0\%$, Sigma-Aldrich), 2-hydroxy-2-methylpropiophenone

2.2. Studying the formation and crystallization of ACC using a spray dryer

(97%), fluorescein isothiocyanate–dextran ($M_w \sim 150,000$ Da) are purchased from Sigma-Aldrich. Calcium chloride ($\geq 98\%$, anhydrous) and sodium carbonate (ACS reagent, $\geq 99.5\%$, anhydrous) are purchased from Carl Roth. Dodecane ($\geq 99.0\%$) is purchased from ABCR, poly (dimethylsiloxane) (Sylgard 184) from Dow Corning, HFE 7500 from 3M Novec, and 2,2,3,3,4,4,4-heptafluoro-1 butanol from TCI. The fluorinated triblock copolymers surfactant, FSH-PEG900-FSH, is synthesized in our laboratory by Dr. Gianluca Etienne.[228]

2.2 Studying the formation and crystallization of ACC using a microfluidic spray dryer

2.2.1 Production of ACC particles using a spray dryer

To quench the formation of ACC particles at early stages, we produce them using a microfluidic spray dryer made of poly (dimethylsiloxane) (PDMS).[229] We employ a soft lithography process to fabricate the spray dryer.[230] To make the channels inside the spray dryer non-wetting for water drops, the surfaces of these channels are treated with dodecane containing 5 vol% trichlorododecylsilane. The spray dryer contains two inlets for liquids and six inlets for gases, as shown in Figure 2.1. During the operation of this device, drops form at the first liquid-gas junction and are sequentially accelerated by the gas that is injected through the additional gas inlets. They are collected on a solid substrate and subsequently fully dried by the gas flow that exits the microfluidic spray dryer.

To avoid any influence of counter ions such as Na^+ and Cl^- on the structure and stability of spray-dried ACC particles, unless stated otherwise, we produce them from an aqueous solution containing 2 mM $\text{Ca}(\text{OH})_2$ and expose it to CO_2 . To prepare this aqueous solution containing $\text{Ca}(\text{OH})_2$, a saturated solution of $\text{Ca}(\text{OH})_2$ (~ 23 mM) is first prepared by adding 2 g $\text{Ca}(\text{OH})_2$ in 1 L of deionized water (Direct-Q®, Merck Millipore, 25 °C) and stirring overnight. To avoid the formation of CaCO_3 precipitates, we degas water over night using N_2 . This solution ($\text{pH} \sim 12.6$) is filtered through a syringe filter ($0.2 \mu\text{m}$, CH-PTFE-20/25, HROMAFIL® Xtra) and diluted to 2 mM ($\text{pH} \sim 11.6$) immediately before the experiments. We inject this $\text{Ca}(\text{OH})_2$ -containing solution into the first liquid inlet at a flow rate of $1 \text{ mL} \cdot \text{h}^{-1}$ using a syringe pump (Cronus Sigma 1000, Labhut). The second liquid inlet is included for flexibility and blocked for these

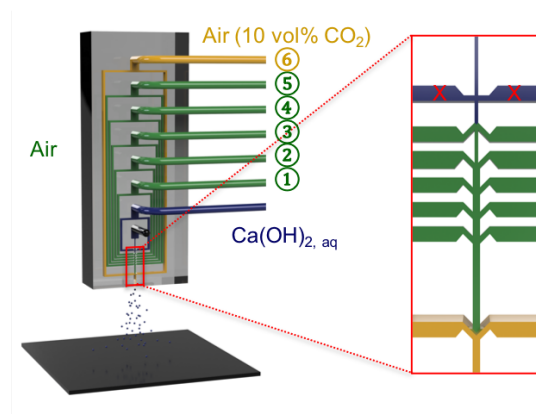


Figure 2.1 – Schematic illustration of the production of ACC nanoparticles using a microfluidic spray dryer. The spray dryer contains two inlets for liquids (blue) where one is used to inject an aqueous solution containing Ca(OH)_2 , and the other is blocked. In addition, the microfluidic spray dryer contains six inlets for air, five to inject unmodified air (green) and one to inject air enriched with 10 vol% CO_2 (brown).

experiments. To prevent precipitation reactions prior to drop formation, we form airborne drops containing Ca(OH)_2 using air. Drops are accelerated in the main channel by introducing additional air through inlets 2-5. To ensure complete conversion of Ca(OH)_2 into CaCO_3 , the air injected through the last inlet is enriched with 10 vol% CO_2 , which is produced by a gas mixer (KM60-2ME, Witt). We keep the pressure at all the air inlets constant at 0.3 MPa. Drops are collected on a silicon wafer or a carbon-coated TEM grid located 20 cm apart from the outlet of the device. After drops are fully dried by the gas flow existing the device, the solid particles are characterized.

To test the influence of the counterions of Ca^{2+} and CO_3^{2-} ions that are often involved in production of ACC particles, we inject an aqueous solution containing 4 mM CaCl_2 at $0.5 \text{ mL}\cdot\text{h}^{-1}$ into the first liquid inlet and the second aqueous solution containing 4 mM Na_2CO_3 at $0.5 \text{ mL}\cdot\text{h}^{-1}$ into the second liquid inlet of the device. In this case, all the six gas inlets are supplied with pure air.

To study how certain organic additives influence the formation and stability of ACC particles, we produce the particles that are functionalized with poly(acrylic acid) (PAA-100K, $M_w \sim 100,000 \text{ Da}$) through co-spray-drying. We add $50 \mu\text{g}\cdot\text{mL}^{-1}$ PAA-100K to the aqueous solution containing 2 mM Ca(OH)_2 . We inject this solution into the device and operate it under the same conditions.

2.2.2 Characterizations of as-produced ACC particles

Size

To measure the size of as-produced ACC particles that are quenched at different stages of their formation, we characterize them using a Zeiss Merlin field emission scanning electron microscope. The microscope is operated at an acceleration voltage of 6 kV and a probe of 100 pA. To avoid charging effects on the samples, they are coated with a 4 nm thick iridium film. Diameters of the particles are measured using the ImageJ software.

Composition and structure

To identify the composition and structure of the as-produced particles, we characterize them using FTIR and XRD. FTIR traces are recorded with a Nicolet 6700 spectrometer (Thermo Scientific) equipped with a Golden Gate Standard ZnSe Lenses ATR accessory (SPECAC) in the attenuated total reflection mode. Traces are acquired between 4000-600 cm^{-1} at a resolution of 4 cm^{-1} . For each trace, 32 scans are averaged. XRD traces are acquired using an Empyrean diffractometer (PANalytical) equipped with a PIXcel-1D detector. A Cu $K\alpha$ radiation source with a wavelength of 1.5405 Å is used as incident beam. To maximize the signal to noise ratio, traces are acquired at a grazing incident angle of 1°. The diffraction patterns are collected within a 2θ range of 15 to 50° and at a scanning rate of 0.1°·s⁻¹. For these measurements, the spray-dried ACC particles are directly collected on a one-side polished silicon wafer. We also characterize two reference samples, namely Ca(OH)₂ and calcite using the same techniques. Their crystalline peaks are identified with the HighScore Plus software.

To further quantify the structure of ACC particles, including their short-range order, we characterize them using XAS. All the XAS experiments are performed at the PHOENIX undulator beamline from the Swiss Light Source (Paul Scherrer Institut, Villigen, Switzerland), which provides photons in the tender X-ray region (0.8 to 8 keV). The size of the incident photon beam is 1 mm × 1 mm. The spray-dried ACC particles are directly deposited onto carbon-coated copper TEM grids. As the samples are monolayers of particles, there are no self-absorption effects that usually distort the fluorescence spectra in thick samples. Hence, their XAS spectra are acquired in the total fluorescence mode using a single element silicon drift diode (Ketek GmbH, Germany). By contrast, thick films of Ca(OH)₂ and calcite reference samples are deposited onto

a conductive carbon tape glued on a copper plate. Their spectra are acquired in the total electron yield mode, which is self-absorption free. All the obtained XAS spectra are corrected by measuring the incident photon flux with a nickel-coated polyester foil that is placed in front of the samples. X-ray absorption near-edge structure spectra are normalized using the Demeter software.[231] Extended X-ray absorption fine structure spectra are measured up to $k = 10 \text{ \AA}^{-1}$ with a step size of 0.05 \AA^{-1} . Fitting is conducted with k^2 -weighted data in the R -space using the Artemis software.[231] The small peaks in the k -space data caused by multielectron excitations are not removed since it has been shown that they do not significantly influence the fitting results.[232] Theoretical phase and scattering amplitude functions used for fitting Ca-O scattering are calculated using calcite as a model system.[76, 93]

Morphology

To investigate the morphology of ACC particles that are quenched at different stages of their formation, we visualize them using TEM. Transmission electron microscopy images of the particles are taken in a field emission Talos transmission electron microscope (FEI) using an acceleration voltage of 200 kV. The condenser aperture 1 is $2000 \mu\text{m}$ and the condenser aperture 2 is $100 \mu\text{m}$. The ACC particles are directly sprayed to carbon film-coated copper grids. The dose of electrons is kept constant at $60 \text{ e} \cdot \text{\AA}^{-2} \cdot \text{s}^{-1}$ and the magnification is kept constant at 190,000 x. In addition, we measure the structure of particles using the SAED in TEM. SAED patterns are collected using a $10 \mu\text{m}$ aperture.

2.2.3 Dehydration and crystallization of ACC particles

To study how n of ACC influences its morphology and structure, we dehydrate the spray-dried ACC particles through thermal annealing unless stated otherwise. ACC particles that are deposited onto carbon film-coated molybdenum TEM grids are heated in a nitrogen atmosphere using a Thermogravimetry Analysis 4000 (Perkin Elmer) at a rate of $10 \text{ }^\circ\text{C} \cdot \text{min}^{-1}$ before they are kept at the desired temperature for 3 h. Similarly, particles that are deposited onto a silicon wafer are annealed in a muffle furnace (France-Etuves) at the desired temperature for 3 h. To study how n influences the kinetic stability of ACC against the temperature-induced crystallization, we crystallize the spray-dried ACC particles through annealing them at more elevated temperatures using similar protocols. For certain experiments, we also use a vacuum

2.2. Studying the formation and crystallization of ACC using a spray dryer

drying method to dehydrate ACC particles, where particles are kept in a vacuum desiccator (VWR) for 2 months.

Degree of hydration

To measure n of ACC particles during their dehydration and temperature-induced crystallization, we characterize the as-produced particles and those that have been annealed at different temperatures using XPS. X-ray photoelectron spectroscopy measurements are carried out using a PHI VersaProbe II scanning XPS microprobe (Physical Electronics) with monochromatic Al K α X-ray source operated at 24.8 W. The beam size of the X-ray source is 100 μm . For these measurements, samples are deposited onto a silicon wafer that is coated with a 20 nm thick platinum film to avoid any oxygen contribution from the substrate. Data is analyzed using the CasaXPS software. All the binding energies are calibrated with the carbon 1s peak at 285 eV.[233] To measure the atomic ratio of O to Ca for ACC, we fit the Ca 2p and O 1s XPS peaks, integrate their areas, and divide them by their relative sensitivity factors[234] provided by the CasaXPS software. Using the same procedure, we quantify O/Ca for a calcite reference. Because calcite does not contain any water, its O/Ca should be 3. We therefore use this measurement to normalize all our values of O/Ca by setting that of calcite to 3.

Morphology

The morphology of the dehydrated and crystallized ACC particles is visualized with TEM using similar parameters as described in Section 2.2.2.

Structure

To quantify the evolution of structures of ACC particles during their dehydration and subsequent crystallization at elevated temperatures, we characterize the particles using XAS while they are heated *in situ*. A resistive heating system (ISOHEAT Mil Heating Systems GmbH, Germany) is used to vary the temperatures. The temperatures are monitored using a Pt100 resistive sensor connected to the sample holder. X-ray absorption spectra are acquired and analyzed using similar protocols as described in Section 2.2.2. Similarly, to monitor the evolution of structures, we also determine the full width half-maximum (FWHM) of the Ca 2p_{3/2} peak for the as-produced particles

and those that have been annealed at different temperatures measured with XPS. To identify the structure of crystallized ACC particles, we acquire their SAED patterns using TEM.

Surface roughness

To relate the change of structures of ACC particles to their dehydration, we image the surface of particles before and after having been annealed at 200 °C for 3 h with atomic force microscopy (AFM). Atomic force microscopy measurements are conducted in ambient conditions in the amplitude modulation mode on a Cypher S system (Asylum Research/Oxford Instruments). The sensitivity of the cantilevers (AC240TS, Olympus) and their spring constant are calibrated using the built-in GetReal™ Automated Probe Calibration procedure. The cantilevers are driven acoustically. The values of the free amplitude are in the range of 10-20 nm, with a relative set-point amplitude of 75%. The scan rates are in the range 3–5 Hz. The ACC particles are directly deposited onto carbon-coated copper TEM grids. Image analysis is performed in Gwyddion[235] (<http://gwyddion.net/>) and power spectral density (PSD) function is calculated using the built-in function. Power spectral density function is a Fourier transform of the autocorrelation function and represents the contributions of different spatial length scales to the fluctuations in the topography. It therefore provides a global evaluation of the surface roughness of the particles. To avoid the artifacts caused by the background, the power spectral density function analysis is conducted on an inscribed rectangular region of the surface of each nanoparticle.

2.2.4 Electron beam-induced decomposition of ACC particles

To investigate the stability of ACC particles against electron beam-induced decomposition, we image the particles using TEM with an increased electron dose of 400 e·Å⁻²·s⁻¹ and record the evolution of their morphology under such conditions.

2.3 Studying the influence of additives on the humidity- and pressure- induced crystallization of ACC

2.3.1 Production of ACC particles using a bulk solution method

To study the influence of additives on the humidity- and pressure- induced crystallization of ACC, we produce unfunctionalized ACC particles and those functionalized with a variety of additives using a bulk solution method. The throughput of this method is approximately three orders of magnitude higher than that obtained using the spray drying method, thereby enabling us to form bulk samples to which we can easily apply different pressures with our current experimental set-up. In addition, this significantly higher throughput allows us to characterize n of ACC with the widely used TGA method, which was not accessible for the spray-dried ACC particles because of the small amounts of particles that are produced.

We employ additives that are often used to control the crystallization of ACC in bulk solutions or at elevated temperatures, including certain low molecular weight additives, such as magnesium chloride hexahydrate (Mg), Gly, CIT, and acrylic acid (AA), as well as certain polymeric additives, such as poly(acrylic acid) with a $M_w \sim 15,000$ Da ((PAA-15K), poly(acrylic acid) with a $M_w \sim 450,000$ Da (PAA-450K), poly(sodium 4-styrenesulfonate) with a $M_w \sim 70,000$ Da (PSS-70K) and poly(allylamine) with a M_w of 15,000 Da (PAL-15K), as summarized in Figure 2.2. To compare the influence of different additives, we fix the molar ratio of the low-molecular weight additives or the repeat units for the polymeric additives to Ca^{2+} present in the initial solution to 1: 10. In the synthesis, 1.75 mL of an aqueous solution containing 0.1 M low molecular weight additives or repeating units of polymeric additives is mixed with 1.75 mL of an aqueous solution containing 1 M CaCl_2 for 10 min using an ultrasonic bath. In addition, 3.5 mL of an aqueous solution containing 0.5 M Na_2CO_3 is prepared. All solutions are stored at 4 °C for at least 2 h. The solution containing 0.5 M Na_2CO_3 is then added to the solution containing CaCl_2 and additives and vortexed for 10 s. To quench the precipitation reaction, 40 mL cold ethanol (4 °C) is added after the reaction carried out for 30 s and the mixture is again vortexed for 10 s. To extract the precipitates, the mixture is centrifuged at 4500 rpm for 5 min at 4 °C before the supernatant is removed. The resulting ACC particles are washed twice, each time with 35 mL ethanol, before the ACC particles are dried and stored in a vacuum desiccator. For CIT-functionalized ACC, we also synthesize samples where we lower the concentration of CIT three-fold

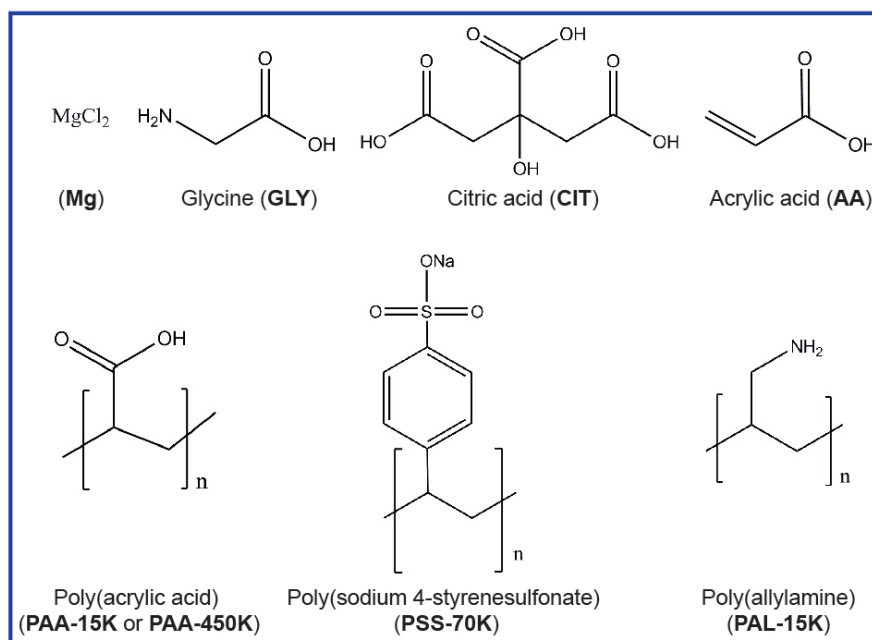


Figure 2.2 – Chemical structures of the additives used to functionalize ACC with their abbreviations indicated in parenthesis. The molecular weights of polymer additives are given in the brackets.

using the same protocol. To synthesize unfunctionalized ACC particles as controls, we prepare 3.5 mL of an aqueous solution containing 0.5 M CaCl_2 and mix it with 3.5 mL of an aqueous solution containing 0.5 M Na_2CO_3 . All the following steps are same as those in the synthesis of additive-functionalized ACC.

2.3.2 Characterization of as-produced ACC particles

Size

To measure the size of as-produced ACC particles synthesized using the bulk solution method, we characterize all the synthesized ACC samples using SEM under same operation conditions as described in Section 2.2.2. All the samples are coated with a 20 nm thick film of Au:Pd (80:20) to avoid charging effects.

Composition and structure

To identify the composition and structure of as-produced particles, we characterize them using FTIR and XRD as described in Section 2.2.2. Because we obtain much

2.3. Studying the influence of additives on the humidity- and pressure- induced crystallization of ACC

higher amounts of ACC using the bulk solution method, XRD patterns of all the ACC samples are acquired in the normal gonio scan mode instead of the grazing incidence mode. To conduct the measurements, sample powders are deposited on glass slides (Corning®).

Degree of hydration

To quantify n of the produced ACC samples, we characterize them using a TGA 4000 instrument. For each measurement, approximately 5 mg of ACC powders are placed into an alumina crucible. The crucible is heated from 30 °C to 800 °C at a rate of 10 °C·min⁻¹ under a flow of dry N₂ whose rate is kept constant at 20 mL·min⁻¹.

2.3.3 Pressure-induced crystallization of ACC particles

To perform the pressure-induced crystallization experiments, we use a programmable hydraulic press (PressPRO, PIKE Technologies) to precisely apply the pressures to ACC particles. We employ a cylindrical die with an inner diameter of 13 mm that is typically used for pressing KBr pellets for FTIR measurements to fabricate the samples. We add approximately 30 mg of ACC powder to the pellet die and subject the powder to well-defined pressures. In the first set of experiments, we apply pressures between 87 and 738 MPa to the ACC samples for 30 min to induce their crystallization. For the additive-functionalized ACC samples that do not crystallize at 738 MPa, which is the highest pressure that can be applied with this set-up, we fix the pressure at 738 MPa and extend the pressing time to induce the crystallization. To study the kinetics of the pressure-induced crystallization, we characterize the structure of ACC samples after having been pressurized using FTIR and XRD, their n using TGA, and their size as well as morphology using SEM.

2.3.4 Humidity-induced crystallization of ACC particles

To perform the humidity-induced crystallization experiments, we deposit a layer of ACC powder on an aluminum tape that is glued to the bottom of a humidity chamber. We supply 20 mL·min⁻¹ N₂ to the humidity chamber to keep the RH constantly around 95%. To monitor the kinetics of the humidity-induced crystallization *in situ*, we place the humidity chamber containing the ACC sample under a Hyperion 3000 Fourier Transform infrared microscope (Bruker) and measure it using an Invenio FTIR spec-

trometer (Bruker). FTIR spectra are measured from 650 to 4000 cm^{-1} with a resolution of 4 cm^{-1} in the reflection mode. For each measurement, 60 scans are averaged. To minimize potential errors in the quantification of the degrees of crystallization that are caused by shifts of the baselines occurring during the crystallization, we fit the baseline of each absorption peak of the *in situ* FTIR traces using a spline interpolation and subtract it from the measured peaks using the OriginPro software. For certain ACC samples, we also measure their structure *ex situ* with FTIR as described in Section 2.2.2.

To quantify the evolution of n of ACC during the humidity-induced crystallization, we characterize ACC samples that have been exposed to the humid environment for different durations using TGA. To measure the size and morphology of ACC samples crystallized in the humid environment, we characterize them with SEM. To test the orientation of CaCO_3 crystals obtained from the humidity-induced crystallization, the crystallized sample is characterized using TEM and SAED, as described in Section 2.2.2. To prepare the sample, an ethanol suspension of ACC particles is deposited to a carbon film-coated copper grid before ethanol evaporates. The sample is subsequently placed in the humidity chamber to crystallize the ACC particles.

2.4 Fabricating 2D hexagonal prismatic granular hydrogel sheets

2.4.1 Production of drops

We produce emulsion drops that act as templates for fabricating 2D structured hydrogel sheets using a microfluidic millipede device made of PDMS.[236] This device enables the production of monodisperse drops with a very high throughput. It consists of a central channel for the inner phase and on each of the two long sides of the central channel there is a channel for the oil phase, as shown in Figure 2.3. The central channel is connected to the two outer channels through 300 individual drop makers that have a much smaller height such that there is a step at the end of each drop maker. The nozzle of the drop makers opens in a triangular way. For a proper functioning of the device, the channel walls must be non-wetting for the inner phases. To produce water-in-oil single emulsion drops, we treat the channel walls with an HFE 7500-based solution containing 1 vol% trichloro(1H,1H,2H,2H-perfluorooctyl)silane.

2.4. Fabricating 2D hexagonal prismatic granular hydrogel sheets

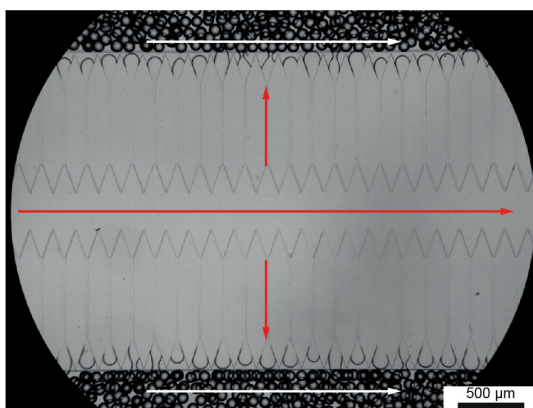


Figure 2.3 – Optical image of a section of the microfluidic millipede device in operation. The red arrows indicate the flow direction of the inner aqueous solution and the white arrows indicate the flow direction of the HFE 7500 oil.

To produce emulsion drop templates that can be converted into hydrogels through UV-initiated polymerization, an aqueous solution containing 50 wt% poly(ethylene glycol) diacrylate (PEG700-DA, $M_w \sim 700$ Da) monomers and 2 wt% 2-hydroxy-2-methylpropiophenone photoinitiators is used as the inner phase. A perfluorinated HFE 7500 oil with 1 wt% fluorinated triblock copolymers surfactant, FSH-PEG900-FSH, is used as the outer phase. These two phases are injected into the millipede devices using syringe pumps. The produced drops are collected in a glass vial that is wrapped in aluminium foil to protect the collected drops from light exposure. To produce fluorescently labeled drops, we add $0.1 \text{ mg} \cdot \text{mL}^{-1}$ fluorescein isothiocyanate–dextran (FITC-Dextran) to the aqueous phase containing the monomers and photoinitiators.

2.4.2 Self-assembly of hydrogel microparticles

As control experiments, we fabricate structured hydrogel sheets through the self-assembly of individual hydrogel microparticles. To convert drop templates into hydrogel microparticles, they are illuminated with UV light ($320 \text{ nm} < \lambda < 500 \text{ nm}$) that is guided by a liquid light guide with a diameter of 8 mm (Ominicure S 1000, Lumen Dynamics, Canada). The polymerized hydrogel microparticles are washed three times with 2,2,3,3,4,4,4-heptafluoro-1 butanol to remove the surfactant and subsequently dispersed into an aqueous solution. We add 20 vol% ethanol to the aqueous dispersion containing the hydrogel microparticles to lower the surface tension of the solvent, thereby facilitating the spreading of the dispersion on the solid substrate; this is required to produce a monolayer of microparticles. We deposit a few drops of this

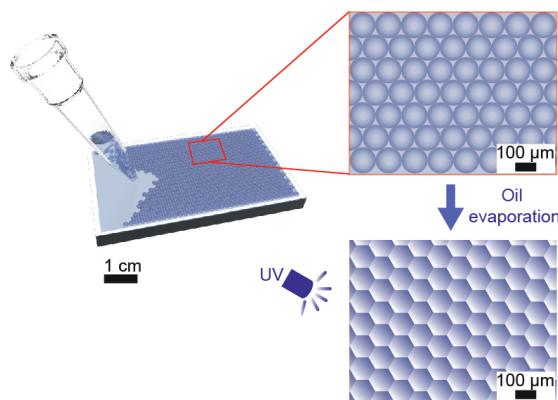


Figure 2.4 – Schematic illustration of the formation of hexagonal prismatic granular hydrogel sheets. Emulsion drops are deposited on a substrate where drops arrange into the energetically most favorable hexagonal close packed structure. Once the majority of the oil is evaporated, drops deform and attain a hexagonal prismatic shape. They are subsequently illuminated with UV light to convert them into hydrogel particles that are linked through their side walls.

dispersion onto a PDMS substrate and let the particles sediment. We subsequently vortex the sample to agitate the particles, thereby facilitating their arrangement into a hexagonal close packed structure monolayer.

2.4.3 Self-assembly and polymerization of drops

To fabricate structured hydrogel sheets with a better integrity, we first deposit the emulsion drops onto a clean glass slide or into a 25 mm long, 4 mm wide and 120 μm deep PDMS trough, as shown in Figure 2.4. The density of water is 1.6 times lower than that of the oil such that drops cream inside the collection vial. We remove part of the oil to increase the drop concentration before the deposition. After the drops self-assemble into a monolayer, excessive drops are removed using a micropipette. While the oil evaporates, drops attain a hexagonal prismatic shape. We subsequently illuminate them with UV light for 15 s to solidify the deformed emulsion drops. The distance between the sample and the end of the light guide is kept constant at 3 cm unless stated otherwise. At this distance, the illumination intensity is around $1.20 \text{ W}\cdot\text{cm}^{-2}$, as measured with a radiometer (Suss MicroTec UV optometer). If we vary the distance from 1 cm to 15 cm, the irradiance shifts from $4 \text{ W}\cdot\text{cm}^{-2}$ to $0.06 \text{ W}\cdot\text{cm}^{-2}$.

2.4.4 Characterizations

Interfacial tension

The contact angle between the aqueous solution containing PEG-DA and the substrate as well as the interfacial tension between the PEG-DA solution and the oil is measured using a drop shape analyzer (DSA25, Kruss, Germany).

Microscopy

All the samples are visualized with optical microscopes (Eclipse TS 100 and Ti-E, Nikon, Japan). Some samples are also characterized using SEM (XLF30-FEG, FEI, USA). Scanning electron microscopy images are acquired at an acceleration voltage of 3 kV using a secondary electron detector. To avoid charging effects, they are coated with a 30 nm thick gold film.

Mechanical properties of hydrogel sheets

We measure the Young's modulus of the hydrogel sheets using a tensile tester (MiniMat 2000, Rheometric Systems). Sample sheets are dried in air at room temperature for at least 2 days before the measurements. These sheets are immobilized with two clamps that are coated with a 1 mm thick PDMS layer to avoid sample damage. We measure the applied force as a function of the strain and calculate the stress by dividing the force by the cross section area of the sample, which we quantify by measuring its width using optical microscopy and its thickness using a digital micrometer.

3 Influence of the Formation Time on the Degree of Hydration and Stability of ACC

This chapter is adapted from the paper entitled “Amorphous CaCO_3 : Influence of the Formation Time on Its Degree of Hydration and Stability,” authored by H. Du, M. Steinacher, C. Borca, T. Huthwelker, A. Murello, F. Stellacci, and E. Amstad, and published in Journal of the American Chemical Society, vol. 140, pp. 14289–14299, Oct. 2018.[225] H. Du and E. Amstad designed the experiments. H. Du performed all the experiments except for the AFM measurements that were conducted by A. Murello. The analysis of AFM results were done by H. Du and A. Murello under the supervision of F. Stellacci. M. Steinacher contributed to the optimization of spray-drying process and the material characterizations. C. Borca and T. Huthwelker helped with the collection and analysis of XAS data. H. Du and E. Amstad analyzed all data and wrote the paper.

In this chapter, we use a microfluidic spray dryer to study the early stages of the ACC formation with a high temporal resolution without the need of any organic solvents. We demonstrate that the amount of mobile water contained in ACC particles increases as the particles grow, rendering them kinetically less stable against the temperature-induced solid-state crystallization. We also find that certain additives known to delay the crystallization of ACC, such as PAA, reduce the amount of mobile water contained in ACC, thereby increasing their kinetic stability.

Contents

3.1	Introduction	54
3.2	Results	56
3.2.1	Production of ACC particles through spray-drying	56
3.2.2	Influence of the formation time on the degree of hydration of ACC particles	57
3.2.3	Mobility of water contained in ACC particles	64
3.2.4	Influence of mobile water on the stability of ACC particles . . .	67
3.2.5	Influence of poly(acrylic acid) on the stability of ACC particles	69
3.3	Discussion	71
3.4	Conclusion	73

3.1 Introduction

Many different processing conditions, such as the pH[28, 60] and temperature[93] of the aqueous solutions that are used to synthesize ACC particles, as well as the methods to dry particles[117] have been shown to influence the formation pathways,[60] structure,[92, 93] and stability[40, 40, 129] of ACC particles. The stability of ACC particles, which is directly related to their size,[65, 80] is also influenced by the amount of water contained in them.[40, 87, 129] Whether the amount of water contained in ACC particles is influenced by the synthesis conditions remains to be determined. To experimentally study the influence of the synthesis conditions on the degree of hydration and the stability of ACC particles, the formation of ACC particles must be quenched at early stages with a temporal resolution of the order of milliseconds.[58]

The formation of ACC is often quenched with organic solvents, such as ethanol, which CaCO_3 has a low solubility in.[40, 77, 87] Indeed, the presence of these organic solvents influences the degree of hydration,[77, 117, 237] structural order,[90] stability,[139] and crystallization pathway[238] of ACC. Hence, the differentiation between effects that are inherent to ACC from those that have been induced by organic solvents is very difficult. The time required to quench the formation of ACC with this method is usually of the order of minutes.[43, 239] Recently, some *in situ* liquid cell TEM[31, 43] and cryo-TEM[48, 240] studies have been employed to investigate the early stages of

CaCO_3 formation with a resolution of a few seconds, although feasibility to achieve a resolution down to 100 ms has been shown.[61] However, the information that has been extracted from these measurements is limited to the size, crystallinity, and morphology of particles. There are a few reports that employ TEM images to extract the degree of hydration of ACC particles from the image contrast.[57, 61] However, more systematic and quantitative studies on the influence of processing conditions on the composition of ACC particles, including their degree of hydration, remain elusive. To gain a better understanding of the correlation between processing conditions and the degree of hydration of ACC particles, it would be beneficial to establish a technique that quenches the formation of ACC during early stages without the need for organic solvents and without embedding them in a matrix that prevents further chemical analysis.

In this chapter, we employ a microfluidic spray dryer[229] to quench the formation of ACC particles at early stages by producing these particles in airborne aqueous drops that rapidly dry; this process does not require any organic solvents to quench the particle formation. To study the formation of ACC particles with a high temporal resolution, we vary the diameter of drops from 10 to 100 μm such that the formation time of ACC particles ranges from 100 ms to 10 s. We find that the amount of mobile water incorporated in ACC particles increases with increasing formation time and hence with increasing particle size. Because of the increased amount of mobile water, larger particles are more prone to temperature-induced crystallization and electron beam-induced decomposition than smaller counterparts. In line with these observations, we find that additives known to delay or even inhibit the crystallization of ACC, such as PAA, reduce the mobility of water contained in ACC, thereby increasing their kinetic stability. These results indicate that the kinetics of crystallization of ACC particles is directly related to the amount of mobile water contained in ACC particles. These insights offer new opportunities to tune the stability of ACC with its degree of hydration and thereby facilitate its processing into biomimetic CaCO_3 -based materials with tunable structures and properties.

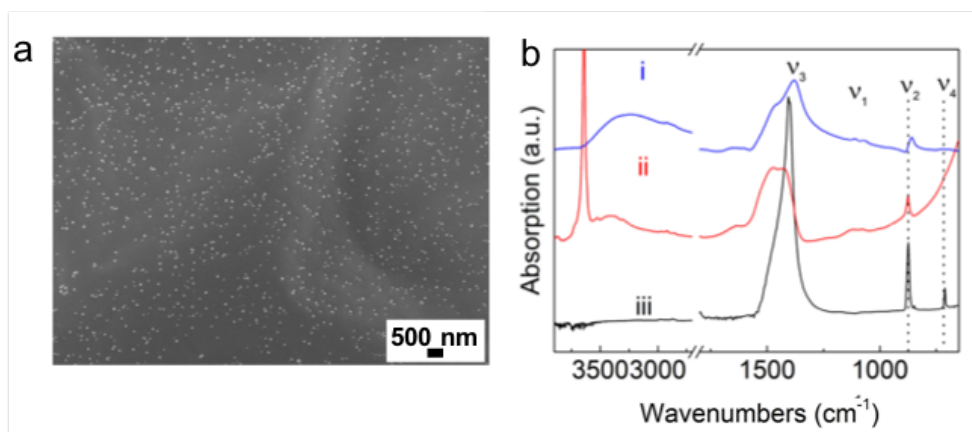


Figure 3.1 – Characterization of the morphology and composition of the spray-dried CaCO_3 nanoparticles. (a) SEM image of the spray-dried nanoparticles. (b) FTIR traces of the spray-dried nanoparticles (i) and reference traces of Ca(OH)_2 (ii) and calcite (iii). Ca(OH)_2 reference contains small amounts of calcite.

3.2 Results

3.2.1 Production of ACC particles through spray-drying

We produce ACC nanoparticles with a PDMS-based microfluidic spray dryer[229] that is fabricated using soft lithography.[230] Nanoparticles are produced inside aqueous drops containing Ca(OH)_2 that are dried using CO_2 -enriched air, as schematically shown in Figure 2.1. The resulting dry nanoparticles are well separated from each other, as shown in the SEM image in Figure 3.1a. To test if this spray-drying process is sufficient to fully convert Ca(OH)_2 into CaCO_3 , we characterize spray-dried particles using FTIR. The spray-dried particles do not display any sharp absorption peak at 3640 cm^{-1} that corresponds to the OH stretch vibration and is prominent in the reference trace of Ca(OH)_2 , as shown in Figure 3.1b. This result suggests that spray-dried particles do not contain significant amounts of Ca(OH)_2 . Instead, spray-dried particles display an ν_2 absorption peak at 863 cm^{-1} and they do not show any ν_4 peak around 712 cm^{-1} . The location of the ν_2 peak and the absence of the ν_4 peak measured for the spray-dried sample is characteristic for ACC.[33, 81, 157, 241] Hence, our FTIR results suggest that Ca(OH)_2 is fully converted into ACC during the spray-drying process. The FTIR spectrum of spray-dried particles also displays a broad absorption peak in the region of $2750\text{--}3600\text{ cm}^{-1}$ and a small peak around 1640 cm^{-1} ; these peaks are characteristic for water contained in ACC,[33, 157] suggesting that spray-dried particles contain significant amounts of water.

To confirm the structure and composition of spray-dried particles, we perform XAS measurements on the Ca K-edge and compare the spectrum measured for spray-dried particles to the reference spectra of $\text{Ca}(\text{OH})_2$ and calcite; calcite is the most stable crystalline form of CaCO_3 at room temperature and ambient conditions for particles whose diameter exceeds 4 nm.[28, 80, 87] X-ray absorption near-edge structure spectra of spray-dried particles display a small pre-edge peak at 4040 eV and a single main absorption edge at 4049 eV but they do not show any shoulder around 4045 eV, as shown in Figure 3.2a. These features are in stark contrast to the reference spectra acquired on calcite, indicating that our particles are composed of ACC, in good agreement with previously reported results for ACC particles produced in bulk.[76, 105, 106, 241] To characterize the short-range order of spray-dried ACC particles, we fit the EXAFS regions of the XAS traces of the particles. The k -space oscillation of the EXAFS and its Fourier transformation with a k -range of 2.4-8.0 \AA^{-1} in the R -space are shown in Figures 3.2b-c. Fits of these measured traces reveal that R of the first oxygen coordination shell around calcium is $2.4 \pm 0.04 \text{ \AA}$ and the corresponding CN is 6.4 ± 3.3 . No additional, more distant shells are observed, in stark contrast to crystals, suggesting that our particles are amorphous.[76] Our EXAFS results agree well with those reported for ACC particles produced in bulk,[76, 106, 107] providing evidence that the spray-dried ACC particles possess a similar short-range order. To further confirm the amorphous structure of spray-dried particles, we perform XRD on the samples. In agreement with our previous results, we do not observe any sharp diffraction peak in the XRD trace of the spray-dried sample, in stark contrast to the reference samples, as shown in Figure 3.2d.

3.2.2 Influence of the formation time on the degree of hydration of ACC particles

To test the influence of the formation time of ACC particles on their sizes, degrees of hydration and structures, we produce them in airborne drops with different sizes such that the time during which particles can form inside drops varies. This formation time is directly related to the drying time of drops: Particles start to form when the solute concentration exceeds its saturation concentration and their formation is quenched when the drop is fully dried. We approximate the particle formation to be initiated when drops exit the device where they are exposed to higher concentrations of CO_2 such that the formation time of particles is very similar to the drying time of drops. Indeed, as the speed of drops that exit the outlet of device is very high ($\sim 10 \text{ m} \cdot \text{s}^{-1}$),

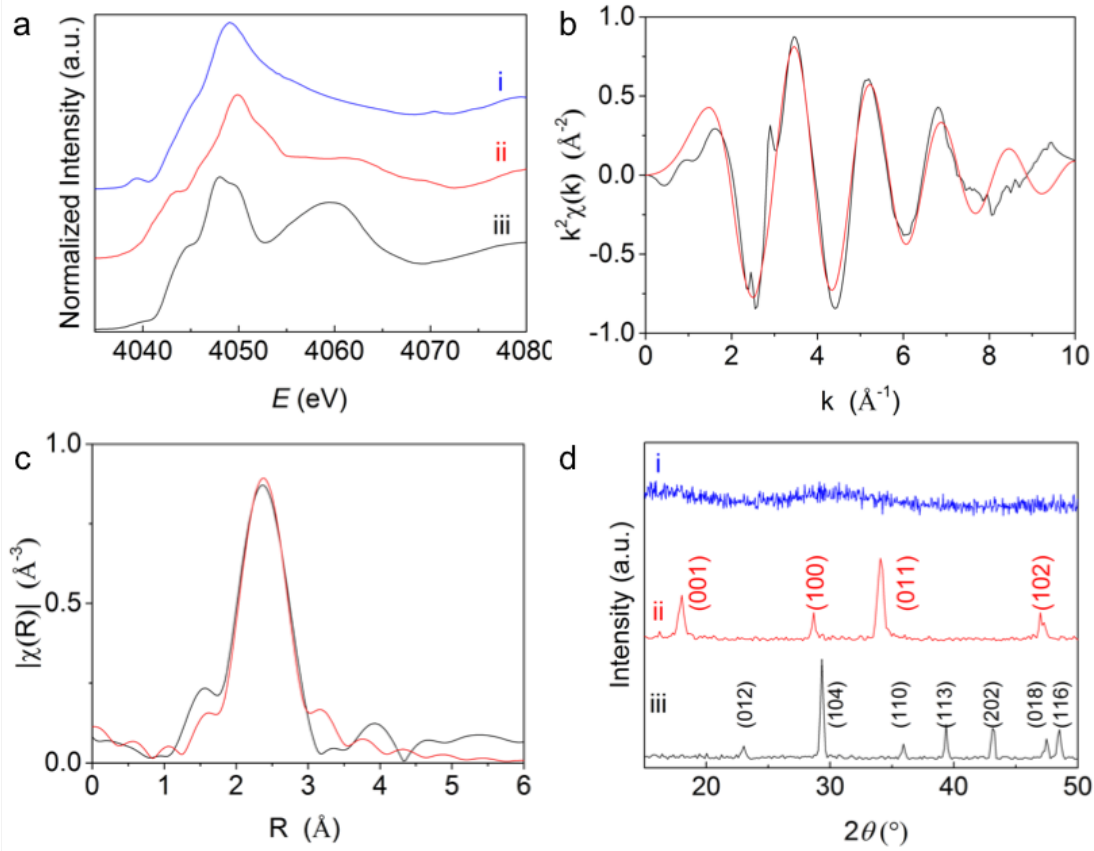


Figure 3.2 – Characterization of the structure of the spray-dried CaCO_3 nanoparticles. (a) Ca K-edge XANES spectra of the spray-dried nanoparticles (i) and reference traces of Ca(OH)_2 (ii) and calcite (iii). (b,c) Measured (black) and fitted (red) Ca K-edge EXAFS traces of the spray-dried nanoparticles (b) in the k -space and (c) its Fourier transform in the R -space. (d) XRD patterns of the spray-dried nanoparticles (i), Ca(OH)_2 (ii), and calcite (iii).

we can neglect the time during which drops fly freely, which is after they exit the device and before they hit the substrate (~ 20 ms). Instead, we only consider the time required to dry drops after they are deposited on a solid substrate, which depends on the sizes and evaporation rates of drops.

To quantify the sizes of drops produced by the spray dryer, we calculate their volume (V) from the diameter (d_{cl}) of the contact line and the contact angle (θ) of drops with the substrate after they are deposited. We assume the shape of drops on the substrate to be a spherical cap, as schematically shown in Figure 3.3a, which is a good approximation for the small drops produced here. We calculate the volume of drops using Equation 3.1,[242]

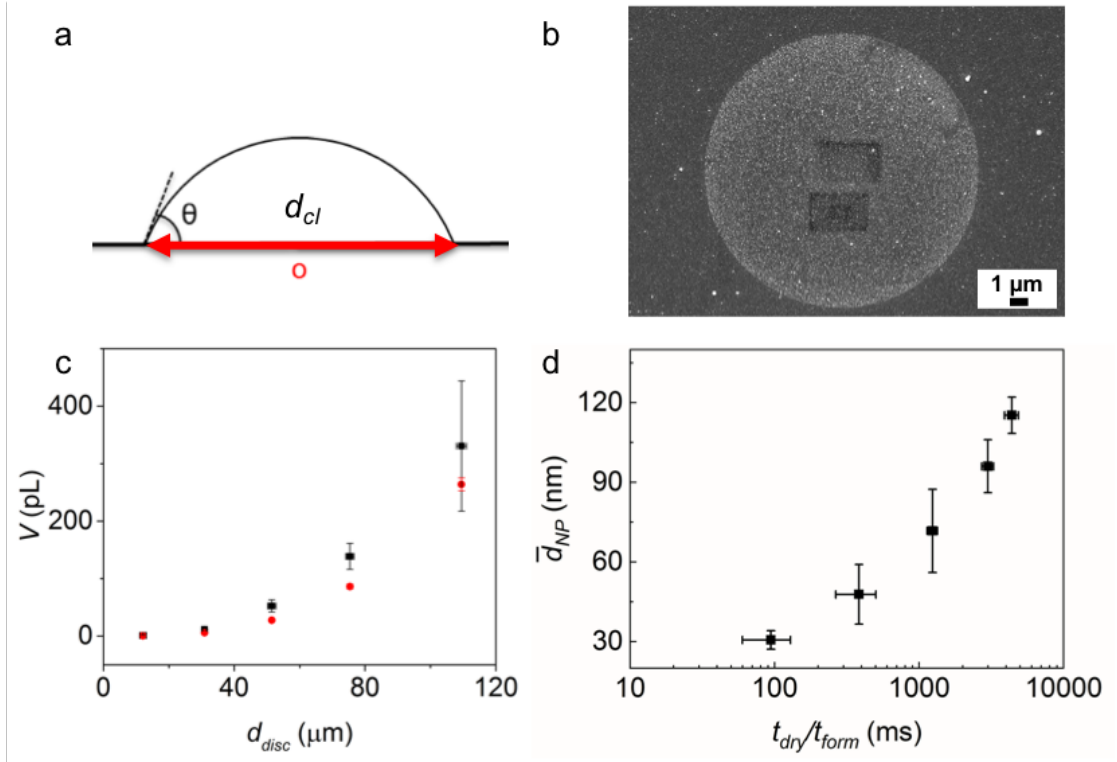


Figure 3.3 – Influence of the drying time of drops on the size of the spray-dried ACC nanoparticles. (a) Schematic illustration of a drop on the solid substrate. (b) SEM image of ACC particles formed within one drop. (c) Diameter of the disc (d_{disc}) as a function of V of the initial drop, which are calculated using two methods: contact line (●) and mass conservation (■). (d) Average diameter of the spray-dried ACC nanoparticles (\bar{d}_{NP}) as a function of the drying time of drops (t_{dry}), namely the formation time (t_{form}) of particles.

$$V = \frac{\pi d_{cl}^3 \left(\frac{1}{\sin\theta} - \frac{1}{\tan\theta} \right) \left(3 + \left(\frac{1}{\sin\theta} - \frac{1}{\tan\theta} \right)^2 \right)}{48} = \pi d_{cl}^3 \left(\frac{1}{16} \tan\frac{\theta}{2} + \frac{1}{48} \tan^2\frac{\theta}{2} \right) \quad (3.1)$$

Because the drops produced with the microfluidic spray dryer are small and dry quickly, it is very difficult to measure d_{cl} directly. However, some of the nanoparticles formed in one drop are pulled towards its edge through the coffee ring effect,[243] as shown in Figure 3.3b. Hence, we approximate the diameters of the drop contact lines to be the same as those of the discs that form after drops are dried and quantify them from SEM images. By substituting the θ and d_{disc} , we obtain the values of V , as summarized with the red circles in Figure 3.3c. To validate our results, we also use a mass conservation method to estimate the drop volumes. We can estimate the

Influence of the Formation Time on the Degree of Hydration and Stability of ACC

number (N_{NP}) and diameter (d_{NP}) of ACC particles that are produced in one drop from the SEM images. With this information and knowing the initial solute concentration of Ca^{2+} ($c_{\text{Ca}^{2+}}$) in the injected solution, we can estimate the volume of the drop using Equation 3.2

$$V = \frac{\rho_{ACC} \cdot \sum_1^{N_{NP}} \left(\frac{1}{6} \pi d_{NP}^3 \right)}{M_{ACC} \cdot c_{\text{Ca}^{2+}}} \quad (3.2)$$

Here ρ_{ACC} is the density of ACC and M_{ACC} its molar mass. The results obtained from this mass conservation method are summarized with the black squares in Figure 3.3c. The volumes of drops obtained from these two methods are in good agreement, indicating that our methods to calculate of the sizes of drops are robust.

To estimate the evaporation rates of drops, we assume that the vapor concentration field around the surface of drops is quasi-steady, the contact line is pinned, and the temperature variation is neglected.[242] In this case, the mass rate of water evaporation from a drop deposited on a solid substrate ($\frac{dm(t)}{dt}$) can be calculated using Equation 3.3,

$$\frac{dm(t)}{dt} = -\rho_{H_2O} \frac{dV(t)}{dt} = \pi r_{cl}(t) D_v (1 - RH) c_v (0.27\theta^2 + 1.3) \quad (3.3)$$

Here ρ_{H_2O} is the density of water, $V(t)$ the volume of the drop at time t , $r_{cl}(t)$ the radius of its contact line, D_v the diffusion coefficient of water vapor, c_v the concentration of saturated vapor around the drop surface, and RH the relative humidity. By combining Equations 3.1 and 3.3, we obtain,

$$r_{cl}(t)^2 = r_{cl}(0)^2 - \frac{2D_v(1 - RH)c_v(0.27\theta^2 + 1.3)}{\rho_{H_2O}(\frac{3}{2}\tan\frac{\theta}{2} + \frac{1}{2}\tan^2\frac{\theta}{2})} t \quad (3.4)$$

When the drop is completely dry, $r_{cl}(t)$ should be zero and hence the drying time is,

$$t_{dry} = \rho_{H_2O} \frac{\frac{3}{2}\tan\frac{\theta}{2} + \frac{1}{2}\tan^2\frac{\theta}{2}}{2D_v(1 - RH)c_v(0.27\theta^2 + 1.3)} r_{cl}(0)^2 \quad (3.5)$$

Here $r_{cl}(0) = d_{disc}/2$, which is measured from SEM images. We approximate D_v to be $27.9 \text{ mm}^2 \cdot \text{s}^{-1}$ and c_v to be $1.7 \times 10^{-8} \text{ g} \cdot \text{mm}^{-3}$. [242] RH is 50% as measured with a

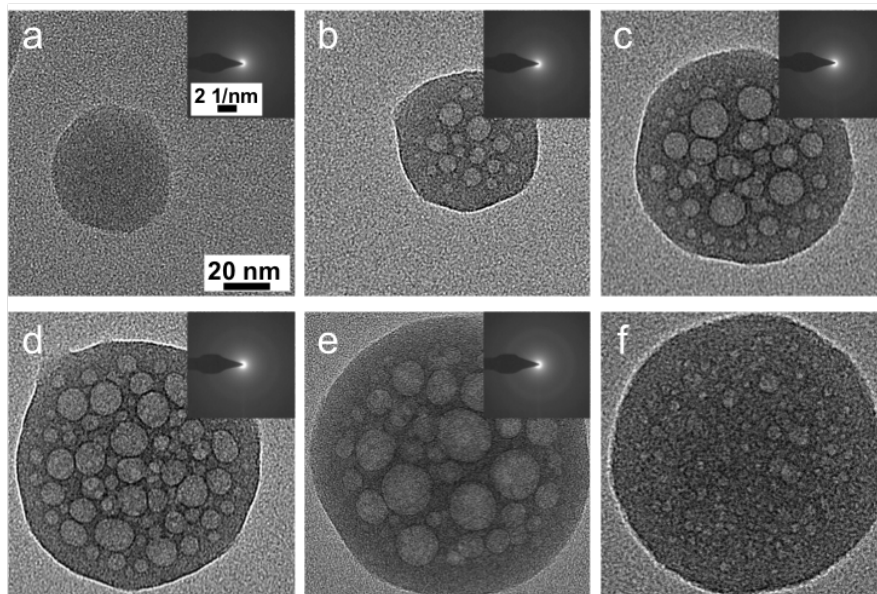


Figure 3.4 – Influence of the size of ACC nanoparticles on their morphology. TEM images of ACC particles with a diameter of (a) 47 nm, (b) 65 nm, (c) 97 nm, (d) 112 nm, and (e) 130 nm with the SAED patterns as insets. (f) TEM image of a 130 nm diameter ACC particle that has been stored in a desiccator under a reduced pressure for 2 months.

hygrometer and θ is 77.8° as measured with a drop shape analyzer. In this case, drops with a diameter of $10\ \mu\text{m}$ dry within 100 ms, whereas $100\ \mu\text{m}$ diameter drops dry within 10 s.

If we vary the diameters of drops from $10\ \mu\text{m}$ to $100\ \mu\text{m}$, the drying time of drops and hence the formation time of ACC particles increases from 100 ms to 10 s. As a result, we observe that \bar{d}_{NP} of the resulting particles increases from 30 nm to 120 nm, as shown in Figure 3.3d. These results are well in agreement with reports on particles produced in bulk solution whose size increases with increasing formation time.[29, 31, 43] Using this correlation, we can deduce the formation time of particles by quantifying their size. This correlation allows studying early stages of the formation of ACC particles with a high temporal resolution without the need for any organic solvent.

To monitor the evolution of the morphology of ACC particles during the formation, we visualize the particles that possess different diameters using TEM. To minimize the risk for electron beam-induced artifacts, which are uncontrollably introduced into particles during their visualization, we image them with a relatively low, well-

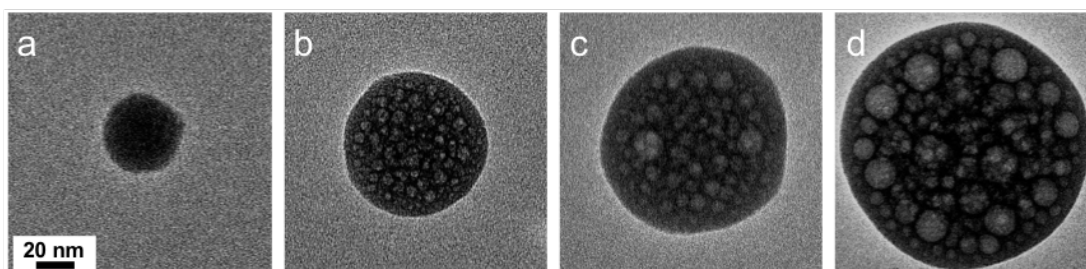


Figure 3.5 – Influence of the size on the morphology of ACC nanoparticles that are produced by co-spray-drying an aqueous solution containing CaCl_2 with one containing Na_2CO_3 . (a-d) TEM images of ACC particles with a diameter of (a) 42 nm, (b) 77 nm, (c) 105 nm and, and (d) 130 nm.

defined electron dose of $60 \text{ e} \cdot \text{\AA}^{-2} \cdot \text{s}^{-1}$. Spray-dried CaCO_3 particles do not display any diffraction spots in their SAED patterns, as exemplified in the insets of Figures 3.4a-e. Instead, the SAED pattern consists of diffuse rings, further confirming the amorphous structure of the particles, well in agreement with our FTIR, XAS, and XRD results. However, particles with varying sizes show distinctly different morphologies: while particles with diameters below 50 nm have a uniform contrast, larger particles contain electron-light domains that are embedded in an electron-dense matrix. The number and average size of the electron-light domains increase with increasing particle size, as shown in Figures 3.4a-e. To exclude that this morphology is related to the composition of the reactants used to produce ACC particles, we co-spray dry an aqueous solution containing CaCl_2 with one containing Na_2CO_3 . The resulting ACC particles display a very similar morphology, as shown in Figures 3.5a-d, indicating that this morphology is inherent to our ACC particles.

Transmission electron microscopy images of ACC particles that display two distinctly different phases[40, 77, 117] as well as those with a homogeneous contrast[31, 244] have been reported. The origin of these differences in morphology is not yet fully understood. A possible reason for these abrupt changes in contrast within a single particle is radiolysis, where the electron beam ionizes water contained in ACC particles and converts it into gases.[245] The resulting gases are trapped within the particles and form pores that correspond to the electron-light regions.[40, 244] In this case, the electron beam-induced phase separation could be taken as a qualitative measure for the degree of hydration of ACC particles. Our results would then suggest that the propensity of particles to undergo electron beam-induced phase separation increases with increasing degree of hydration. To test this suggestion, we store spray-dried ACC particles in a desiccator at reduced pressure for two months to remove parts of the

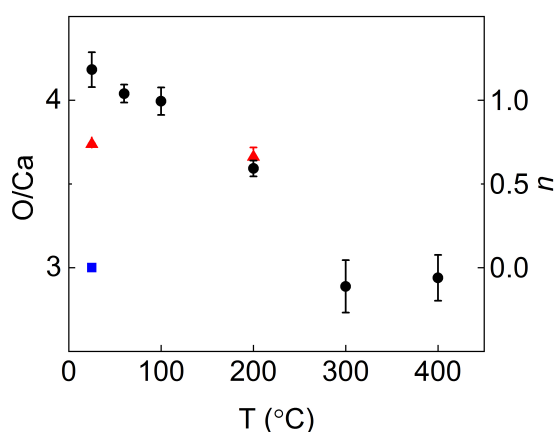


Figure 3.6 – Atomic ratio of O to Ca and the degree of hydration of ACC nanoparticles with an average diameter of 130 nm (●) and those with an average diameter of 30 nm (▲) as a function of the annealing temperature, as well as that of a calcite reference sample (■), quantified with XPS measurements.

water contained in as-prepared ACC particles.[86] Indeed, these dried particles display much smaller electron-light regions than as-prepared particles with similar diameters, as a comparison between Figures 3.4e and 3.4f reveals. These results suggest that the observed phase separation is related to the degree of hydration of the particles. Hence, we conclude that small particles, whose formation is quenched at earlier stages, are less hydrated than their larger counterparts.

Our TEM results indicate that the degree of hydration increases with increasing formation time and hence, with increasing particle size. To test this suggestion, we quantify the amount of water contained in spray-dried ACC particles using XPS. X-ray photoelectron spectroscopy only probes the surface of particles. However, because the TEM images do not provide any evidence for core-shell structures of our particles, as shown in Figure 3.4, we approximate the surface composition of the particles to be equal to that of their cores. Using this approximation, we quantify the amount of water contained in particles with an average diameter of 130 nm, whose formation time is 10 s. Similarly, we quantify the amount of water contained in particles with an average diameter of 30 nm, whose formation time is 100 ms. The n of 30 nm diameter particles is 30% lower than that of larger particles, as indicated by the lower atomic ratio of O to Ca (O/Ca), shown in Figure 3.6. This result indicates that n of spray-dried ACC particles increases with increasing formation time and supports our TEM results. The correlation between the formation time and n of ACC particles might be a contributing reason for the wide range of the values of n from 0.4 to 1.58 reported

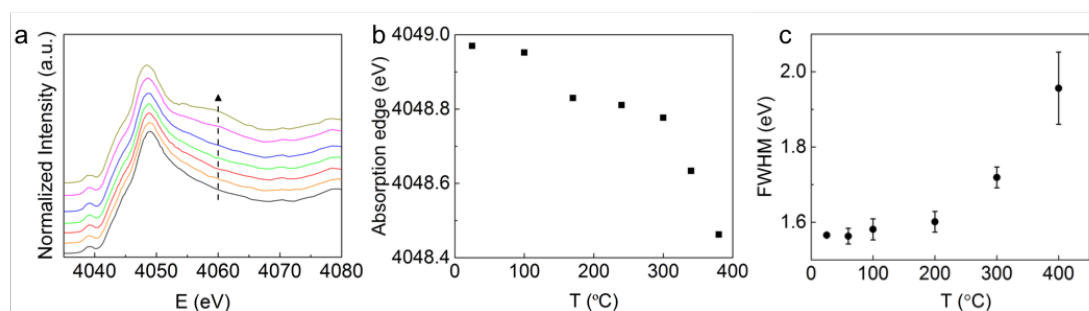


Figure 3.7 – Influence of the degree of hydration of ACC particles on their structures. (a) Ca K-edge XANES spectra and (b) the corresponding positions of the absorption edge of ACC particles with an average diameter of 130 nm that are heated *in situ* to different temperatures. Following the direction of the arrow, the temperature is increased from room temperature (RT) to 100, 170, 240, 300, 340, and 380 °C. (c) Full width half-maximum of the Ca 2p_{3/2} peaks of ACC particles with an average diameter of 130 nm as a function of the annealing temperature, as determined with XPS.

for particles produced under similar conditions.[40, 76, 87, 92, 94]

3.2.3 Mobility of water contained in ACC particles

Our results suggest that larger ACC particles possess a higher degree of hydration. This water is well known to influence the stability of ACC particles but the extent of its effect depends on its interaction with CaCO₃. [103, 114, 118] Water contained in ACC can weakly interact with CO₃²⁻ and therefore is usually called mobile water. [76, 96, 109, 119] Water can also strongly interact with Ca²⁺ ions such that it has a restricted mobility and is considered to be rigid. [76, 96, 109, 119] This strongly bound water is an integral part of the structure of ACC, such that its loss is accompanied by a re-arrangement of Ca²⁺ and CO₃²⁻. [108, 114] Because of the stronger interatomic interactions, rigid water evaporates at much higher temperatures than mobile water does. [77, 108] To test if spray-dried 130 nm diameter ACC particles contain any rigid water, we acquire XANES spectra as a function of the temperature that is varied *in situ*. When the temperature is increased above 170 °C, a shoulder around 4060 eV appears and the position of the absorption edge is shifted towards lower values, as summarized in Figures 3.7a-b. These results hint at a re-arrangement of the ions that occurs upon removal of rigid water. In line with these observations, the FWHM of the Ca 2p_{3/2} peak measured with XPS increases significantly if the particles are annealed at temperatures above 200°C, as shown in Figure 3.7c. These results indicate that ion re-arrangement occurs both, in the core and at the surface of the particles.

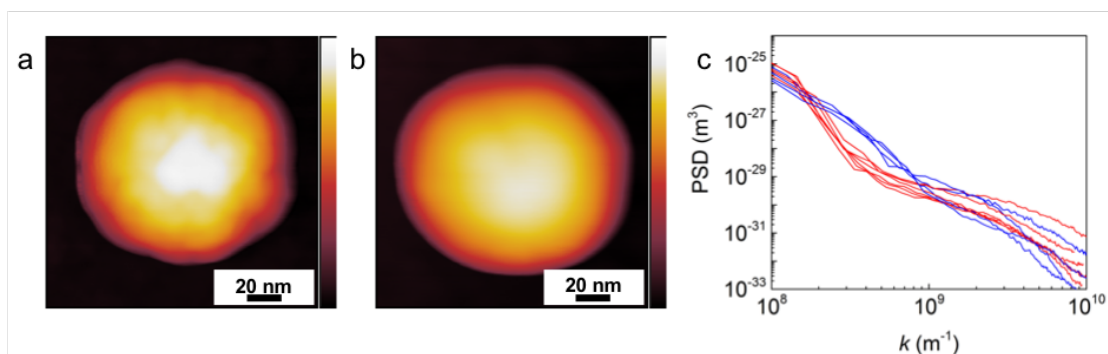


Figure 3.8 – Surface roughness of ACC particles. (a,b) Height-contrast AFM images of ACC particles (a) freshly produced and (b) after having been annealed at 200 °C for 3 h. The color scale ranges from 0 to 60 nm. (c) Power spectral density plots of the freshly produced particles (blue) and those annealed at 200 °C for 3 h (red) calculated from the AFM images. The measurement has been repeated on different particles, each represented by one curve in the figure.

If a large fraction of ions located in proximity to the surface re-arranges, we expect the surface roughness of these particles to change. To test this expectation, we image the surface of these particles with AFM before and after they have been annealed at 200 °C for 3 h, as shown in Figures 3.8a-b. Indeed, a comparison of the PSD function analysis performed on the AFM images reveals that annealed particles have a considerably lower PSD than as-prepared ones in a spatial frequency (k) ranging from 2×10^8 to 1×10^9 m⁻¹ that corresponds to features with a size of 6–30 nm in real space, as shown in Figure 3.8c. These results indicate that annealed particles possess a significantly smoother surface than as-produced counterparts and hence, that the removal of rigid water occurred around 200 °C is accompanied by a re-arrangement of the ions contained in ACC. However, even though ions re-arranged, we do not observe any sign of crystallinity in these particles, suggesting that a significant amount of rigid water is released before particles start to crystallize.

Our results suggest that spray-dried particles encompass a significant amount of rigid water. To quantify the amount of rigid water, we measure the O/Ca ratio of the particles as a function of the annealing temperature using XPS. Particles with diameters around 130 nm contain approximately 1.2 H₂O molecules per CaCO₃. Approximately 50% of this water is removed below 200 °C, whereas the remaining water is removed between 200 °C and 300 °C, as summarized in Figure 3.6. These results suggest that about 50% of the water contained in 130 nm diameter particles is rigid water, corresponding to a concentration of 0.6 molecules of structural H₂O per mole of CaCO₃. Remarkably,

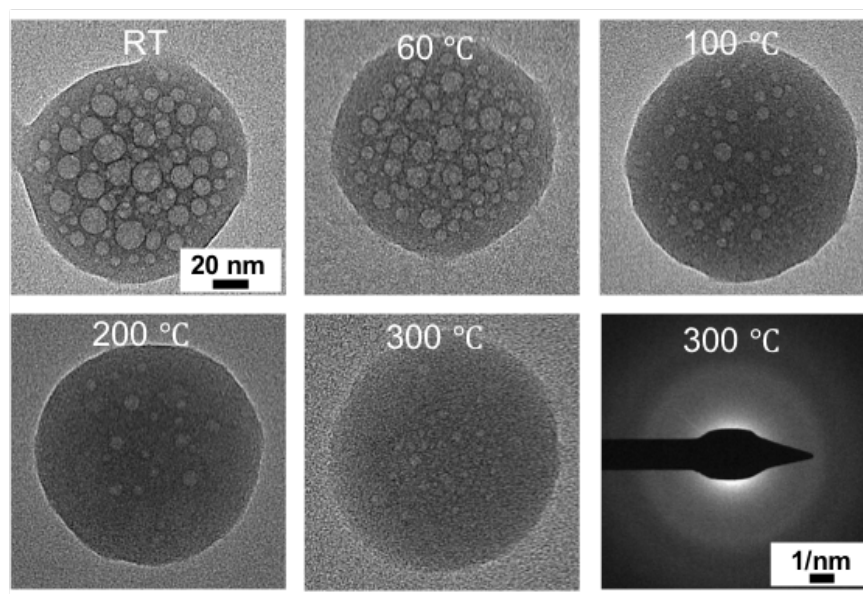


Figure 3.9 – Influence of the degree of hydration of ACC particles on their morphology. TEM images and SAED pattern of 130 nm diameter ACC particles that have been annealed at different temperatures for 3 h.

this concentration is very similar to the total amount of water contained in 30 nm diameter ACC particles, suggesting that the majority of water contained in these small particles is rigid. To test this suggestion, we quantify the degree of hydration of 30 nm diameter particles that have been annealed at 200 °C. Indeed, the degree of hydration of 30 nm diameter particles does not measurably change upon annealing at 200 °C for 3 h, as shown in Figure 3.6. These results indicate that the vast majority of water contained in smaller particles is rigid.

The very low concentration of mobile water contained in 30 nm diameter particles likely renders them more resistant against radiolysis, as shown in Figure 3.4. To test if it is indeed the amount of mobile water contained in ACC particles that determines their susceptibility towards radiolysis and not their size, we visualize larger particles that have been annealed at different temperatures using TEM. While particles with a diameter of 130 nm that have been annealed at 100 °C or below undergo considerable electron beam-induced phase separations, particles annealed at 200 °C or above only contain very few electron-light domains, as shown in Figure 3.9. These results confirm that the presence of mobile water renders particles prone to undergo electron beam-induced phase separation. Moreover, these results suggest that the observed increase in the degree of hydration with increasing size of the ACC particles is mainly attributed

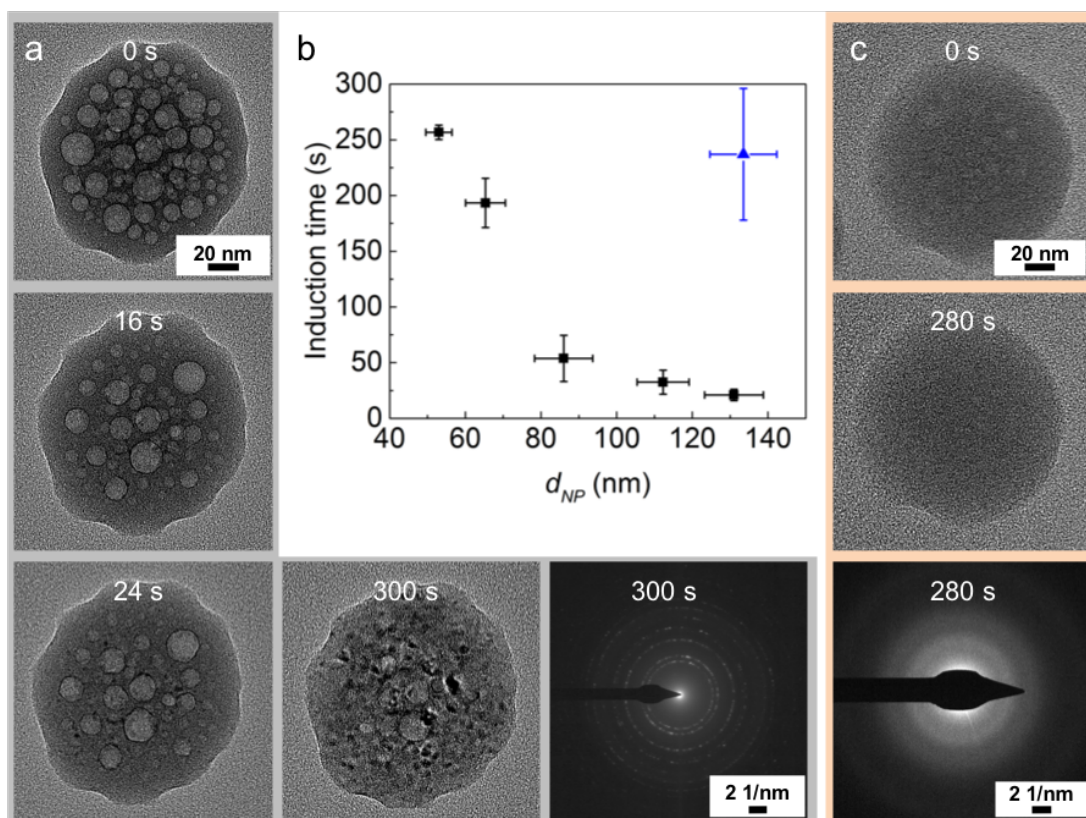


Figure 3.10 – Kinetic stability of ACC particles against the electron beam-induced decomposition. (a) Time-lapse TEM images and SAED pattern of a 130 nm diameter ACC particle exposed to a focused electron beam with a dose of $400 \text{ e} \cdot \text{\AA}^{-2} \cdot \text{s}^{-1}$. (b) Influence of d_{NP} of as-prepared ACC particles (■) and those dehydrated in a vacuum (▲), on the exposure time required to induce the formation of CaO crystals. (c) Time-lapse TEM images and SAED pattern of a 130 nm diameter ACC particle that has been annealed at 300 °C for 3 h, when it is exposed to a focused electron beam with a dose of $400 \text{ e} \cdot \text{\AA}^{-2} \cdot \text{s}^{-1}$.

to the increasing amount of mobile water.

3.2.4 Influence of mobile water on the stability of ACC particles

The electron beam is known to decompose CaCO_3 into crystalline CaO and CO_2 , if its intensity is sufficiently high.[246] If ACC particles are imaged with a low dose of electrons, $60 \text{ e} \cdot \text{\AA}^{-2} \cdot \text{s}^{-1}$, we do not observe any formation of CaO. However, we expect particles that contain a high concentration of mobile water and hence that undergo radiolysis even if exposed to a low electron dose, to be prone to an electron beam-induced decomposition. To test our expectation, we expose particles to a

Influence of the Formation Time on the Degree of Hydration and Stability of ACC

high electron dose of approximately $400 \text{ e} \cdot \text{\AA}^{-2} \cdot \text{s}^{-1}$ and observe structural changes *in situ*. In 130 nm diameter particles that contain significant amounts of mobile water, the electron-light domains rapidly grow and coalesce before small crystals start to form at the interface of the domains, as illustrated in time-lapse TEM micrographs of Figure 3.10a. The crystals that form at the interface and grow into the electron-dense phase are composed of CaO, as indicated by the diffraction pattern in Figure 3.10a. The illumination time required to induce this decomposition increases with decreasing particle size, as summarized in Figure 3.10b. This result suggests that the time required to induce the decomposition of ACC into CaO scales inversely with the amount of mobile water contained in ACC. To confirm this suggestion, we dehydrate the ACC particles in vacuum or by annealing them at 300 °C and subsequently expose them to a focused electron beam. The dehydrated particles are much more stable than as-produced counterparts with a similar average diameter, as shown in time-lapse TEM micrographs in Figure 3.10c and summarized in Figure 3.10b. These results confirm that the stability of ACC particles against electron beam-induced decomposition increases with decreasing amount of mobile water.

To study the influence of the amount of mobile water on the propensity of spray-dried particles to crystallize, we anneal particles with an average diameter of 45 nm and those with an average diameter of 130 nm in a furnace and quantify the temperature where crystallization occurs in the absence of any bulk water using TEM. ACC particles with a diameter of 130 nm start to crystallize at 330 °C whereas those with a diameter of 45 nm that contain only a very small fraction of mobile water start to crystallize at a significantly higher temperature, 370 °C, as shown in the TEM images and SAED patterns in Figure 3.11. These results indicate that the temperature where ACC particles start to crystallize decreases with increasing amount of mobile water. Because the amount of mobile water in our ACC particles increases with increasing size, the temperature where particles start to crystallize decreases with increasing size, well in agreement with previous reports on ACC particles produced in bulk.[81] Our results suggest that this decrease in the crystallization temperature measured for particles whose diameter increases from 30 – 130 nm is related to their change in composition, namely the increased amount of mobile water, rather than being purely a size effect.

The concentration of mobile water contained in ACC particles determines their stability against temperature-induced crystallization. Interestingly, the concentration of mobile water contained in ACC particles also influences the size of the resulting crys-

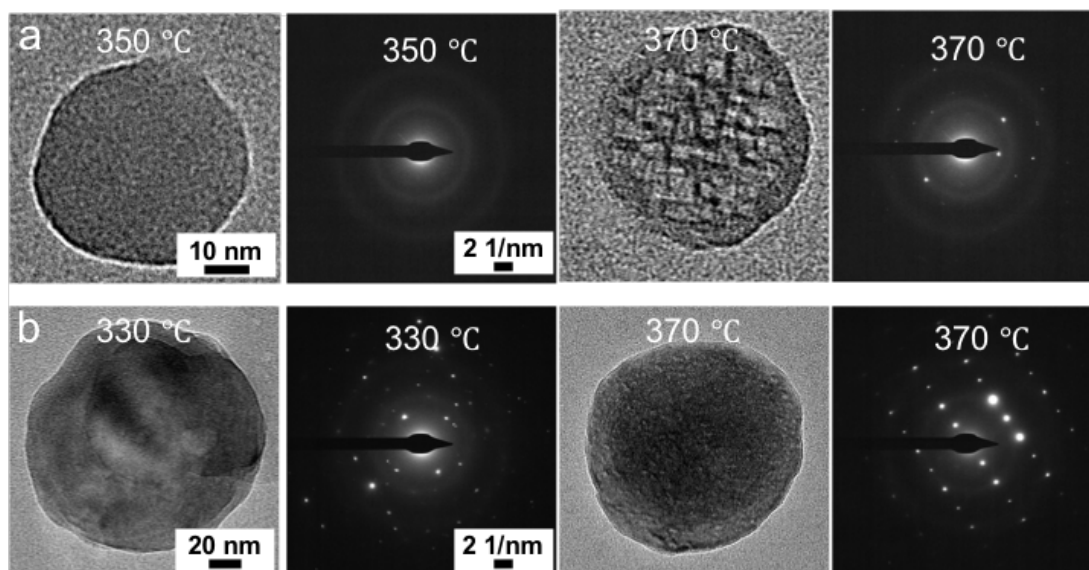


Figure 3.11 – Kinetic stability of ACC particles against the temperature-induced crystallization. (a, b) TEM images and SAED patterns of (a) 45 nm and (b) 130 nm diameter ACC particles after having been annealed at different temperatures for 3 h.

tals: The size of grains formed in 45 nm diameter particles is much smaller than that of grains formed in 130 nm diameter particles, as shown in Figure 3.11. Indeed, 130 nm particles often transform into a single crystal whereas 45 nm diameter particles are transformed into polycrystals. We attribute this difference to the mobility of the ions: Larger particles contain a higher amount of mobile water that likely enhances the mobility of Ca^{2+} and CO_3^{2-} . The higher mobility allows nuclei to grow relatively quickly and consume the ions before many more nuclei can form. By contrast, the mobility of Ca^{2+} and CO_3^{2-} contained in smaller particles, which contain less mobile water, is likely lower such that the crystals grow much slower and many more nuclei can form before all the ions contained in ACC are consumed.

3.2.5 Influence of poly(acrylic acid) on the stability of ACC particles

The formation of ACC particles[143, 145] and their stability against crystallization[122, 138, 176, 196] strongly depend on the additives contained in them. To test if additives influence the amount of mobile water contained in ACC particles, we produce ACC particles that are functionalized with PAA-100K through co-spray-drying; PAA is known to delay the crystallization of ACC[61, 71, 138, 143, 145] without measurably altering its degree of hydration.[138] The spray-dried PAA-functionalized particles are

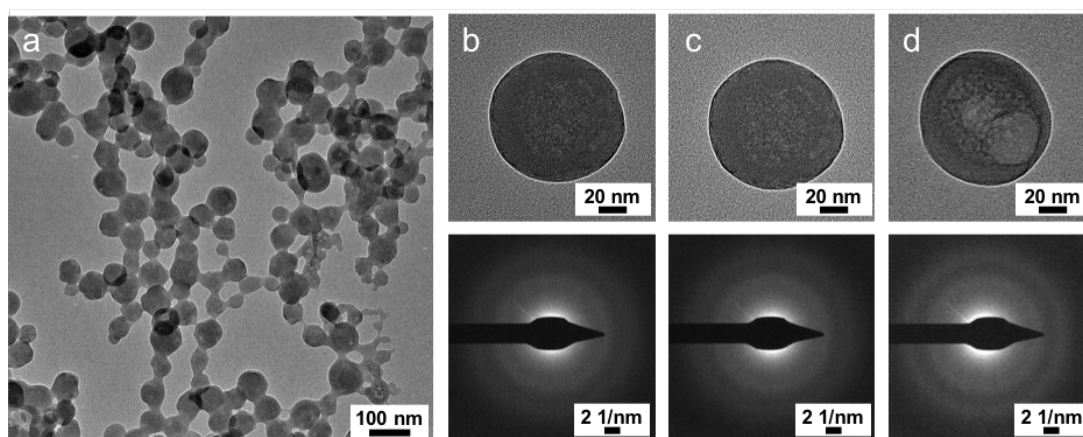


Figure 3.12 – PAA-functionalized ACC particles. (a) Overview TEM image of PAA-functionalized ACC particles. (b, c) TEM images and corresponding SAED patterns of a 100 nm diameter PAA-functionalized ACC particle (b) as-produced and (c) after having been exposed to a focused electron beam with a dose of $400 \text{ e} \cdot \text{\AA}^{-2} \cdot \text{s}^{-1}$ for 280 s. (d) TEM image and SAED pattern of a 100 nm diameter PAA-functionalized ACC particle after having been annealed at 370°C for 3 h.

significantly smaller than additive-free counterparts and individual particles are interconnected by PAA, as shown in Figure 3.12a. However, the most striking difference between PAA-functionalized and additive-free particles is their stability against electron beam-induced phase separation: PAA-functionalized particles with diameters up to 100 nm do not undergo any electron beam-induced phase separation, in stark contrast to additive-free counterparts with similar sizes, as shown in Figure 3.12b. This result indicates that the water contained in PAA-functionalized particles is less mobile, likely because it strongly interacts with PAA.[247] This behavior is similar to that observed for other additives, such as PSS,[247] Mg^{2+} , [157] and PO_4^{3-} . [128] As a result of the lower mobility of water contained in ACC, these particles are more stable against electron beam-induced decomposition: PAA-functionalized particles with a diameter of 100 nm do not undergo any decomposition even if exposed to a focused electron beam for 280 s, which is six times longer than the time required to induce decomposition of additive-free particles of a similar size, as shown in Figure 3.12c. Similarly, PAA-functionalized particles are kinetically more stable against temperature-induced crystallization: These particles do not crystallize even if exposed to 370°C for 3 h although they undergo a noticeable change in morphology, as shown in Figure 3.12d, well in agreement with results reported for particles produced in bulk.[138] We assign the higher stability of PAA-functionalized particles again to the lower mobility of water that delays the crystallization.[77]

3.3 Discussion

Molecular dynamics simulations predict water to play a key role in the formation of ACC particles.[80, 83] Our results indicate that the amount of mobile water contained in ACC particles increases as they grow from 30 nm to 130 nm. To test if water influences the formation energy of particles, we relate our experimental results to those obtained from molecular dynamics simulations. These studies indicate that the enthalpy of ACC particles decreases with increasing degree of hydration,[80, 114, 118] in good agreement with calorimetric measurements.[28, 86] These results suggest that the enthalpy of our particles decreases as they grow. Simulations indicate that the contribution of the entropy penalty, associated with the incorporation of water into ACC, to the free energy is much smaller than that of the enthalpy.[80, 118] We therefore neglect the entropy for our qualitative consideration of the free energy. In this case, as a result of the decreasing enthalpy, the free energy decreases as the particles grow indicating that, due to the increase in the degree of hydration, the ACC particle growth is thermodynamically favorable, as schematically illustrated in Figure 3.13a.

The most common CaCO_3 crystals that exist under ambient conditions, namely calcite, aragonite, and vaterite, are anhydrous, such that water contained in ACC must be expelled before these crystals can form.[29, 40, 77, 248] If put in bulk solutions, ACC particles dissolve and new, water-free crystals reprecipitate from a supersaturated solution.[54] As the ACC particles are surrounded by bulk water, we expect the degree of hydration to not be the most important factor determining the kinetics of dissolution of ACC particles. Instead, the dissolution kinetics is strongly influenced by the surface-to-volume ratio of these particles and hence, by their size. As a result of the decrease in surface-to-volume ratio with increasing ACC particle size, the rate of crystallization in bulk solutions decreases with increasing particle size, as was nicely demonstrated on ACC particles produced in bulk, as shown schematically in Figure 3.13b.[81] By contrast, if crystallized in the absence of bulk water at high temperatures,[121] ACC particles typically crystallize through a solid-state transformation. In this case, ACC must dehydrate before crystals can start to form through re-arrangements of Ca^{2+} and CO_3^{2-} ions.[77, 86, 114] Our temperature-dependent TEM results indicate that ACC particles dehydrate before they crystallize, suggesting that they crystallize through a solid-state transformation[16–18, 87, 121] despite the fact that they initially contain a high concentration of water. Moreover, our results indicate that the kinetics of this crystallization is influenced by the amount of water contained in ACC particles: The more mobile water is present in ACC particles with

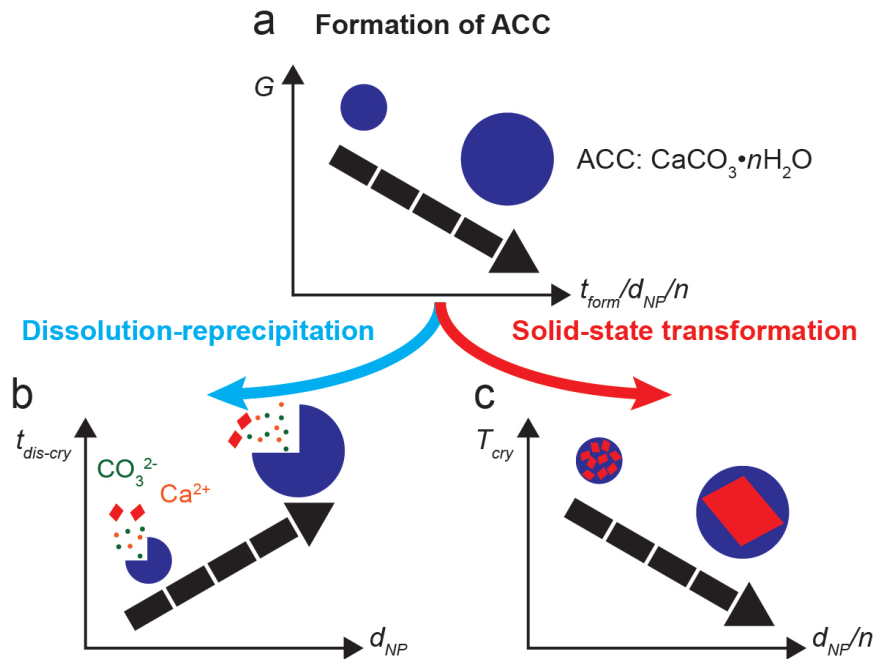


Figure 3.13 – Schematic illustration of the formation of ACC particles and their transformation into crystals. (a) The free energy (G) of ACC particles decreases with increasing t_{form} , d_{NP} , and n . ACC particles can transform into crystals through a (b) dissolution-reprecipitation pathway or (c) solid-state transformation. If crystallized through dissolution-reprecipitation, the time required for crystals to form ($t_{dis-cry}$) increases with increasing particle size. By contrast, if crystallized through a temperature-induced solid-state transformation, the temperature where crystals start to form within a given amount of time (T_{cry}) decreases with increasing particle size and hence with increasing amount of mobile water contained in ACC particles.

sizes exceeding 30 nm, the higher is the mobility of the Ca^{2+} and CO_3^{2-} ions and the faster do they crystallize. Hence, in the absence of bulk water, the temperature where ACC particles start to crystallize within a given amount of time decreases with increasing size because the amount of mobile water contained in them increases, as schematically illustrated in Figure 3.13c. These results indicate that the kinetics of the crystallization is influenced by the amount of mobile water contained in ACC particles with sizes varying between 30 and 130 nm. Hence, while the growth of these ACC particles is thermodynamically driven, their crystallization in the absence of bulk water is kinetically controlled.

3.4 Conclusion

The microfluidic spray dryer quenches reactions through rapid drying of the aqueous solution without the need for organic solvents. Thereby, it enables studying early stages of the formation of ACC particles with a high temporal resolution. We demonstrate that the amount of mobile water contained in ACC particles increases with increasing formation time and hence, with increasing particle size. The amount of mobile water contained in these particles influences their kinetic stability against temperature-induced solid-state transformation and electron beam-induced decomposition. While we investigated the role of water in the formation and transformation of CaCO_3 , our findings are not limited to this material but most likely also apply to the formation of many other materials that form via transient precursors, such as calcium phosphate, calcium oxalate, and calcium sulfate. These findings might offer new insights to better understand the role of water in the biomineralization process occurring in nature. They might also open up new possibilities to control the crystallization of CaCO_3 through tuning the degree of hydration of ACC, thereby facilitating the fabrication of biomimetic CaCO_3 -based materials whose structures and properties more closely resemble those of natural biomaterials.

4 Influence of the Additives on the Humidity- and Pressure- Induced Crystallization of ACC

This chapter is adapted from the paper entitled “Additives: Their Influence On the Humidity- and Pressure- Induced Crystallization of Amorphous CaCO_3 ,” authored by H. Du, C. Courrégelongue, J. Xto, A. Böhlen, M. Steinacher, C. Borca, T. Huthwelker, and E. Amstad, and submitted in Oct. 2019.[226] H. Du designed all the experiments. H. Du and C. Courrégelongue performed all the experiments. A. Böhlen and M. Steinacher contributed to the material synthesis and characterizations. J. Xto, C. Borca and T. Huthwelker helped with the *in situ* FTIR measurements. H. Du, C. Courrégelongue and E. Amstad analyzed all the data. H. Du and E. Amstad wrote the paper.

In this chapter, we present a systematic study of the influence of additives on the crystallization of ACC when exposed to humid environments or elevated pressures. We find that the humidity-induced crystallization of ACC follows a distinctly different pathway than that induced by pressure. As a result, the influence of additives on the crystallization kinetics of ACC, and hence, the size, morphology, structure, and orientation of the resulting CaCO_3 crystals differs considerably.

Contents

4.1	Introduction	76
4.2	Results	78
4.2.1	Synthesis and characterization of ACC particles	78
4.2.2	Humidity-induced crystallization kinetics	80
4.2.3	Crystals obtained from the humidity-induced crystallization .	88
4.2.4	Pressure-induced crystallization kinetics	90
4.2.5	Crystals obtained from the pressure-induced crystallization .	97
4.3	Discussion	98
4.3.1	Kinetic stability of ACC	98
4.3.2	Size, morphology, orientation and structure of CaCO ₃ crystals	100
4.4	Conclusion	102

4.1 Introduction

Amorphous CaCO₃ is metastable and hence crystallizes with time.[1, 40, 117, 123] This crystallization can be accelerated if particles are immersed in bulk solutions, where the crystallization occurs through a dissolution-reprecipitation pathway.[1, 29, 30, 40, 52–54, 81, 121, 122] While this crystallization pathway is often used, it offers very limited control over the formation of CaCO₃ and hence over the properties of resulting crystals. Crystallization of ACC can also be accelerated if particles are exposed to elevated temperatures,[28, 81, 86, 87, 121, 122, 127, 128] where ACC undergoes a solid-state transformation that includes a complete dehydration of ACC and a subsequent formation of CaCO₃ crystals.[28, 77, 81, 121, 122, 127, 225] These two crystallization pathways possess distinctly different activation energies and hence crystallization kinetics[1, 40, 77, 114, 118] that translate into differences in the size, morphology, and structure of the resulting CaCO₃ crystals.[1, 81] The crystallization of ACC in solution or at elevated temperatures can be influenced by certain low molecular weight additives such as Mg²⁺, [86, 157, 159, 161] PO₄³⁻, [86, 128] CIT, [145, 176] Gly, [177] and Asp, [177] as well as high-molecular weight counterparts such as PAA, [53, 138, 143, 225] PSS, [43, 122, 138, 145] PAsp, [44, 106] poly(allylamine hydro chloride), [192, 249] and acidic proteins.[74, 250, 251] The effects of these additives on the crystallization of

ACC depend on their molecular weight,[122, 148, 252] functional groups,[86, 122, 138, 143, 145, 249] and quantity contained in ACC.[138, 157, 159, 161, 176, 196] Interestingly, the influence of additives on the crystallization of ACC also depends on the processing conditions.[1, 122] This was nicely demonstrated for ACC functionalized with PSS, PAsp, or AOT; these additives increase the kinetic stability of ACC against crystallization if ACC is exposed to bulk solutions but decrease it if exposed to elevated temperatures.[122, 127]

The crystallization of ACC can also be induced if it is exposed to a humid environment[40, 86, 121, 123, 131, 132] or elevated pressures.[129, 130] Interestingly, it has been shown that the kinetic stability of ACC as well as the size, morphology, structure, and orientation of the resulting crystals are distinctly different from those formed if ACC is exposed to bulk solutions or elevated temperatures.[40, 86, 121, 123, 129–131] This finding might open up new possibilities to fabricate CaCO_3 -based materials with structures and hence properties that can be tuned over a much wider range.[129, 253] However, the effects of additives on the crystallization of ACC induced by exposing it to a humid environment or elevated pressures are poorly understood. While it has been shown that Mg^{2+} [86, 131] and PO_4^{3-} [86] can increase the kinetic stability of ACC against humidity-induced crystallization, the effects of other additives remain unknown. Moreover, a study on the influence of additives on the pressure-induced crystallization of ACC is missing. This incomplete understanding of the effects of additives on the humidity- and pressure- induced crystallization of ACC limits the range of structures and properties of CaCO_3 -based materials that can be accessed. To close this gap, a better understanding of the influence of additives on the humidity- and pressure- induced crystallization of ACC and how these parameters relate to the size, structure, and morphology of the resulting crystals is warranted.

In this chapter, we systematically study the influence of different additives on the crystallization of ACC when exposed to a humid environment or elevated pressures. We monitor the evolution of the structure and degree of hydration of ACC during its crystallization *in situ* and *ex situ* as well as relate these results to the size, morphology, structure, and orientation of the resulting crystals. We find that the humidity-induced ACC crystallization pathway is distinctly different from the pressure-induced counterpart. As a result of the different crystallization pathways, the influence of additives on the crystallization kinetics of ACC as well as the size, morphology, structure, and orientation of the resulting CaCO_3 crystals differs considerably. These new insights might offer new possibilities to design CaCO_3 -based materials whose structures and

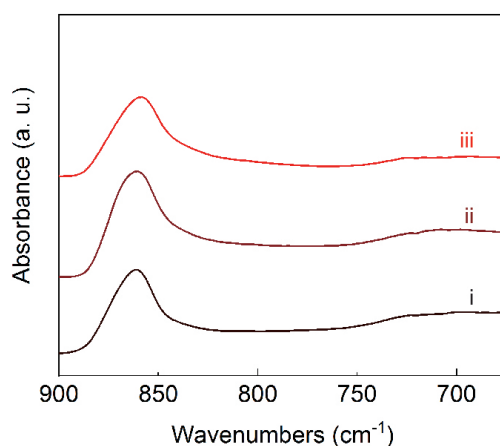


Figure 4.1 – Kinetic stability of CIT-functionalized ACC particles that are synthesized from an aqueous solution containing CIT and Ca^{2+} with a molar ratio of 1:10. (i) FTIR trace of as-synthesized CIT-functionalized ACC and those of particles after they have been (ii) exposed to a RH around 95% for 30 h or (iii) subjected to a pressure of 738 MPa for 30 h. The similar features in these FTIR traces indicates no crystallization occurs during the exposure.

properties can be tuned to more closely resemble natural counterparts.

4.2 Results

4.2.1 Synthesis and characterization of ACC particles

To study the influence of additives on the crystallization of ACC, we employ additives that are often used to control the crystallization in bulk solutions or at elevated temperatures, as summarized in Figure 2.2.[53, 86, 122, 138, 157, 176, 177, 192, 249] We keep the molar ratio of the low molecular weight additives or the repeat units for the polymeric additives to Ca^{2+} present in the initial solution constant at 1:10. However, if we produce CIT-functionalized ACC particles with this ratio, they do not crystallize within 30 h under the crystallization conditions used in this study, which is more than 10 times longer than it takes ACC particles functionalized with the other tested additives to crystallize, as shown in Figure 4.1. Therefore, we lower its concentration threefold. We characterize the synthesized particles using FTIR and powder XRD. The FTIR traces of all the synthesized particles display the characteristic features of ACC,[16, 90, 106, 225] including the presence of a ν_2 absorption peak around 860 cm^{-1} and the absence of a ν_4 absorption peak around 700 cm^{-1} , as shown in Figures 4.2a-c.

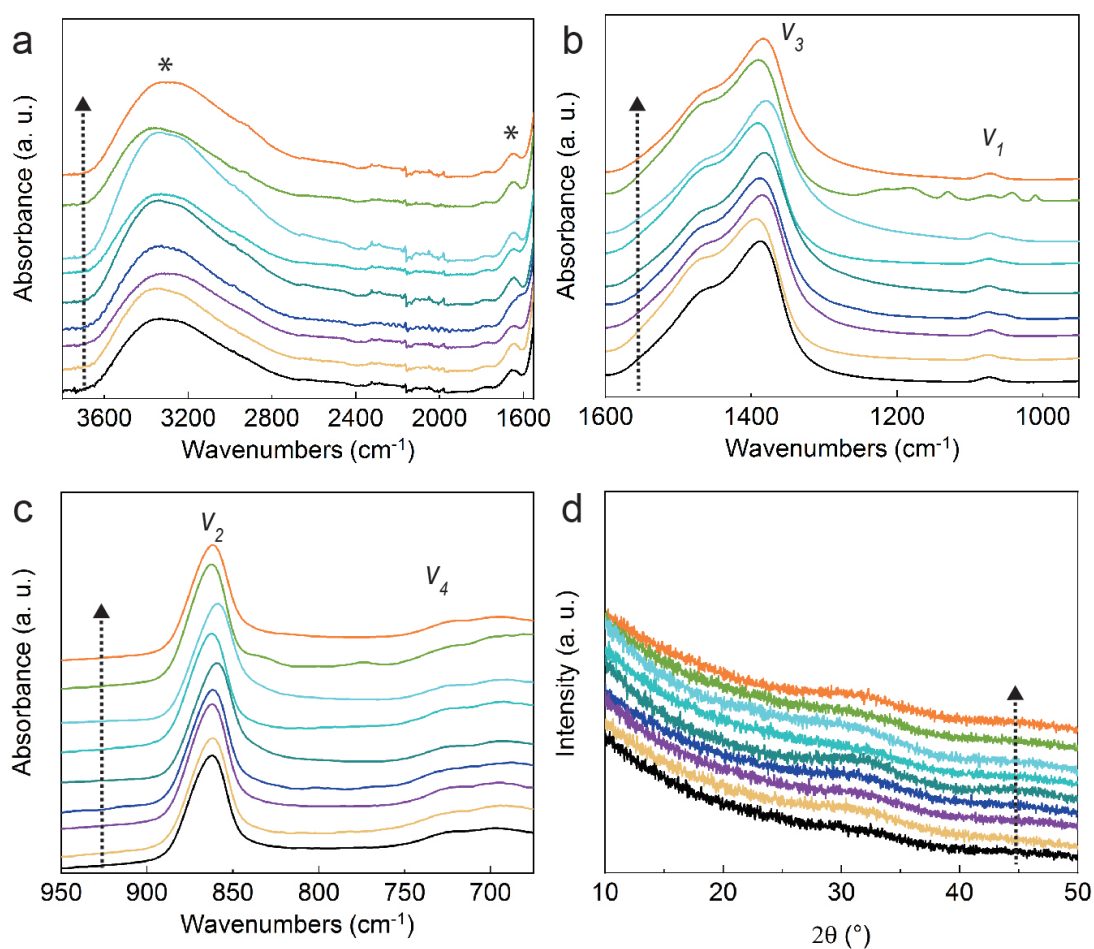


Figure 4.2 – Characterization of the structure of the synthesized ACC particles. (a-c) FTIR and (d) XRD traces of unfunctionalized ACC particles (bottom) and those functionalized with Mg, Gly, CIT, AA, PAA-15K, PAA-450K, PSS-70K and PAL-15K (in the direction of the arrows). The absorption peaks corresponding to the vibration of the hydroxyl group are indicated with asterisks.

In addition, the broad absorption peak around 3300 cm^{-1} and the small peak around 1650 cm^{-1} are characteristic for the vibrations of the -OH group, indicating that the synthesized ACC particles contain structural water.[33, 157, 225] The amorphous structure of these particles is confirmed by the absence of any sharp peak in the XRD traces, as shown in Figure 4.2d.

4.2.2 Humidity-induced crystallization kinetics

To monitor the kinetics of the humidity-induced crystallization of ACC, we expose ACC particles to a N_2 gas atmosphere possessing a RH around 95% and measure their structure using time-resolved *in situ* FTIR. When ACC particles are exposed to such a humid environment, we observe the characteristic ν_2 peak around 874 cm^{-1} and ν_4 peaks between 700 and 750 cm^{-1} corresponding to crystalline CaCO_3 appearing, as exemplified for AA-functionalized ACC in Figure 4.3a and unfunctionalized ACC in Figure 4.3b. The intensity of these peaks increases with increasing exposure time while the intensity of the ν_2 peak characteristic for ACC around 863 cm^{-1} gradually decreases. If these particles are sufficiently long exposed to this humid environment, the characteristic ν_2 peak of ACC disappears and the intensity of the ν_2 peak around 874 cm^{-1} and the ν_4 peaks between 700 and 750 cm^{-1} level off, indicating that the crystallization of ACC is complete. These results are in good agreement with reports on the crystallization of unfunctionalized ACC particles that are induced through the exposure to a humid environment[121] or water drops.[90]

To determine the crystallization kinetics of ACC, we extract the degrees of crystallization (α) from the time-resolved *in situ* FTIR data. By approximating that the intensity of the absorption peaks in the FTIR spectra scales linearly with the amount of the corresponding chemical species, we can estimate the amount of crystals from the intensity of the ν_4 peaks or that of the ν_2 peak around 874 cm^{-1} . Similarly, we can extract the amount of ACC from the intensity of the ν_2 peak around 863 cm^{-1} . We then measure the intensity of the ν_4 peak at 712 cm^{-1} characteristic for calcite and that at 744 cm^{-1} characteristic for vaterite and use the sum of the intensities ($I_{\nu_4, t_{rh}}$) of these two peaks to obtain the relative amount of crystals at the exposure time (t_{rh}). In addition, we approximate that the degree of crystallization at the end of the crystallization is one. Hence, we can determine the degree of crystallization at specific t_{rh} as,

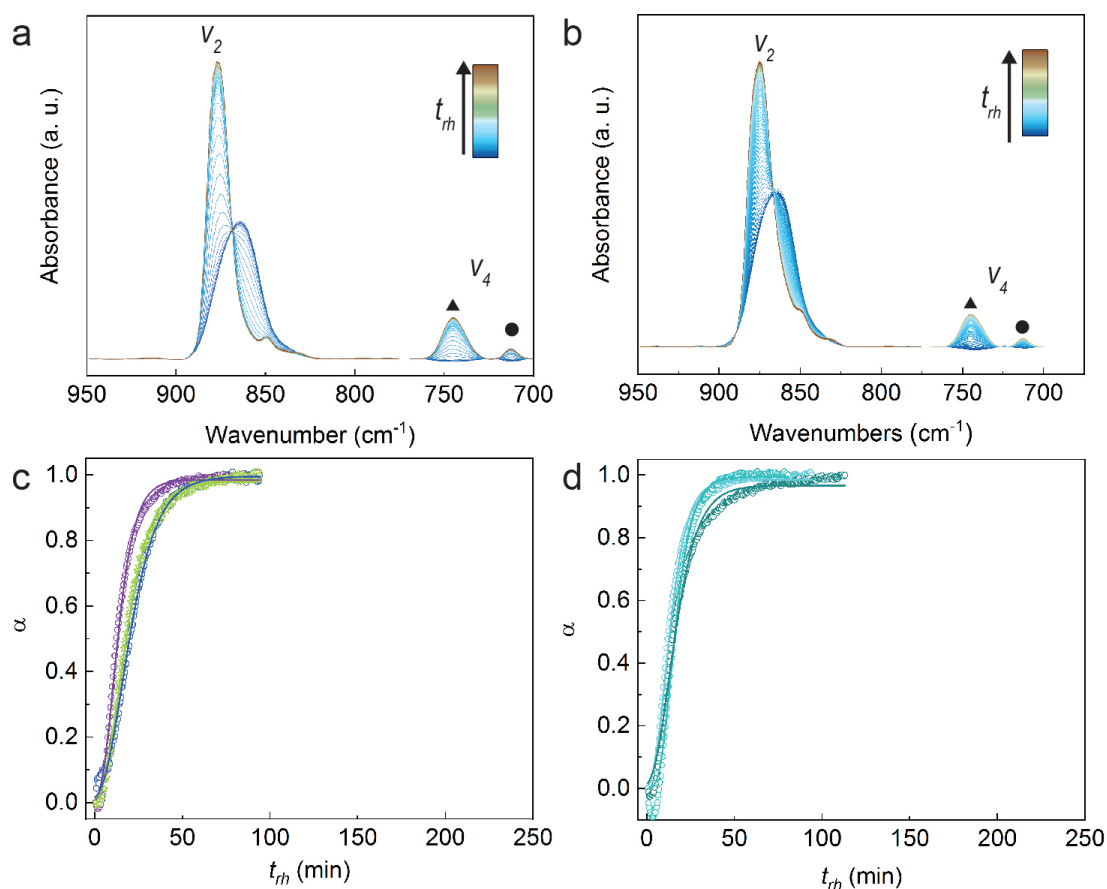


Figure 4.3 – Structural evolution of ACC particles if exposed to a *RH* around 95%. (a,b) Time-resolved FTIR spectra of (a) AA-functionalized ACC particles and (b) unfunctionalized counterparts measured *in situ* when they are exposed to the high humidity. The baselines of these spectra are subtracted. The ν_4 features corresponding to vaterite are indicated with triangles (▲) and those corresponding to calcite with circles (●). (c) Degree of crystallization as a function of the exposure time for unfunctionalized ACC particles extracted from the intensities of different absorption peaks in the *in situ* FTIR traces. α_{ν_4} is indicated in green, α_{ν_2-cry} in violet and α_{ν_2-acc} in blue. (d) Degree of crystallization as a function of the exposure time obtained from three different repetitions of *in situ* FTIR measurements of unfunctionalized ACC.

$$\alpha_{\nu_4, t_{rh}} = \frac{I_{\nu_4, t_{rh}} - I_{\nu_4, 0}}{I_{\nu_4, e} - I_{\nu_4, 0}} \quad (4.1)$$

where $I_{\nu_4, 0}$ is the sum of intensities of the two ν_4 peaks measured at $t_{rh} = 0$ and $I_{\nu_4, e}$ is that measured in the end of the crystallization.

Similarly, we can extract the relative amount of crystals from the intensity of the ν_2 peak around 874 cm^{-1} . Due to the difficulty of directly deconvoluting the ν_2 peak corresponding to crystalline CaCO_3 and that corresponding to ACC, we measure the intensity of the overall ν_2 peak at 874 cm^{-1} ($I_{\nu_2-cry, t_{rh}}$) after an exposure time t_{rh} . We can also obtain the corresponding degree of crystallization as,

$$\alpha_{\nu_2-cry, t_{rh}} = \frac{I_{\nu_2-cry, t_{rh}} - I_{\nu_2-cry, 0}}{I_{\nu_2-cry, e} - I_{\nu_2-cry, 0}} \quad (4.2)$$

Alternatively, we can extract the relative amount of ACC by measuring the intensity of the overall ν_2 peak at 863 cm^{-1} ($I_{\nu_2-acc, t_{rh}}$). The degree of crystallization at t_{rh} is expected to be equal to the amount of ACC that has been transformed at this time, expressed as,

$$\alpha_{\nu_2-acc, t_{rh}} = 1 - \frac{I_{\nu_2-acc, t_{rh}} - I_{\nu_2-acc, 0}}{I_{\nu_2-acc, e} - I_{\nu_2-acc, 0}} \quad (4.3)$$

Indeed, the degree of crystallization as a function of the exposure time determined by analyzing these three different peaks are in good agreement with each other, as shown in Figure 4.3c. As the ν_2 peak at 874 cm^{-1} has the highest intensity among these three peaks, it contains the smallest error that is introduced from the baseline subtraction. Therefore, we use this peak to calculate α for all the studied ACC samples. Moreover, to test the reproducibility of the humidity-induced crystallization kinetics, we carry out three repetitions of *in situ* FTIR measurements on the unfunctionalized ACC and ACC functionalized with AA and PAA-450K, which crystallize relatively fast. For all these three samples, the crystallization kinetics obtained from different repetitions are very similar, as exemplified with the case of unfunctionalized ACC in Figure 4.3d, indicating that our analysis is robust and reproducible.

To compare the crystallization kinetics of all the studied ACC samples, We plot their degrees of crystallization as a function of exposure time, as shown in Figure 4.4a. Each

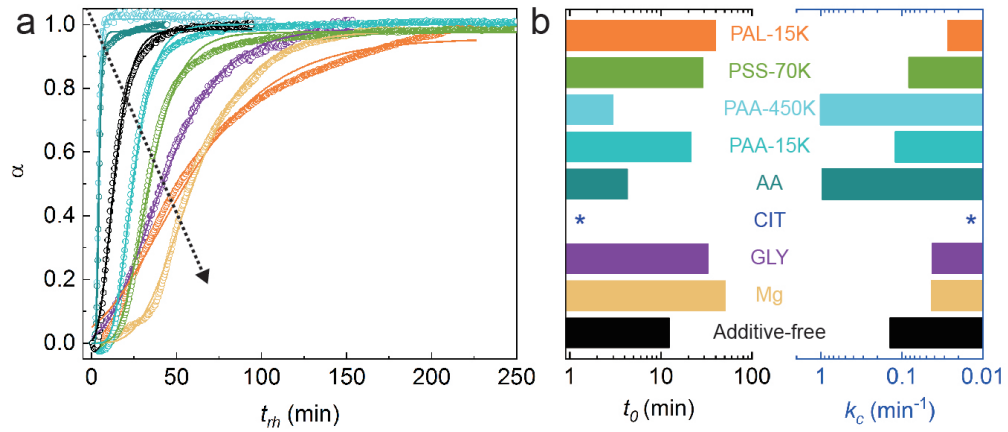


Figure 4.4 – Kinetics of the humidity-induced crystallization of ACC particles at a RH around 95%. (a) Degree of crystallization as a function of the exposure time. The values extracted from the time-resolved *in situ* FTIR measurements are indicated with empty symbols and the fits with solid lines. In the direction of the arrow, the traces correspond to ACC particles functionalized with PAA-450K or AA, unfunctionalized ACC, and ACC functionalized with PAA-15K, PSS-70K, Gly, PAL-15K or Mg. (c) Induction time and crystallization rate coefficient of ACC obtained by fitting the traces of degree of crystallization as a function of time with the Gompertz model. There was no sign of crystallization of CIT-functionalized ACC within 6 h in the *in situ* FTIR measurements, such that we could not determine these values for it.

trace is subsequently fitted with the Gompertz model,

$$\ln \alpha = -e^{(-k_c(t_{rh}-t_0))} \quad (4.4)$$

which has previously been employed to describe the kinetics of the humidity-induced crystallization of ACC.[131] From these fits, we extract the induction time required to detect first signs of the crystallization (t_0) and the crystallization rate coefficient (k_c), as summarized in Figure 4.4b. The t_0 for unfunctionalized ACC particles is 12.4 min and k_c is 0.14 min⁻¹. The functionalization of ACC with AA or PAA-450K decreases t_0 and increases k_c , indicating that these additives decrease the kinetic stability of ACC against the humidity-induced crystallization. By contrast, the functionalization with Mg, Gly, PAA-15K, PSS-70K, or PAL-15K, increases t_0 and decreases k_c , indicating that these additives increase the kinetic stability of ACC. Remarkably, even though the amount of CIT added during the synthesis of ACC is three-fold lower than that of the other tested additives, CIT-functionalized ACC does not crystallize after having been exposed to the same humid environment for 6 h, as determined with *in situ*

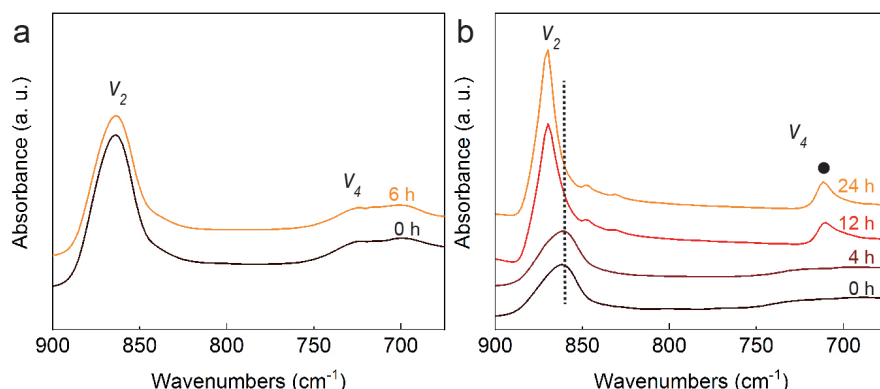


Figure 4.5 – Crystallization kinetics of CIT-functionalized ACC particles that are synthesized from an aqueous solution containing CIT and Ca^{2+} with a molar ratio of 1:30, if exposed to a RH around 95%. (a,b) FTIR spectra of particles measured (a) *in situ* and (b) *ex situ* if exposed to such humidity for different durations.

FTIR measurements and shown in Figure 4.5a. Indeed, we only observe signs of crystallization after these particles have been exposed to this humid environment for 12 h, as shown in the *ex situ* FTIR results in Figure 4.5b. These results indicate that the kinetics of the humidity-induced crystallization and hence the kinetic stability of ACC can be tuned with additives, by analogy to the crystallization induced in bulk solutions or through the exposure to elevated temperatures.

The functionalization of ACC particles with additives imparts different kinetic stabilities to them. Remarkably, the kinetic stability of ACC particles functionalized with AA monomers, PAA-15K, and PAA-450K differs significantly even though they all possess the same functional group: PAA-15K increases the kinetic stability of ACC, whereas AA and PAA-450K reduce it, as shown in Figure 4.4. This result indicates that the molecular weight of additives influences the kinetic stability of additive-functionalized ACC if exposed to a humid environment. In addition, the kinetic stability of ACC is influenced by the composition of the functional group: ACC functionalized with PAL-15K displays a much higher kinetic stability than PAA-15K-functionalized counterparts even though their average molecular weight is very similar. In good agreement with this indication, we observe distinctly different kinetic stabilities for ACC particles functionalized with small molecules that possess similar molecular weights: AA, Gly, Mg, and CIT. These results suggest that the kinetic stability of additive-functionalized ACC if exposed to a humid environment depends on the composition of the functional groups and molecular weight of the additives, in good agreement with the results obtained for additive-functionalized ACC particles that are exposed to bulk

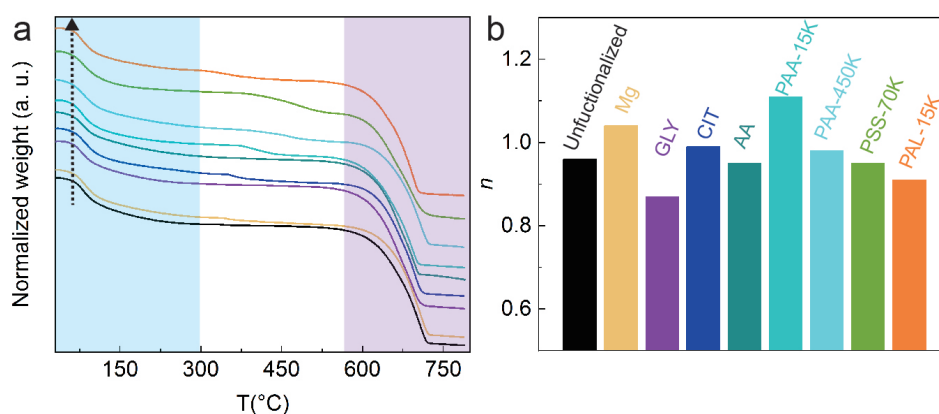


Figure 4.6 – Degrees of hydration of ACC particles. (a) Normalized TGA curves of as-synthesized unfunctionalized ACC particles (bottom) and those functionalized with Mg, Gly, CIT, AA, PAA-15K, PAA-450K, PSS-70K or PAL-15K (in the direction of the arrow). The temperature range corresponding to the evaporation of water contained in ACC particles is indicated in blue and that corresponding to the decomposition of CaCO_3 into CaO and CO_2 in violet.[165] (b) Degrees of hydration of particles extracted from TGA measurements.

solutions[122, 138, 143, 252] or elevated temperatures.[86, 122, 138]

The kinetic stability of ACC against the humidity-induced crystallization has been shown to depend on n of ACC: A higher n results in a lower kinetic stability.[86] To test if the observed effects of the composition of the functional groups and molecular weight of the additives on the kinetic stability of ACC are related to differences in n , we quantify n for all the ACC samples using TGA. The degrees of hydration for most of the additive-functionalized and unfunctionalized ACC particles synthesized here are around 1 without significant differences between each other, as shown in Figure 4.6, and well in agreement with literature.[81, 92] Indeed, even if n of ACC functionalized with PAA-15K is slightly higher than that of ACC functionalized with PAA-450K, it displays a significantly higher kinetic stability, as shown in Figure 4.4. These results indicate that the observed differences in the kinetic stability are not caused by the different degrees of hydration of ACC particles.

The kinetic stability of ACC particles that are exposed to humid environments has also been shown to depend on the size of these particles: Smaller ACC particles display a higher kinetic stability.[86] To test if ACC particles functionalized with different additives possess different sizes, we quantify this parameter using SEM, as shown in Figure 4.7. The diameters of the synthesized ACC particles range from 30 nm to

Influence of the Additives on the Humidity- and Pressure- Induced Crystallization

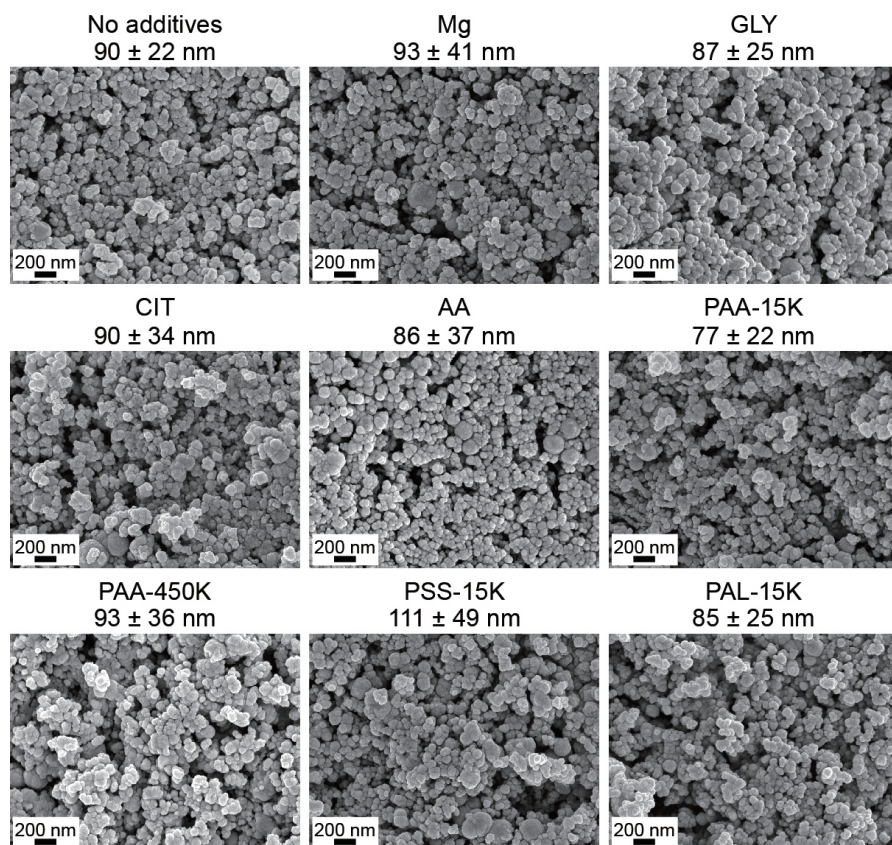


Figure 4.7 – Size of ACC particles. SEM images of as-synthesized unfunctionalized ACC particles and those functionalized with different additives. The average diameters of particles are quantified from SEM images using the Digimizer software by averaging at least 70 particles, as indicated on top of each image.

300 nm without significant differences between different ACC samples. Even if the size of AA-functionalized ACC is slightly smaller than that of ACC functionalized with Mg, Gly, CIT or PSS-15K, its kinetic stability is much higher, as shown in Figure 4.4. These results suggest that the measured difference in the kinetic stability cannot be explained with differences in the sizes of ACC.

To elucidate the reason for the dependence of the kinetic stability of ACC on the composition of the functional groups and the molecular weight of additives, we must understand the pathway of the humidity-induced crystallization of ACC. Humidity-triggered crystallization has been suggested to occur through a surface-coupled partial dissolution-precipitation pathway, where water contained in the humid environment is absorbed on the surface of ACC and partially dissolves it. Thereby, a supersaturated solution forms in proximity of the particle surface from which CaCO_3

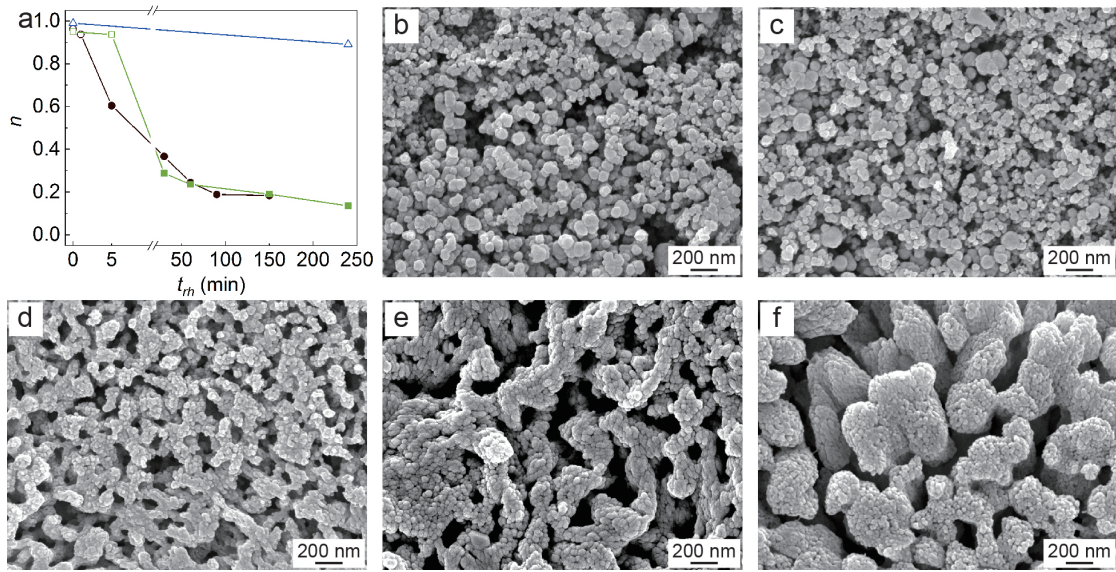


Figure 4.8 – Evolution of the degree of hydration and morphology of ACC particles if exposed to a RH around 95%. (a) n for unfunctionalized ACC particles (●) and those functionalized with PSS-70K (■) or CIT (▲) as a function of t_{rh} , quantified using TGA. Samples that remain amorphous are indicated as empty symbols whereas those containing crystalline CaCO_3 are depicted as solid symbols. (b-f) SEM images of ACC particles functionalized with PSS-70K after having been exposed to the humid environment for (b) 0 min, (c) 5 min, (d) 30 min, (e) 150 min, and (f) 240 min.

crystals can start to form.[1, 40, 86, 121, 123, 131] It has been demonstrated that for ACC particles initially possessing a n of 0.4, the dissolution-reprecipitation process only occurs if n increases to values above 0.65.[123] Hence, a significant amount of water contained in the humid environment must be absorbed on the surfaces of ACC particles before crystallization can occur, resulting in an induction time.[131] To check if a measurable amount of water is absorbed on the surfaces of ACC particles studied here, we measure n of particles as a function of the time which they are exposed to the humid environment for using TGA. We conduct this analysis on unfunctionalized ACC that shows a fast crystallization kinetics and ACC functionalized with PSS-70K and CIT that displays a slow crystallization kinetics, as previously shown in Figure 4.4. Despite their striking difference in the crystallization kinetics, none of these three samples displays a measurable increase in n during the induction stage, as shown in Figure 4.8a. In line with this observation, the morphology of these particles does not change during this process, as shown in the SEM images in Figures 4.8b-c and Figures 4.9b-c. These results indicate that water absorption does not measurably influence t_0 in the induction stage. Instead, we expect t_0 to depend on the kinetics of

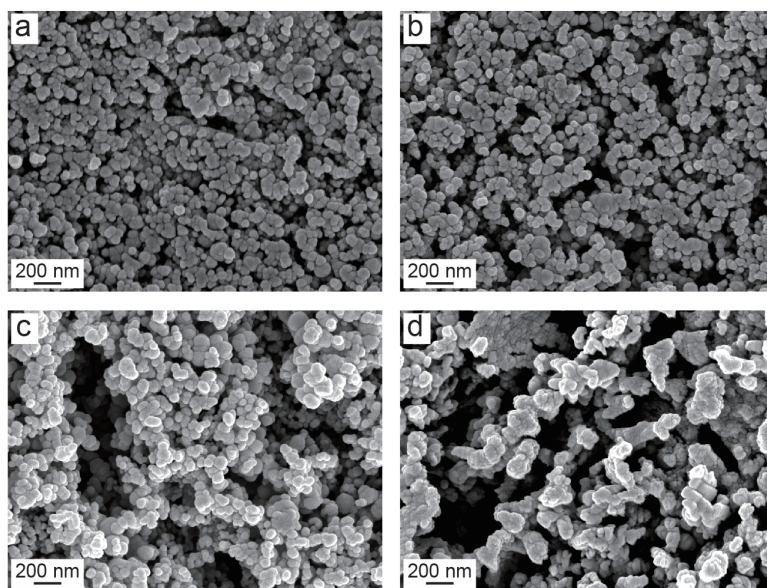


Figure 4.9 – Evolution of the morphology of unfunctionalized ACC particles. (a-d) SEM images of unfunctionalized ACC particles after having been exposed to a RH around 95% for (a) 0 min, (b) 1 min, (c) 5 min, and (d) 30 min.

the partial dissolution-reprecipitation process of ACC. Once ACC starts to crystallize into the anhydrous crystalline forms vaterite or calcite, water contained in ACC is expelled and accelerates the partial dissolution-reprecipitation process of adjacent ACC, as shown in Figure 4.4 and Figure 4.8a. Similarly, we expect k_c to depend on the kinetics of the partial dissolution-reprecipitation process of ACC. During this process, we observe a coalescence of particles that results in an increase in the average particle size, as shown in Figures 4.8d-f and Figures 4.9c-d. These results suggest that the composition of the functional groups and the molecular weight of additives influence the kinetics of the partial dissolution-reprecipitation, [1, 86] thereby affecting the humidity-induced crystallization kinetics of ACC, including t_0 and k_c .

4.2.3 Crystals obtained from the humidity-induced crystallization

Many additives are known to influence the structure of CaCO_3 crystals that form through the crystallization of ACC in bulk solutions. [1] To test if this is also the case when ACC is exposed to a humid environment, we determine the structures of all our crystallized samples with FTIR, as shown in Figure 4.10a. Unfunctionalized ACC and ACC functionalized with Gly, AA, PAA-15K or PAA-450K, crystallize into a mixture of vaterite and calcite, as indicated by the presence of the ν_4 absorption peak around

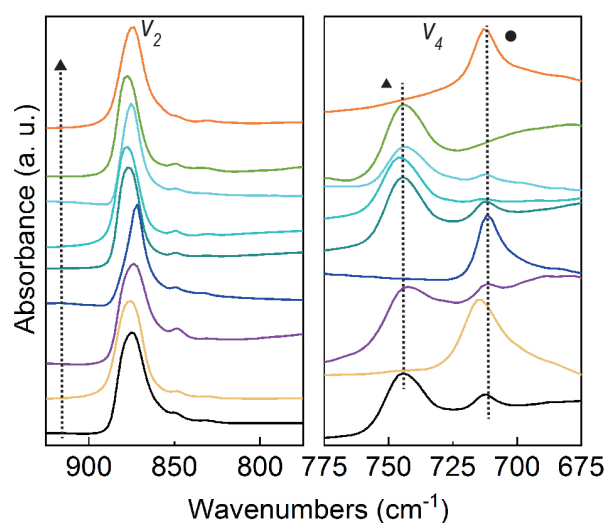


Figure 4.10 – Structure of CaCO_3 crystals after the humidity-induced crystallization of ACC. FTIR spectra of CaCO_3 crystals obtained from unfunctionalized ACC (bottom) and ACC functionalized with Mg, Gly, CIT, AA, PAA-15K, PAA-450K, PSS-70K, or PAL-15K (in the direction of the arrows).

744 cm^{-1} characteristic for vaterite and that around 712 cm^{-1} characteristic for calcite. ACC functionalized with Mg, CIT, or PAL-15K, predominantly transforms into calcite, as suggested by the presence of the ν_4 absorption peak around 712 cm^{-1} and the absence of the ν_4 absorption peak around 744 cm^{-1} . By contrast, ACC functionalized with PSS-70K predominantly transforms into vaterite, as suggested by the presence of the ν_4 absorption peak around 744 cm^{-1} and the absence of that around 712 cm^{-1} . To check if the differences in the structure translate into morphological variations, we image the formed CaCO_3 crystals with SEM. All the studied samples are composed of loosely packed nanocrystals. Samples that are composed of a mixture of vaterite and calcite contain some nanocrystals that display the rhombohedral morphology typical for calcite, whereas the rest of the samples does not possess any well-defined facets, as exemplified in Figures 4.11a-c. These results indicate that vaterite crystals obtained from the humidity-induced crystallization do not possess any well-defined facets. In line with this indication, no well-defined facets are present in the nanocrystals formed from ACC functionalized with PSS-70K, which are predominantly vaterite, as shown in Figure 4.8f. By contrast, crystals formed from ACC functionalized with Mg or CIT that mainly possess the calcite structure, have a truncated rhombohedral morphology, as shown in Figures 4.11d-e. These results indicate that certain additives influence the crystalline structure and morphology of the forming CaCO_3 crystals if the crystallization occurs in a humid environment. Interestingly, many CaCO_3

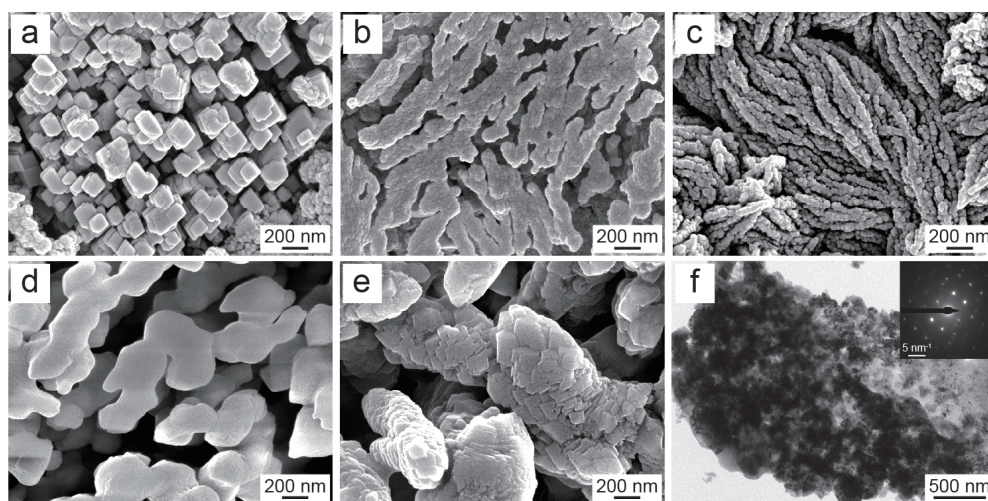


Figure 4.11 – Size, morphology and orientation of CaCO_3 crystals after the humidity-induced crystallization of ACC. (a-e) SEM images of CaCO_3 crystals obtained from (a-b) unfunctionalized ACC and ACC functionalized with (c) PAA-15K, (d) Mg, or (e) CIT. (f) TEM image of CaCO_3 crystals obtained from unfunctionalized ACC with the corresponding SAED pattern included.

nanocrystals contained in agglomerates display a similar orientation, as shown in the SEM images in Figure 4.11. The preferential orientation of nanocrystals is confirmed by the SAED patterns, as exemplified in the inset in Figure 4.11f. These results are in good agreement with those reported for the humidity-induced crystallization of unfunctionalized ACC and ACC functionalized with Mg.[40, 131]

4.2.4 Pressure-induced crystallization kinetics

The crystallization of ACC can also be induced without the addition of water if it is subjected to elevated pressures.[129, 130] To study the influence of additives on the kinetics of the pressure-induced crystallization, we uniaxially pressurize ACC for 30 min and subsequently measure its structure *ex situ* using FTIR and XRD. We observe a shift of the ν_2 absorption peak from 863 cm^{-1} to 874 cm^{-1} , the appearance of the ν_4 absorption peak around 712 cm^{-1} , characteristic for calcite and that around 744 cm^{-1} characteristic for vaterite, if AA-functionalized ACC is subjected to pressures of 222 MPa or above, as shown in Figure 4.12a. These results indicate that these samples only start to crystallize at pressures of 222 MPa or above. They are supported by XRD measurements where sharp diffraction peaks indicating the crystalline structure only become apparent if ACC is subjected to pressures at or above 222 MPa for 30 min, as

shown in Figure 4.12b.

To compare the kinetics of the pressure-induced crystallization of unfunctionalized ACC particles with that of particles functionalized with different additives, we summarize the critical pressure (P_c) above which crystallization occurs within 30 min in Figure 4.13a. Unfunctionalized ACC has a P_c of 222 MPa. Similarly, AA-functionalized ACC has a P_c of 222 MPa, as shown in Figures 4.12c-d, indicating that AA does not measurably change the kinetic stability of ACC against the pressure-induced crystallization. Remarkably, the kinetic stability of ACC decreases if it is functionalized with PAA-450K, as indicated by the significant decrease of P_c to 87 MPa. By contrast, Mg, Gly and PAA-15K increase the kinetic stability of ACC, as indicated by the higher values of P_c . The kinetic stability of ACC is increased even more if it is functionalized with CIT, PSS-70K, or PAL-15K: These particles do not crystallize within 30 min even if subjected to a pressure of 738 MPa, which is the maximum pressure we can apply in our experimental set-up, as shown in Figures 4.12e-f. Indeed, these samples only crystallize if they are subjected to 738 MPa for a critical amount of time (t_c), as summarized in Figure 4.13b. These results demonstrate that additives influence the kinetics of crystallization of ACC not only if exposed to humid environments but also if subjected to elevated pressures.

Our results of the humidity-induced crystallization demonstrate that the kinetic stability of ACC depends on the composition of the functional groups and the molecular weight of additives. To test if this is also the case for the pressure-induced crystallization, we compare the values of P_c and t_c for ACC particles functionalized with AA, Gly, Mg and CIT. Indeed, P_c and t_c of ACC particles functionalized with these different additives vary significantly even though the molecular weight of these additives is similar, as shown in Figure 4.13. These results indicate that the composition of the functional groups of additives also influences the kinetic stability of ACC against the pressure-induced crystallization. Similarly, the molecular weight of the additives influences the kinetic stability: P_c of AA-functionalized ACC is similar to that of unfunctionalized ACC, whereas that of ACC functionalized with PAA-15K is higher and that of ACC functionalized with PAA-450K is lower, as summarized in Figure 4.13a. By contrast, the kinetic stability of ACC against pressure-induced crystallization does not scale with n or the size of ACC particles studied here, by analogy to that against the humidity-induced crystallization, as indicated by the comparison between Figure 4.13, Figure 4.6 and Figure 4.7.

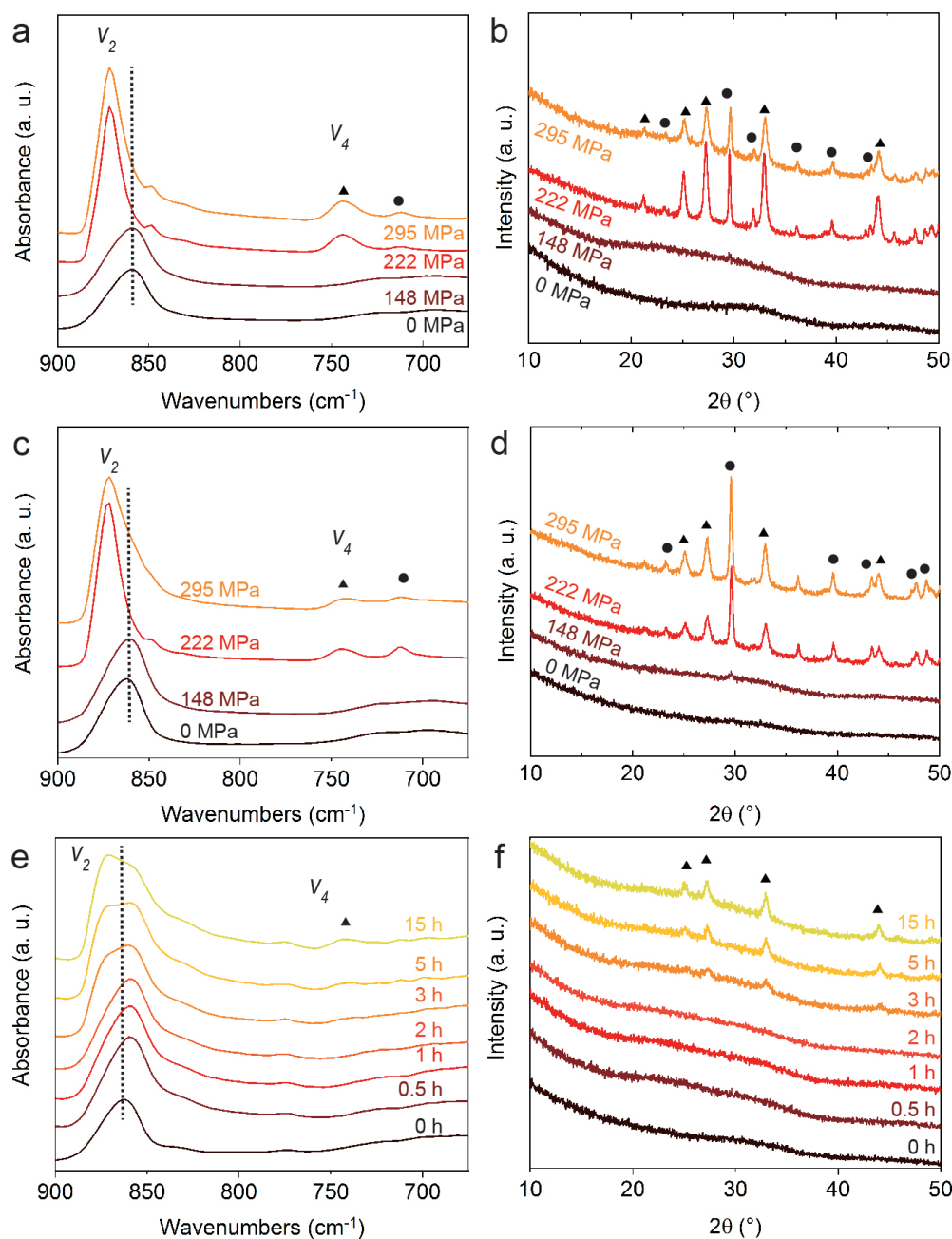


Figure 4.12 – Pressure-induced crystallization of ACC particles. (a,c) FTIR traces and (b,d) XRD patterns of (a,b) AA-functionalized ACC and unfunctionalized one after having been exposed to different pressures for 30 min. (e) FTIR traces and (f) XRD patterns of ACC particles functionalized with PSS-70K after having been exposed to 738 MPa for different durations.

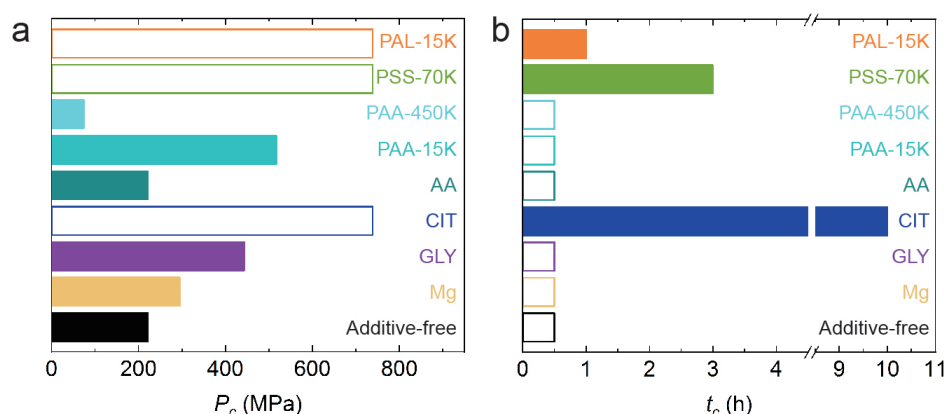


Figure 4.13 – Comparison of the pressure-induced crystallization kinetics of ACC particles. (a) Critical pressure where crystallization is observed if ACC is pressurized for 30 min. Samples possessing a critical pressure above 738 MPa, the maximum pressure that our experimental set-up can achieve, are indicated as empty bars. (d) Critical time that it takes ACC to crystallize if subjected to a pressure of 738 MPa. Samples that crystallize within 30 min are indicated as empty bars.

The composition of the functional groups of additives and their molecular weight influence the kinetic stability of ACC against the humidity- and pressure-induced crystallization. However, the effect of certain additives on the stability of ACC against crystallization is distinctly different for these two crystallization processes, as a comparison between Figure 4.4 and Figure 4.13 reveals. For example, while Mg-functionalized ACC displays a higher kinetic stability against the humidity-induced crystallization than ACC functionalized with Gly, PAA-15K, or PSS-70K, it shows a lower kinetic stability against the pressure-induced crystallization. A similar process-dependent effect of certain additives on the stability of ACC against crystallization has been reported if ACC particles were exposed to bulk water or elevated temperatures.[122, 127] In this case, the difference in the effect of additives was attributed to differences in the crystallization pathways. By analogy, the difference in the effects of additives observed here indicates that ACC crystallizes through a different pathway if exposed to a humid environment or to elevated pressures.

The pressure-induced crystallization of ACC has been suggested to occur through a solid-state transformation.[130] If this is the case, ACC must be fully dehydrated before CaCO_3 crystals can start to form, by analogy to the temperature-induced crystallization.[1, 77, 86, 121, 122, 225] To test if the pressure-induced crystallization indeed occurs through a solid-state transformation, we quantify the evolution of n of ACC when subjected to 738 MPa using TGA. To obtain a high temporal resolution,

Influence of the Additives on the Humidity- and Pressure- Induced Crystallization

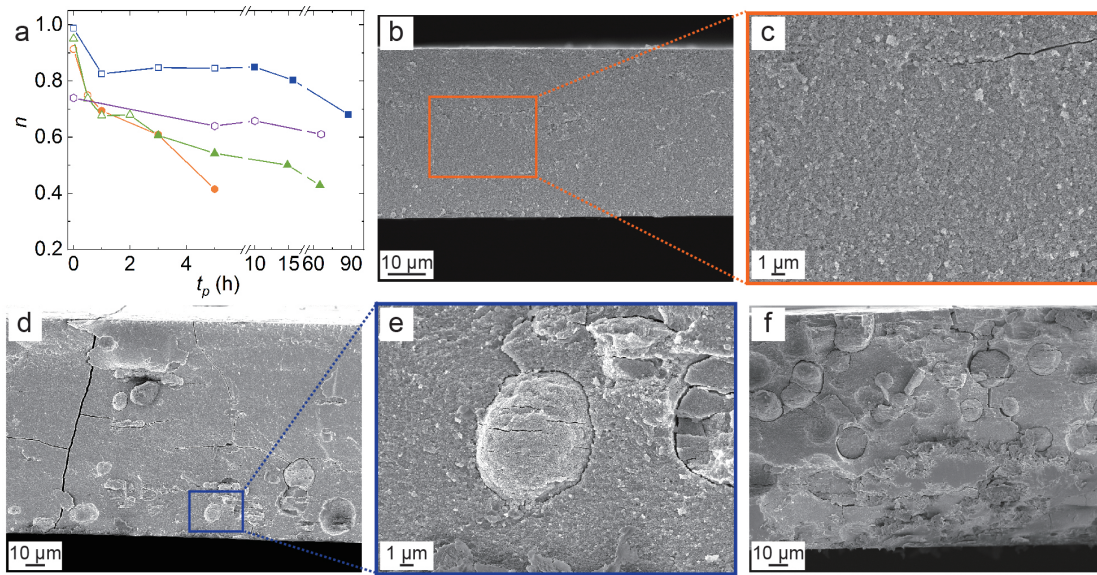


Figure 4.14 – Evolution of the degree of hydration and morphology of ACC particles if subjected to a pressure of 738 MPa. (a) n for ACC functionalized with PAL-15K (●), PSS-70K (▲), CIT (■), and PSS-70K that has been annealed at 100 °C for 10 min (●) as a function of the time (t_p) they have been exposed to 738 MPa, as measured using TGA. Samples that remain amorphous are indicated with empty symbols and crystallized samples with solid symbols. (b-f) Cross-section SEM images of compacted films obtained by pressing ACC functionalized with PSS-70K for (b-c) 10 min, (d-e) 10 h, and (f) 68 h.

we quantify the evolution of n of ACC that is functionalized with PAL-15K, PSS-70K or CIT and hence, crystallizes slowly, as summarized in Figure 4.14a. n measured for ACC functionalized with CIT decreases from 1 to 0.82 within 1 h, even though we can observe the first sign of crystallization only after 10 h, as previously shown in Figure 4.13b. Similar results are obtained for the other two ACC samples. These results indicate that ACC can dehydrate while being exposed to elevated pressures, consistent with the results previously reported for unfunctionalized ACC.[124] Interestingly, if ACC functionalized with PSS-70K or CIT is subjected to such pressures for an extended amount of time, its n remains nearly constant until it starts to crystallize. Once the crystallization is initiated, n of these samples further decreases, suggesting that ACC only partially dehydrates before it starts to crystallize. This finding is in stark contrast to the full dehydration that is typically observed for the temperature-induced solid-state transformation.[1, 77, 86, 121, 225]

The dehydration of ACC is endothermic,[80, 86, 114, 118] such that external energy is often required to initiate this process.[1] This can be achieved, for example, by

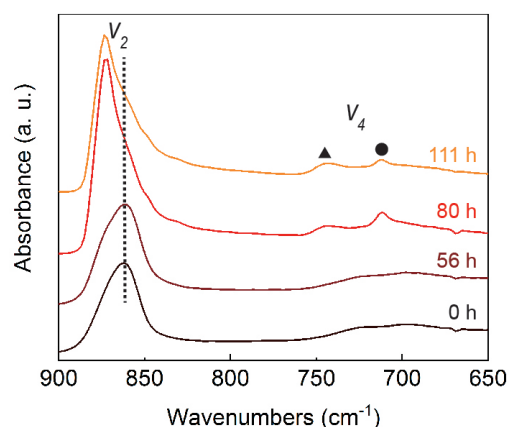


Figure 4.15 – Crystallization kinetics of unfunctionalized ACC if exposed to ambient air with a *RH* around 50%. FTIR spectra of particles after having been exposed to ambient air for different time.

subjecting ACC to elevated temperatures[77, 86, 121, 225] or pressures.[124] The kinetics of this process is mainly controlled by the interaction strength between water and ions contained in ACC.[1, 77, 96, 118, 225] Weakly interacting water, often called mobile water, is released easily, whereas the strongly bound water, often called rigid water, is released only if a sufficient amount of energy is input into the system.[76, 77, 96, 110, 114, 118, 225] Here, we also observe two distinct regions of dehydration: The first region of dehydration is observed before we can measure any sign of crystallization, suggesting that mobile water is expelled before the crystallization is initiated. The second region of dehydration is only observed after the crystallization is initiated. This observation suggests that the pressure is insufficient to expel the rigid water to initiate the solid-state transformation. Instead, the crystallization might occur through a dissolution-reprecipitation pathway that typically requires a significantly lower energy than the solid-state transformation.

A dissolution-reprecipitation process of ACC typically requires water to dissolve ACC such that a supersaturated solution with respect to the crystalline CaCO_3 results, from which crystals start to form. To check if the amount of water contained in ambient air is sufficient to initiate this process, we expose unfunctionalized ACC particles to ambient air that has a *RH* around 50% without applying any pressure and measure their crystallization kinetics *ex situ* with FTIR. We cannot detect any sign of crystallization even after the particles have been exposed for 56 h, more than 100 times longer than the time it takes these particles to crystallize at elevated pressures, as shown in Figure 4.15. This observation indicates that the humidity of ambient air

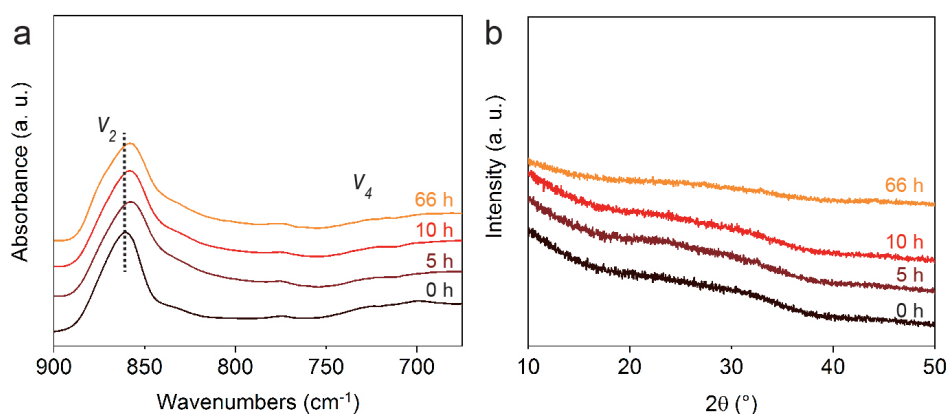


Figure 4.16 – Kinetic stability of ACC particles functionalized with PSS-70K that has been annealed at 100 °C for 10 min, if subjected to 738 MPa. (a) FTIR traces and (b) XRD patterns of annealed particles after having been exposed to 738 MPa for different durations.

does not measurably influence our pressure-induced crystallization results. Instead, the dissolution-precipitation process is most likely initiated by the mobile water that is released during the partial dehydration of ACC particles under elevated pressures. Indeed, we observe that several micro-sized crystals form within a compact film composed of dehydrated ACC particles, as shown in SEM images in Figures 4.14b-e. This observation suggests that the released mobile water accumulates within certain regions of the film composed of ACC particles because these samples are contained in a closed die. This accumulated water initiates the local dissolution-precipitation of adjacent ACC particles. Interestingly, this suggestion is in contrast to the surface-coupled partial dissolution-precipitation process observed in the humidity-induced crystallization; in this case, the crystallization starts at the interface between the ACC particles and the humid gas, as shown Figure 4.8 and Figure 4.9. Once the dehydrated ACC transforms into anhydrous vaterite or calcite, rigid water previously contained in ACC is released and accelerates the dissolution-precipitation process of adjacent particles, thereby favoring the formation of additional and larger CaCO_3 crystals, as shown in Figure 4.14f. These observations support our finding that it is not the humidity of the ambient air but the mobile water initially contained in ACC that initiates the pressure-induced crystallization of ACC. In this case, the ease of the pressure-induced crystallization is expected to depend on the amount of mobile water contained in ACC particles. This amount is much lower for CIT-functionalized ACC compared to ACC functionalized with PSS-70K or PAL-15K, as shown in Figure 4.14a. As a result, t_c of CIT-functionalized ACC particles is significantly longer

than that for particles functionalized with PSS-70K or PAL-15K if exposed to the same pressure, as exemplified in Figure 4.13b.

To further check the role of mobile water in the pressure-induced crystallization, we remove most of the mobile water contained in ACC particles functionalized with PSS-70K by annealing them at 100 °C for 10 min and subject these particles to the same pressure. Indeed, n for this ACC only slightly decreases even after having been exposed to such a high pressure for 66 h, a time that is more than 20-fold longer than t_c measured for its non-annealed ACC counterpart, as shown in Figure 4.14a and Figure 4.16. This clear difference indicates that the majority of mobile water is removed during the annealing process, thereby strongly increasing the kinetic stability of annealed ACC against the pressure-induced crystallization. These results confirm that the pressure-induced crystallization is initiated by the mobile water that is released from ACC particles when these particles are pressurized. This released water dissolves adjacent ACC particles to generate a confined aqueous solution from which CaCO_3 crystals can precipitate. In this case, additives possessing different functional groups or molecular weights likely influence the kinetic stability of ACC against the pressure-induced crystallization because they facilitate or hamper the dehydration-assisted local dissolution-reprecipitation of ACC.

4.2.5 Crystals obtained from the pressure-induced crystallization

To test if additives influence the structure of CaCO_3 crystals that form through the pressure-induced crystallization of ACC, we characterize the resulting crystals using FTIR, as shown in Figure 4.17. Crystalline samples obtained from unfunctionalized ACC and ACC functionalized with Gly, AA, PAA-15K, PAA-450K, PSS-70K, or PAL-15K are composed of a mixture of vaterite and calcite. By contrast, ACC that is functionalized with the Mg or CIT predominantly transforms into calcite. To relate the crystalline structure to the morphology of the formed crystals, we visualize them with SEM. All these samples are composed of heavily agglomerated CaCO_3 nanocrystals. However, depending on the additives contained in ACC, the size of the agglomerates varies from a few hundreds of nanometers to tens of micrometers, as shown in Figure 4.18. The vast majority of crystals contained in the samples that transform into a mixture of vaterite and calcite does not display any well-defined facets, whereas a few crystals possess the characteristic rhombohedral morphology of calcite, as exemplified in Figures 4.18a-b. Similarly, crystals formed from CIT-functionalized ACC, which are

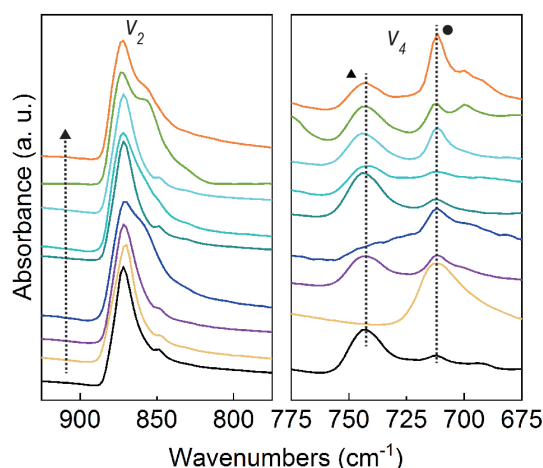


Figure 4.17 – Structure of CaCO_3 crystals after the pressure-induced crystallization. FTIR spectra of CaCO_3 crystals obtained from unfunctionalized ACC (bottom) and ACC functionalized with Mg, Gly, CIT, AA, PAA-15K, PAA-450K, PSS-70K or PAL-15K (in the direction of the arrow).

predominantly calcite, do not show any well-defined facets, as shown in Figure 4.18c. By contrast, a truncated rhombohedral morphology is present in crystals formed from Mg-functionalized ACC that mainly possess the calcite structure, as shown in Figure 4.18d. These results suggest that certain additives can influence the structure, size, and morphology of CaCO_3 crystals obtained from the pressure-induced crystallization of ACC, by analogy to what we observed for the humidity-induced crystallization.

4.3 Discussion

4.3.1 Kinetic stability of ACC

Our results suggest that additives can influence the humidity- and pressure-induced crystallization of ACC. The influence of additives on the crystallization of ACC depends on the composition of their functional groups and their molecular weight. Remarkably, certain additives tested here influence the humidity-induced crystallization of ACC in a distinctly different way than the pressure-induced crystallization. This discrepancy suggests that the crystallization under these two processing conditions follows different pathways, as schematically illustrated in Figure 4.19.

During the humidity-induced crystallization of ACC, water contained in the humid environment is absorbed on the surfaces of particles and partially dissolves part of the

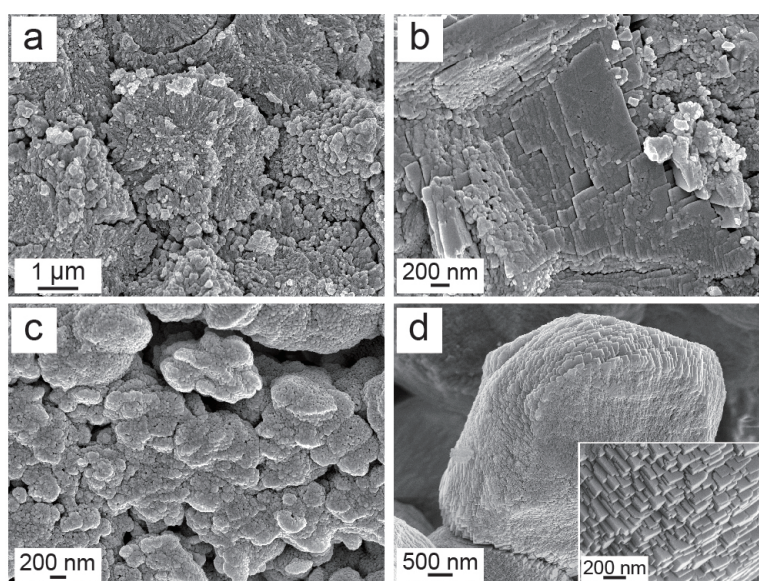


Figure 4.18 – Size and morphology of CaCO_3 crystals after the pressure-induced crystallization. (a-d) SEM images of CaCO_3 crystals formed through the crystallization of (a,b) unfunctionalized ACC and ACC functionalized with (c) CIT and (d) Mg.

surfaces such that CaCO_3 crystals form from a supersaturated solution, as shown in Figures 4.19a-b. In this case, the kinetic stability of ACC against crystallization mainly depends on the kinetics of the partial dissolution-precipitation. The kinetics of the partial dissolution-precipitation process depends on the mobility of water that is absorbed on the surfaces of particles and that initially contained in them.[1, 86, 123, 131] If no additives are contained in ACC, the mobility of water is mainly determined by the degree of hydration of ACC[1, 86, 225] and the amount of water contained in the surrounding environment.[29, 121, 131, 138] If ACC is functionalized with certain additives, such as Mg^{2+} , [157, 165] PO_4^{3-} , [128] PSS, [247] PAA, [225, 247] and Asp-rich proteins, [254] the mobility of water can also be influenced by its interaction with these additives. In this case, the kinetics of the partial dissolution-precipitation process also depends on the interaction strength between additives and water.[86, 131] The tested additives do not significantly change the degree of hydration of ACC and we keep the humidity constant. Hence, we assign the observed differences in the kinetic stability of additive-functionalized ACC to the different interaction strengths of these additives with water that result in different dissolution-precipitation kinetics.

During the pressure-induced crystallization, mobile water is released from ACC. This released water accumulates in certain regions of the pressed film composed of ACC particles, thereby initiating the local dissolution-precipitation process of ACC, as

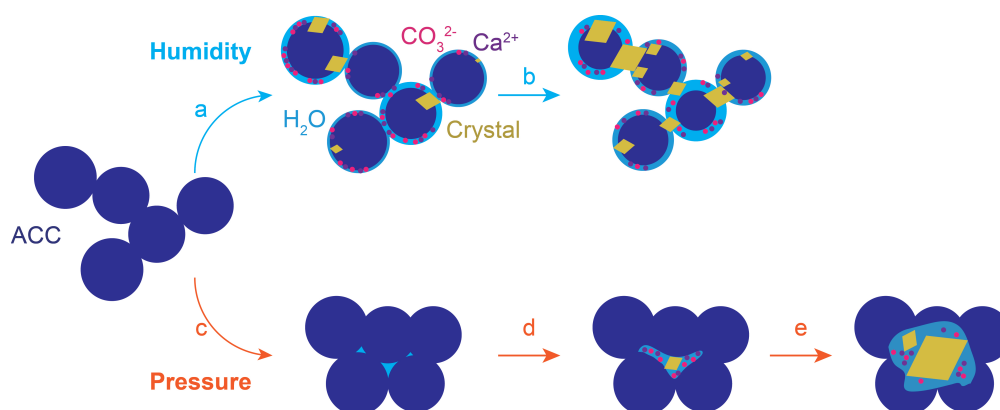


Figure 4.19 – Schematic illustration of the crystallization pathways for the humidity- and pressure-induced crystallization of ACC. (a-b) The humidity-induced crystallization follows a surface-coupled partial dissolution-reprecipitation pathway. (a) Water contained in the humid environment is absorbed on the surface of ACC particles, where it initiates the partial dissolution of ACC that is followed by the formation crystals. (b) Once ACC starts to transform into anhydrous crystals, additional water contained in ACC is released and accelerates the dissolution-reprecipitation process. (c-e) The pressure-induced crystallization follows a dehydration-assisted local dissolution-precipitation pathway. (c) While being compressed, ACC particles dehydrate. (d) The released mobile water accumulates in certain regions of the film composed of dehydrated ACC particles, where it initiates a local dissolution-reprecipitation process. (e) Once ACC starts to transform into anhydrous crystals, rigid water is released from dehydrated ACC and accelerates the dissolution-reprecipitation process.

shown in Figures 4.19c-e. Additives studied here have different interaction strengths with water[1, 165, 225] such that the dehydration kinetics of ACC functionalized with them varies. As a result, these additives influence the amount of water that is released if ACC is subjected to a defined pressure, thereby further influencing the dissolution-reprecipitation kinetics and hence, the kinetic stability of ACC against the pressure-induced crystallization.

4.3.2 Size, morphology, orientation and structure of CaCO_3 crystals

Our results demonstrate that the size and morphology of CaCO_3 crystals formed through the humidity-induced crystallization of ACC differs from those obtained from the pressure-induced crystallization. CaCO_3 crystals formed through a humidity-induced crystallization are typically composed of loosely packed nanoparticles with diameters of a few hundreds of nanometers, which resemble those of as-synthesized ACC particles. By contrast, CaCO_3 crystals obtained from the pressure-induced crystal-

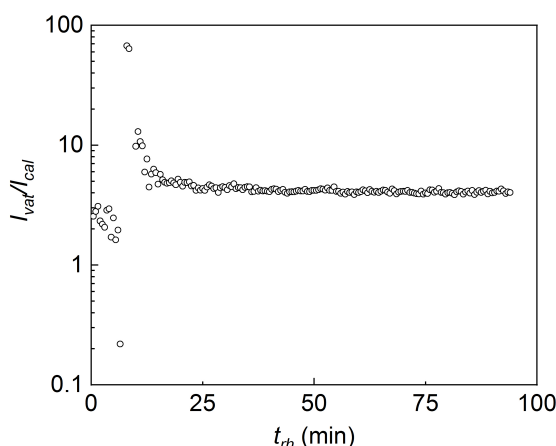


Figure 4.20 – Intensity ratio of the ν_4 peaks of vaterite and calcite ($I_{\nu_{vat}}/I_{\nu_{cal}}$) as a function of the exposure time measured with *in situ* FTIR, when unfunctionalized particles are exposed to a *RH* around 95%.

lization are typically micro-sized agglomerates composed of densely packed nanoparticles. This difference is likely caused by the varying amounts of free water present in the two crystallization processes. During the humidity-induced crystallization, a limited number of water molecules is absorbed on the surfaces of ACC particles such that these particles only partially dissolve.[40, 123] The small volume of the supersaturated solution confines the growing crystals such that their size and morphology is similar to that of the initial ACC particles.[121, 131] Moreover, the small amount of water results in a slow dissolution-reprecipitation kinetics, thereby enabling a continuous propagation of the crystal growth fronts through the amorphous phase such that the resulting crystals display a preferential orientation.[40, 131, 253] By contrast, during the pressure-induced crystallization, the released mobile water molecules accumulate in certain regions of the compacted film composed of ACC particles and locally initiate the dissolution of adjacent particles. The larger volume of the supersaturated solution enables crystals to rapidly form such that they attain a morphology and size that is similar to those formed in bulk solutions.

Unfunctionalized ACC transforms into a mixture of vaterite and calcite after the humidity- and pressure-induced crystallization, in good agreement with previous reports.[86, 129] The metastable vaterite does not transform into calcite under the conditions tested here, as indicated by the constant $I_{\nu_{vat}}/I_{\nu_{cal}}$ obtained in the *in situ* FTIR measurements in Figure 4.20. This observation is in stark contrast to reports on the formation of CaCO_3 crystals in bulk solutions, where ACC typically crystallizes into the metastable vaterite before it transforms into stable calcite.[29, 54] The structure

of CaCO_3 crystals usually depends on the degree of supersaturation of the aqueous solution: High degrees of supersaturations typically result in the formation of vaterite whereas lower degrees of supersaturations result in the formation of calcite.[81] Our results suggest that the degree of supersaturation varies throughout the samples such that vaterite and calcite simultaneously form. For vaterite to transform into the stable calcite form, it must dissolve and reprecipitate.[29, 54] The small amounts of water available during the humidity- and pressure-induced crystallization of ACC are most likely too low to enable this process such that we cannot detect any change in the ratio of calcite to vaterite in our samples.

The effects of additives on the structure of crystals obtained from the humidity- or pressure-induced crystallization depend on the composition of their functional groups and the processing conditions. For example, functionalization with Mg or CIT favors the formation of calcite if ACC is subjected to a humid environment or elevated pressures, in line with results reported for the crystallization in bulk solutions.[157, 176] By contrast, if ACC is functionalized with PSS-70K, the structure of the formed CaCO_3 crystals depends on the processing conditions: it predominantly transforms into vaterite during the humidity-induced crystallization process, and into a mixture of vaterite and calcite during the pressure-induced one. Similarly, ACC functionalized with PAL-15K primarily transforms into calcite if crystallized in a humid environment and into a mixture of vaterite and calcite if crystallized under elevated pressures. This process-dependent behavior of additives is likely related to the differences in the local supersaturations and the crystallization kinetics that exist in the two crystallization processes.[81, 123] These examples demonstrate possibilities to tune the size, morphology, orientation, and structure of CaCO_3 crystals with processing conditions without altering their composition.

4.4 Conclusion

We show that the size, morphology, structure, and orientation of CaCO_3 crystals formed from certain additive-functionalized ACC depend on the crystallization conditions: These parameters can be distinctly different if ACC is crystallized in a humid environment or at elevated pressures. We assign this process-dependent behavior to the different pathways through which ACC crystallizes: While the humidity-induced crystallization of ACC follows a surface-coupled partial dissolution-reprecipitation, the pressure-induced crystallization undertakes a dehydration-assisted local dissolution-

reprecipitation. In both crystallization pathways, the amount and mobility of water that triggers the crystallization of ACC is influenced by the composition of the functional groups of additives and their molecular weight. As a result, they display a variation in the crystallization kinetics of ACC and in the size, morphology, orientation, and structure of resulting CaCO_3 crystals. These insights provide new opportunities to more closely control the formation of CaCO_3 crystals and hence, the properties of CaCO_3 -based materials by using appropriate additives and tuning the crystallization conditions.

5 Fabrication of 2D Hexagonal Prismatic Granular Hydrogel Sheets

This chapter is adapted from the paper entitled “Fabrication of Hexagonal- Prismatic Granular Hydrogel Sheets,” authored by H. Du, A. Cont, M. Steinacher, and E. Amstad, and published in Langmuir, vol. 34, pp. 3459–3466, Mar. 2018.[227] H. Du, A. Cont and E. Amstad designed the experiments and analyzed all data. H. Du and A. Cont conducted the experiments. M. Steinacher helped with the SEM imaging. H. Du and E. Amstad wrote the paper.

In this chapter, we present a new method to fabricate 2D structured hydrogel sheets that can potentially be used as insoluble scaffolds for the fabrication of strong and tough CaCO_3 -based composite materials. These hydrogels sheets are composed of covalently crosslinked hexagonal prismatic hydrogel microparticles. We demonstrate that the structure and composition of these sheets can be tuned on a microscale by controlling the size, composition and arrangement of individual particles. We also show that their surface morphology can be varied with the polymerization conditions and their mechanical properties with their structure and composition.

Contents

5.1	Introduction	106
5.2	Results and Discussion	107
5.2.1	Fabrication of granular hydrogel sheets	107
5.2.2	Mechanical properties of hydrogel sheets	111
5.2.3	Structure, morphology and composition of hydrogel sheets . .	114
5.3	Conclusion	117

5.1 Introduction

Many natural biomineral-based composite materials have well-defined hierarchical structures and local composition that are crucial for their mechanical properties.[3–5] A prominent example is nacre: It is composed of 95 vol% of layered aragonite platelets, interspaced with 5 vol% of thin insoluble organic scaffolds composed of β -chitin and silk fibroin, as shown in Figures 1.1b-c.[5, 13, 23, 25] These insoluble organic scaffolds confine the formation of aragonite platelets, thereby enabling an excellent control over the hierarchical structure and local composition of nacre.[8, 13] In addition, these soft scaffolds allow the aragonite platelets to plastically deform if subjected to a mechanical impact, such that the toughness of nacre is 40-fold higher than that of aragonite single crystals.[4, 5, 24, 26, 27]

Inspired by the superior mechanical properties of natural biomineral-based materials, a lot of research has been devoted to designing synthetic soft materials including hydrogels that possess similar structures and mechanical properties to natural scaffolds.[151, 154, 155, 255, 256] However, these synthetic materials typically have inferior mechanical properties than natural counterparts, because they possess different structures.[5] By analogy to the self-assembly process that occurs during the formation of natural scaffolds,[257] a potential strategy to produce soft materials with well-defined structures is self-assembling individual particles into macroscopic materials and subsequently crosslinking the adjacent particles to impart the materials mechanical strengths. For example, spherical hydrogel microparticles have been assembled into superstructures[258–263] that are crosslinked through introducing reactive groups on the surfaces of particles[264] or by adding external crosslinkers.[265–

269] The structure of the resulting macroscopic hydrogels is determined by the size and size distribution of the particles and their arrangement. However, all these particles are spherical such that the area where adjacent particles are in close proximity is limited and hence, the number of crosslinks between them is insufficient. As a result, macroscopic hydrogels are fragile and often lose their integrity if removed from the substrate.[270] To improve the mechanical strength, the crosslink density between adjacent particles must be increased. Feasibility to do so has been shown for spherical microparticles with diameters below $2\text{ }\mu\text{m}$ by functionalizing their surface with additional reactive groups.[271–273] However, the control over the structure and local crosslink density of these microparticle assemblies is limited because particles are randomly assembled.[274, 275] Hence, a fabrication technique that simultaneously offers a good control over the microscale structure and local crosslink density of macroscopic hydrogels remains to be developed.

In this chapter, we develop a new protocol to fabricate 2D macroscopic hydrogel sheets made of regularly arranged, covalently crosslinked 40-120 μm diameter hexagonal prismatic hydrogel particles that display a narrow size distribution. The microscale structure and local composition of these sheets can be varied with the size, composition, and arrangement of granular components. The surface morphology can be controlled with the polymerization conditions. The mechanical properties of the sheets can be tuned with their structure and composition. These results might open up new possibilities to fabricate hydrogels that possess similar structures and mechanical properties to those of natural ones. This would also offer new opportunities to produce structured organic materials that can serve as scaffolds for the formation of minerals, thereby facilitating the fabrication of strong and tough mineral-based composites possessing well-defined structures.

5.2 Results and Discussion

5.2.1 Fabrication of granular hydrogel sheets

To produce hydrogel particles with a well-defined size, we employ emulsion drops as templates. Aqueous drops that display a narrow size distribution are produced using a microfluidic millipede device that contains 550 parallelized nozzles, each one having a triangular shape, as shown in the optical image in Figure 2.3.[236] We employ a device with 40 μm tall nozzles to produce aqueous drops with an average diameter

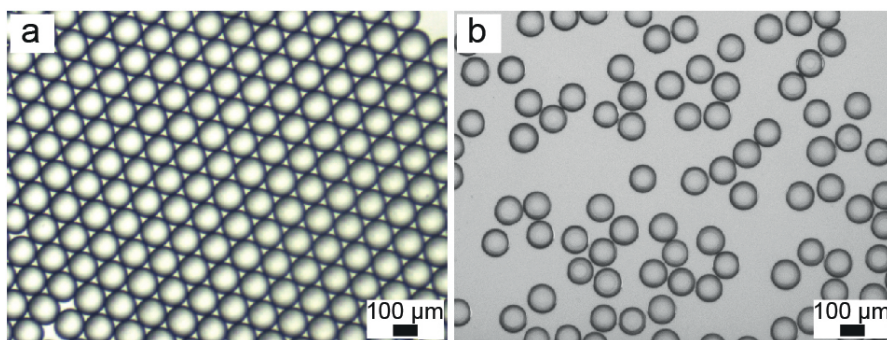


Figure 5.1 – Production of drop templates and hydrogel particles. (a,b) Optical images of (a) water-in-oil emulsion drops produced in 40 μm tall nozzles, which are illuminated with UV light to convert them into (b) hydrogel microparticles that display a coefficient of variation below 2.5%. These hydrogel particles are dispersed in water.

of 119 μm . Their coefficient of variation, defined as the standard deviation of the drop size distribution divided by the mean diameter, is as low as 2.5%, as shown in Figure 5.1a.

Two dimensional colloidal crystals composed of hard spheres are usually made by spreading a dispersion containing monodisperse colloids onto a solid substrate and letting the particles arrange into the energetically most favorable crystalline structures.[276, 277] To mimic this process, we produce aqueous drops containing PEG700-DA and photoinitiators. These drops are converted into spherical hydrogel particles through the exposure to UV light to initiate the polymerization reaction. The resulting microparticles display a narrow size distribution, as shown in Figure 5.1b. The dispersion is deposited onto a substrate composed of PDMS such that the particles sediment. To facilitate the re-arrangement of spherical hydrogel particles into the energetically most favorable hexagonal close packed structure, we agitate the substrate, as shown in Figure 5.2a. However, upon evaporation of water, the crystalline structure becomes defective because the particles shrink without being connected to each other, as shown in Figure 5.2b.

To build macroscopic materials from individual microparticles, adjacent particles must be connected to each other, for example by back-filling the structured hydrogel particles with a second matrix.[278–280] However, this procedure risks that the structure and properties of the particles are changed during the infiltration of the matrix. To overcome this limitation, adjacent particles can be connected covalently using reactive groups that are present at their surfaces. This can be achieved if drops rupture before all the monomers contained in the drops are consumed. However,

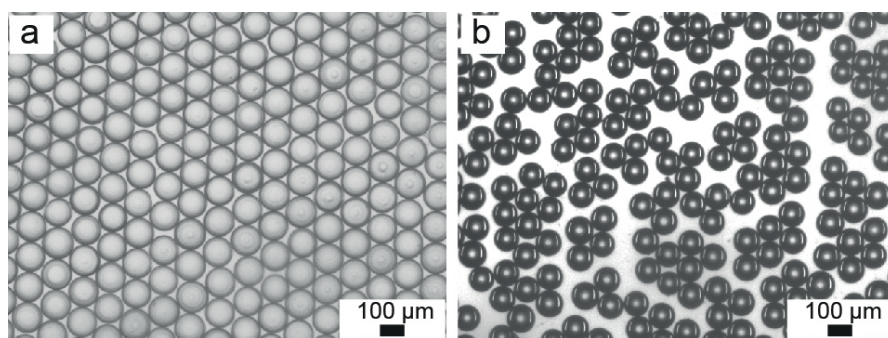


Figure 5.2 – Assembly of hydrogel particles in the wet and dry state. (a,b) Optical image of hydrogel particles (a) that are assembled into a hexagonal close packed structure in the wet state and (b) that become loosely packed upon water evaporation.

unreacted monomers can only crosslink adjacent particles, if they are located at their surface. Indeed, unreacted monomers accumulate at the surface of polymerizing particles, if they are preferentially located at the water-oil interface. This is the case if the interfacial tension between the monomers and the HFE 7500 oil is below that between the hydrogel particles and the oil.[281] Here, the interfacial tension between PEG-DA monomers and HFE 7500 is $15.7 \pm 0.1 \text{ mN}\cdot\text{m}^{-1}$; it is much lower than that between PEG-based hydrogels that contain a high fraction of water such that we assume this interfacial tension to be similar to that of water-HFE 7500 interfaces, $41.6 \pm 0.6 \text{ mN}\cdot\text{m}^{-1}$. Hence, we expect the polymerized hydrogel particles to be surrounded by monomers that can covalently link adjacent particles.

To covalently link adjacent particles, drops must rupture before all the monomers are consumed. The rate at which drops rupture depends on the oil evaporation rate, and hence is in a first approximation independent of the UV light intensity, if we neglect the heating of the UV source. The rate at which monomers are crosslinked depends on the UV light intensity. If we reduce the UV light intensity to sufficiently low values, thereby slowing down the initiation of the polymerization reaction, we expect drops to rupture before all the monomers are consumed. To test this expectation, we deposit drops on a glass slide where they spontaneously assemble into a hexagonal close packed 2D structure and let the oil evaporate, as shown in Figure 2.4. Once the majority of the oil is evaporated, drops deform to attain a hexagonal prismatic shape, as shown in the time-lapse optical images in Figures 5.3a-c. If they are subsequently illuminated for 15 s with a UV light source that is 1 cm apart from the sample, monomers polymerize before drops rupture such that individual hexagonal prismatic particles result, as shown in the SEM image in Figure 5.4a. By contrast, if we increase the distance

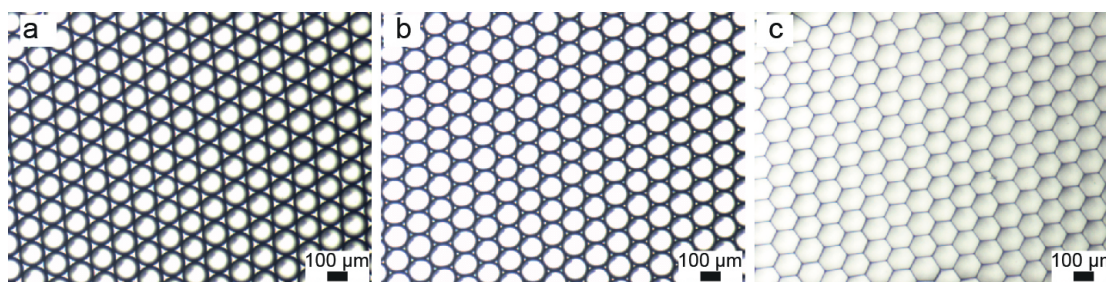


Figure 5.3 – Time-lapse optical images of self-assembled drops taken during the evaporation of the surrounding oil. (a) Monodisperse drops self-assemble into a hexagonal close packed structure. While the oil evaporates, drops (b) deform and (c) attain a hexagonal prismatic shape.

between the UV light source and the sample to 3 cm, we can easily detach a connected film composed of the hexagonal prismatic particles from the glass slide, as shown in Figure 5.4b. However, the particles are not connected through any of their side walls. Instead, they are connected through a thin film at the bottom of this structure, as shown in the SEM image in Figure 5.4c. We assign the film formation to the low contact angle between the monomer solution and the glass slide, $14 \pm 2^\circ$. Hence, the monomer containing aqueous solution wets the glass slide as soon as drops rupture. Upon exposure to UV light, the monomers contained in these thin films polymerize, thereby forming a connecting hydrogel sheet at the bottom of the particle array. While these structures are mechanically sufficiently stable to be detached from the glass slide, the sheet tends to roll. Rolling is likely caused by the free volume between adjacent hexagonal prismatic particles that is present on one side of the sheet: This free volume induces contraction of the sheet on one side only, thereby causing a non-uniform deformation that makes it cumbersome to handle.

To connect adjacent particles through their side walls we must avoid the formation of a connecting bottom layer. We expect these connecting films to form because the substrate is wetted by the monomer-containing solution. To test this expectation, we deposit drops onto a hydrophobic substrate made of PDMS; the contact angle between the monomer solution and PDMS is $87 \pm 4^\circ$. After drops attain a hexagonal prismatic shape, we illuminate them with UV light for 15 s. The resulting macroscopic sheets are again mechanically sufficiently stable to be detached from the substrate, as shown in Figure 5.5a. Sheets formed on PDMS substrates remain flat even after they have been detached from the substrate, indicating that the stress distribution along their height is more homogeneous. Indeed, there is no connecting film at the bottom

of the particle assembly, as shown in the SEM images in Figures 5.5b-c, indicating that adjacent particles are connected through their sidewalls.

5.2.2 Mechanical properties of hydrogel sheets

To quantify the influence of the granular structure of hydrogel sheets on their mechanical properties, we perform tensile tests on dried samples. The measured Young's modulus (E) of unstructured sheets is 7.7 ± 0.7 MPa, as detailed in Table 5.1, well in agreement with that measured for bulk hydrogels made of PEG-DA with similar molecular weights.[282] The measured E of hexagonal prismatic granular hydrogel sheets is higher than that of unstructured counterparts, 12.0 ± 1.0 MPa, as shown in stress-strain curve in Figure 5.6a and summarized Table 5.1. The increased stiffness of granular hydrogels suggests that the average crosslinking density is higher than that in unstructured samples. The density of covalent crosslinks depends on the monomers used to form hydrogels. Hence, the average density of covalent crosslinks should, in a first approximation, be the same in granular and unstructured hydrogels. The density of physical crosslinks depends on the density of the polymers. The initial concentration of monomers contained in the aqueous solution is the same for granular and bulk hydrogels. To produce granular hydrogels, this aqueous solution is processed into $120\ \mu\text{m}$ drops that are converted into microparticles through polymerization of the monomers contained in them. If microparticles are produced from unconfined undeformed spherical drops, they have a diameter of $99\ \mu\text{m}$, resulting in a volume of $5.1 \times 10^5\ \mu\text{m}^3$. By contrast, if particles are produced from drops that are deformed and arranged into a hexagonal close packed structure due to oil evaporation, their

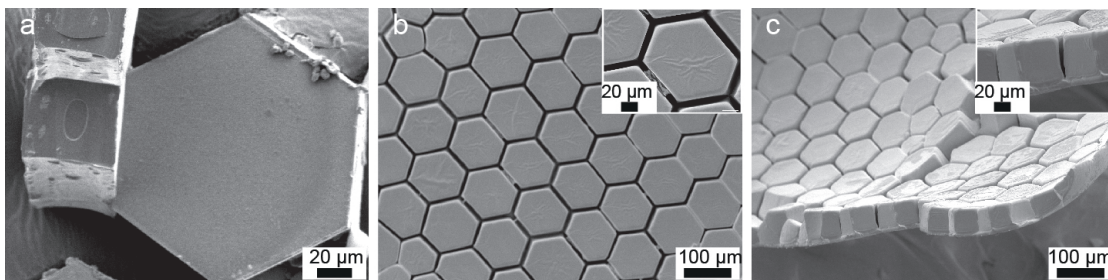


Figure 5.4 – Morphology of individual hydrogel particles and granular hydrogel sheets on a glass slide. (a) SEM image of individual hexagonal prismatic particles, obtained by polymerizing the monomers before drops ruptured. (b) Top view and (c) side view SEM images of granular hydrogel sheets made from drops that are self-assembled on a hydrophilic glass slide.

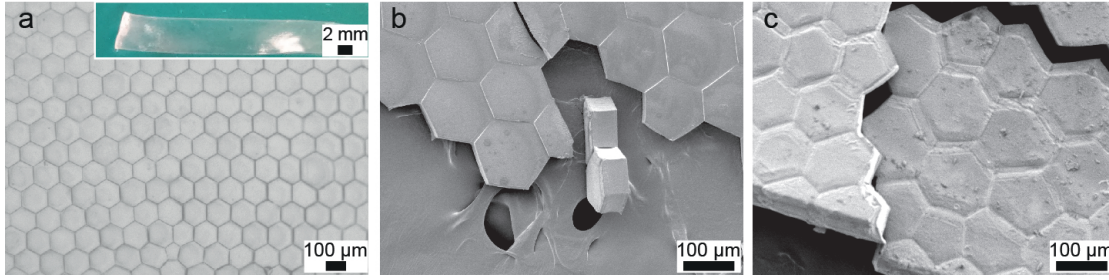


Figure 5.5 – Morphology of granular hydrogel sheets produced on a hydrophobic PDMS substrate. (a) Optical image of a hexagonal prismatic granular hydrogel sheet made by self-assembling drops on a PDMS substrate and subsequently illuminating them with UV light to convert them into hydrogels. The entire sample is shown in the photograph in the inset. (b) Top view and (c) side view SEM images of granular hydrogel sheet made from hexagonal prismatic particles that are covalently linked to each other. The sample is cut to visualize the connection between adjacent particles.

Table 5.1 – The Young’s modulus of hydrogel sheets as function of the concentration of monomers contained in drops (c_{mono}), their composition, and the hydrogel sheet structure.

c_{mono} (wt%)	M_w of PEG	Structure	E (MPa)
50	700	unstructured	7.7 ± 0.7
		granular	12.0 ± 1.0
	575	unstructured	9.6 ± 1.0
		granular	12.0 ± 1.5
40	700	unstructured	6.3 ± 0.5
		granular	9.8 ± 0.3
	575	unstructured	6.8 ± 0.8
		granular	9.6 ± 1.2

projected area is $8.9 \times 10^3 \mu\text{m}^2$ and they are $48 \mu\text{m}$ tall, such that their volume is $4.3 \times 10^5 \mu\text{m}^3$. Hence, the volume of these hexagonal prismatic particles is 16% below that of spherical counterparts while the type and number repeat units contained in this volume is the same. These results suggest that the density of physical crosslinks within the hexagonal prismatic particles is higher than that in spherical counterparts. Hence, we also expect it to be higher than that of unstructured hydrogels that are fabricated without any spatial deformation. This increased physical crosslink density within the hydrogel particles is likely a contributing reason for the increased E .

Structured sheets rupture along the grain boundaries, as shown in the SEM image in Figure 5.5c and the optical image in the inset of Figure 5.6a, by analogy to the fracture mechanism of ceramics.[283, 284] These results demonstrate that the grain

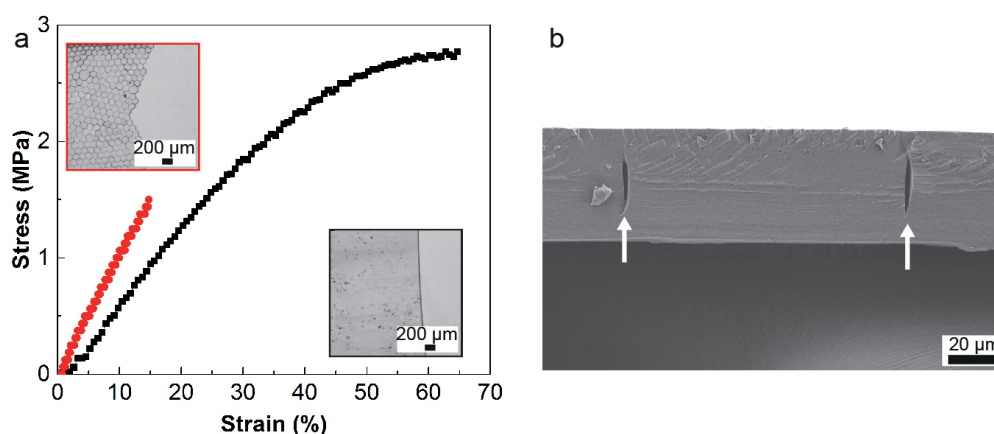


Figure 5.6 – Mechanical properties of hydrogel sheets. (a) Stress as a function of strain for unstructured (black) and structured, granular (red) PEG700-DA hydrogel sheets. Optical images of the corresponding ruptured sheets are shown in the insets. (b) SEM image of the cross-section of a granular hydrogel sheet. The white arrows indicate the voids present in the grain boundaries.

boundaries are the weakest points of the hydrogels. Moreover, these results suggest that the low ductility and toughness observed for the granular hydrogels is related to the grain boundaries. To investigate possible reasons for this reduction in toughness and ductility, we visualize a cross-section of the granular hydrogels using SEM. Grain boundaries encompass long voids, as shown in Figure 5.6b. These voids, which are defects within the granular structure, facilitate crack propagation, thereby lowering the ductility and toughness of the granular hydrogels.

The increase in E and the decrease in fracture toughness and ductility caused by introducing grain boundaries into hydrogel sheets indicate that the crosslink density inside the particles is high whereas that between adjacent particles is low. We expect this difference in crosslink density to decrease if the density of covalent crosslinks is increased. To test this expectation, we produce particles from PEG-DA with a lower molecular weight, PEG575-DA, which results in a higher density of covalent crosslinks. Also for these samples, E of hexagonal prismatic granular hydrogel sheets is significantly higher than that of unstructured counterparts. However, in agreement with our expectation, the difference in Young's moduli decreases to 25% as summarized in Table 5.1.

The density of physical crosslinks depends on the density of polymers and hence on the initial monomer concentration. To test the influence of the physical crosslink density on the mechanical properties, we reduce the monomer concentration to 40

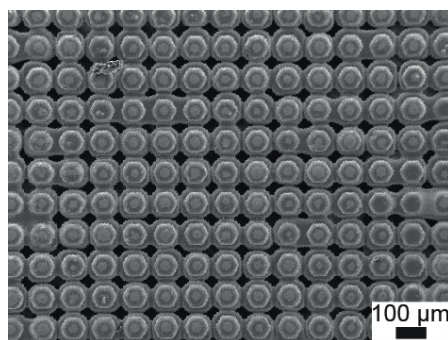


Figure 5.7 – Arrangement of microparticles within granular hydrogel sheets. SEM image of a granular hydrogel sheet composed of spherical particles arranged in a cubic lattice. Drops are assembled using a template containing hexagonal wells that are arranged into a cubic structure. They are polymerized within this template such that their surfaces attain the shape of the wells.

wt%. Indeed, E of these hydrogels is lower than that of hydrogels produced from a monomer concentration of 50 wt%; E of granular sheets is again approximately 50% higher than that of unstructured counterparts, as summarized in Table 5.1. If we further reduce the monomer concentration to 30 wt%, the crosslink density between adjacent particles becomes too low such that no integral films can be obtained any more.

5.2.3 Structure, morphology and composition of hydrogel sheets

Drops spontaneously assemble into the thermodynamically most favorable hexagonal close packed structure, if deposited on a flat substrate, resulting in hexagonal prismatic particles. To test if we can control the drop arrangement and therefore the structure of the resulting granular films, we deposit drops on a PDMS substrate containing 95 μm diameter hexagonal wells. The wells are arranged in a cubic lattice with a distance of 130 μm , which is slightly larger than the drop diameter. After drops are illuminated with UV light, we can detach a connected sheet made of spherical particles that are arranged in a cubic lattice. The bottom surfaces of the particles have adopted the hexagonal shape of the wells that are used to arrange the drops into the cubic structure, as shown in Figure 5.7.

Our results indicate that we can tune the surface morphology of granular hydrogel sheets using templates. However, the use of templates makes the assembly process more time consuming. To test if we can also control the surface topology of these

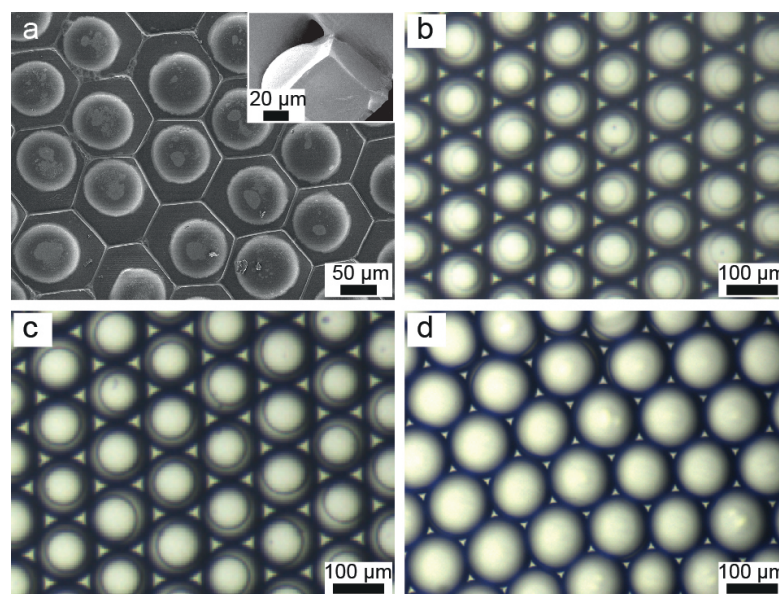


Figure 5.8 – Controlling the surface morphology of granular hydrogel sheets using a two-step polymerization. (a) SEM image of a granular hydrogel sheet composed of hexagonal prismatic particles, each one containing a semi-spherical dome, with a side view of a single particle as inset. (b-d) Optical images of self-assembled drops containing spherical hydrogel particles made by illuminating self-assembled PEG-DA-containing drops with a light source located at a distance of (b) 15 cm, (c) 10 cm, and (d) 4 cm from the sample surface.

hydrogels without the use of templates, we polymerize the hydrogels in two steps: We illuminate the drops with UV light for 3 s immediately after they have been assembled into the hexagonal structure, when they are still spherical. These partially polymerized drops deform into hexagonal prisms after the majority of the oil is evaporated. During this process, we observe the formation of domes at the surface of the deformed drops. When all the drops deformed into hexagonal prisms, we expose them again to UV light for 15 s to fully solidify the drops. Thereby, we obtain 2D sheets composed of hexagonal prismatic particles; each particle contains a semi-spherical dome, as shown in Figure 5.8a. The size of the domes can be tuned with the distance between the UV light source and the sample, as shown in Figures 5.8b-d. These results suggest that a spherical hydrogel particle forms inside the spherical drops when they are illuminated for the first time. As the oil evaporates, drops deform into hexagonal prisms whose height is below the diameter of the growing microparticles such that these particles are trapped in the deformed drops and form domes. The remaining monomers are polymerized when illuminated with UV light for the second time, such that hexagonal prismatic particles with semi-spherical domes result. This two-step polymerization

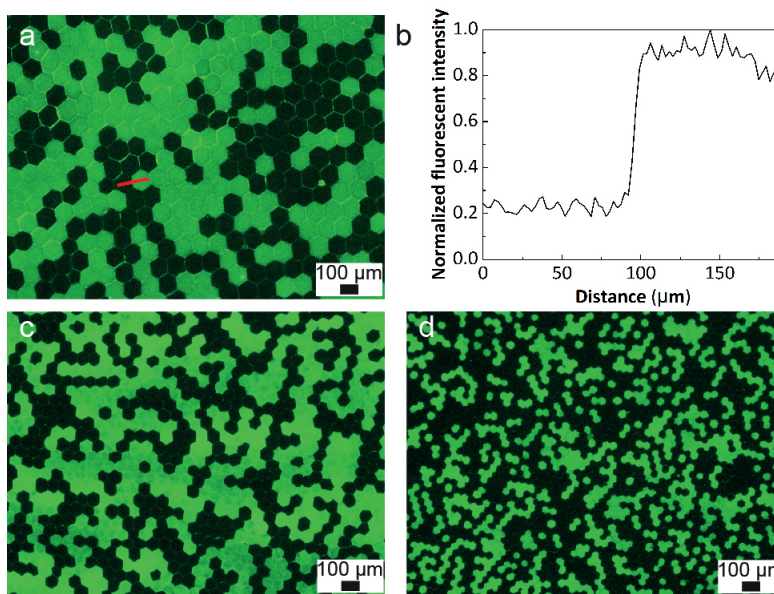


Figure 5.9 – Varying the local composition of granular hydrogel sheets. Fluorescent images of hexagonal prismatic granular hydrogel sheets composed of a mixture of FITC-dextran labeled and label-free particles with an average diameter of (a) 120 μm , (c) 67 μm , and (d) 36 μm . (b) The normalized fluorescent intensity profile measured along the red line in Figure 5.9a.

enables tuning the microscale surface morphology of granular hydrogel sheets without the need for any solid templates.

The main advantage of using drops to build structured granular hydrogel sheets is the ease with which the composition can be varied locally. To exploit this feature, we produce two different batches of drops with identical sizes but different compositions. We add FITC-labeled dextran to one batch of PEG-DA containing drops and produce a second batch of label-free PEG-DA containing drops. The two batches are mixed before drops are assembled on a PDMS substrate and subsequently illuminated with UV light to be converted into granular sheets. The appearance of these sheets closely resembles the skin of cellated lizards,[285] as shown in Figure 5.9a. By analogy to the lizard skin, the composition of these sheets changes over very short length scales, as indicated in Figure 5.9b. The size of the particles can be conveniently varied by controlling the diameter of the drops, as shown in Figures 5.9c-d.

5.3 Conclusion

We demonstrate a new method to fabricate 2D granular hydrogel sheets with locally varying crosslink densities. The sheets are composed of self-assembled hexagonal prismatic particles that are covalently crosslinked through their side walls. The structure and surface morphology of these sheets can be tuned with the size and arrangement of drop templates as well as with the polymerization conditions. The mechanical properties of these granular hydrogels can be controlled by tuning their structure and composition. These granular hydrogel sheets open up new possibilities to design biomimetic soft materials with structures and mechanical properties that closely resemble those of natural ones. This could open up new possibilities to use them as scaffolds for the formation of minerals to fabricate mineral-based composites possessing well-defined structures and properties.

6 Conclusion and Outlook

Many natural CaCO_3 -based materials display superior mechanical properties that are difficult to reproduce with synthetic counterparts. To produce materials with such fascinating properties, nature has established processes that offer a precise control over the formation of CaCO_3 crystals and hence, the local composition and structure of resulting materials. Inspired by these natural materials, a lot of research has been devoted to the fabrication of synthetic CaCO_3 -based materials with similar compositions and structures. However, these synthetic materials typically display inferior mechanical properties. The poor properties are, at least partially, related to the inferior control over the formation of these materials, which is caused by our incomplete understanding of the influence of different variables, such as the processing conditions, soluble additives, and insoluble scaffolds, on different stages of the CaCO_3 formation.

To gain a better understanding of the influence of the formation time on the early stages of the CaCO_3 formation, we employ a new microfluidic spray drying method. This method allows us to quench the formation of ACC with a temporal resolution of hundreds of milliseconds without introducing any organic solvent. Using this method, we reveal that the amount of mobile water contained in ACC particles increases with their formation time and, hence with an increasing particle size. The amount of mobile water contained in these particles influences their kinetic stability if particles are exposed to elevated temperatures or to a focus electron beam. We also demonstrate that the amount of mobile water contained in ACC particles can be reduced if they are functionalized with certain additives, such as PAA. Thereby, these additives increase the kinetic stability of ACC against the temperature-induced crystallization. These results hint at the importance of water in the forma-

Conclusion and Outlook

tion and stability of ACC. Similar to CaCO_3 , many other materials such as calcium phosphate,[286, 287] calcium oxalate,[288, 289], calcium sulfate,[290, 291], titanium oxide,[292, 293] silica,[82, 294, 295], iron oxide[296], and certain proteins[250, 295] form via amorphous precursors. Hence, our results are likely not limited to CaCO_3 but also offer new insights on the role of water in the formation and stability of these amorphous precursors.

To process ACC particles into bulk CaCO_3 -based materials with well-defined properties, it is crucial to understand the influence of amount of mobile water contained in them on their kinetic stability against crystallization under different processing conditions. The amount of mobile water contained in ACC particles can be tuned with soluble additives. To study how this difference in the amount of mobile water contained in ACC influence the humidity- or pressure- induced crystallization of ACC, we synthesize unfunctionalized ACC particles and those functionalized with different additives using a bulk solution method. Therefore, we can produce sufficient quantities of ACC to form bulk samples that we can easily subject to elevated pressures. We monitor the evolution of the structure and degree of hydration of these particles when exposed to a well-defined humid environment or elevated pressures and relate these results to the size, morphology, structure, and orientation of the resulting CaCO_3 crystals. We reveal that the humidity-induced crystallization of ACC follows a distinctly different pathway than the pressure-induced one: The humidity-induced crystallization follows a surface-coupled partial dissolution-reprecipitation, whereas the pressure-induced crystallization undertakes a dehydration-assisted local dissolution-reprecipitation. In both pathways, the amount of water and its mobility that is determined by its interaction strength with additives can significantly influence the crystallization kinetics of ACC and hence, the size, morphology, orientation, and structure of resulting CaCO_3 crystals.

Natural CaCO_3 -based materials are often produced in insoluble soft scaffolds that offer a good control over the local composition and structure of the resulting materials across multiple length scales. Inspired by these soft scaffolds and as a proof-of-concept work, we develop a simple method to fabricate 2D granular hydrogel sheets that mimic the structure and mechanical properties of natural insoluble scaffolds. We produce the granular hydrogel sheets using monomer-filled drop templates that self-assemble into a macroscopic film. We subsequently covalently crosslink the assembled drop templates through a UV-initiated polymerization. The resulting hydrogel sheets are composed of hexagonal prismatic hydrogel microparticles. We

can vary the microscale structure and composition of these hydrogel sheets with the size, composition, and arrangement of individual particles. In addition, we can control the surface morphology of hydrogel sheets with the polymerization conditions. The developed method might offer new opportunities to fabricate structured soft materials that can potentially serve as scaffolds for the formation of CaCO_3 crystals. The influence of size, chemical composition, structures, and mechanical properties of these scaffolds on the formation of CaCO_3 crystals as well as on the mechanical properties of resulting CaCO_3 -based materials remains to be further investigated.

To summarize, this thesis provides new insights in the influence of water, soluble additives, and crystallization conditions on the formation of CaCO_3 crystals that form via ACC precursors. These insights hint at possibilities to more closely control the size, morphology, orientation, and structure of CaCO_3 crystals. Hence, by carefully tuning these parameters as well as rationalizing the size, chemical composition, structure, and mechanical properties of the insoluble scaffold, we might achieve a significant higher level of control over the local composition and structure of synthetic CaCO_3 -based materials, such that their mechanical properties more closely resemble those of natural ones.

Appendix A. Abbreviations

- 2D: two-dimensional
- 3D: three-dimensional
- AA: acrylic acid
- AAS: atomic absorption spectroscopy
- ACC: amorphous CaCO_3
- AFM: atomic force microscopy
- AOT: bis(2-ethylhexyl)sulfosuccinate
- AUC: analytical ultracentrifugation
- Asp: aspartic acid
- CCHH: calcium carbonate hemihydrate
- CIT: citric acid
- CNT: classical nucleation theory
- CP PASS: cross-polarization phase adjusted spinning sideband
- CSA: chemical shift anisotropy
- Cryo-TEM: cryogenic transmission electron microscopy
- DOLLOPS: dynamically ordered liquid-like oxyanion polymers
- DSC: differential scanning calorimetry
- EXAFS: extended X-ray absorption fine structure

Appendix A Abbreviations

- FITC-Dextran: fluorescein isothiocyanate–dextran
- FTIR: Fourier-Transform infrared
- FWHM: full width half-maximum
- Gly: glycine
- LCST: lower critical solution temperature
- MAS: magic angle spinning
- MD: molecular dynamics
- MHC: monohydrocalcite
- Mg-ACC: ACC containing Mg^{2+}
- NMR: nuclear magnetic resonance
- PAA-100K: poly(acrylic acid) with a $M_w \sim 100,000$ Da
- PAA-15K: poly(acrylic acid) with a $M_w \sim 15,000$ Da
- PAA-450K: poly(acrylic acid) with a $M_w \sim 450,000$ Da
- PAA: poly(acrylic acid)
- PAL-15K: poly(allylamine) with a M_w of 15,000 Da
- PAsp: poly(aspartic acid)
- PDF: pair distribution function
- PDMS: poly(dimethyl siloxane)
- PEG700-DA: poly(ethylene glycol) diacrylate with a $M_w \sim 700$ Da
- PILP: polymer-induced liquid precursors
- PNCs: prenucleation clusters
- PSD: power spectral density
- PSS-70K: poly(sodium 4-styrenesulfonate) with a $M_w \sim 70,000$ Da

- PSS: poly(styrene sulfonate)
- PVA: poly(vinyl alcohol)
- RMC: reverse Monte-Carlo
- SAED: select area electron diffraction
- SAXS: small angle X-ray scattering
- TEM: transmission electron microscopy
- TGA: thermogravimetric analysis
- WAXS: wide-angle X-ray scattering
- XANES: X-ray absorption near-edge structure
- XAS: X-ray absorption spectroscopy
- XPS: X-ray photoelectron spectroscopy
- XRD: X-ray diffraction

Appendix B. Symbols

- \bar{d}_{NP} : average diameter of ACC particles
- θ : contact angle of drops on the substrate
- α : degree of crystallization
- χ : molar fraction of Mg^{2+} ions incorporated in Mg-ACC
- ρ_{ACC} : density of ACC
- Δ_G : free energy of ACC with respect to calcite
- Δ_H : enthalpy of ACC with respect to calcite
- ρ_{H_2O} : density of water
- χ_{H_2O} : molar fraction of water contained in ACC
- A : surface area of ACC particles
- CN : average coordination number
- C_b : concentration of ions in bulk solutions
- C_s : saturation concentration of ions with respect to the solubility of ACC
- D_{ion} : diffusion coefficient of ions
- D_v : diffusion coefficient of water vapor
- E : Young's modulus
- E_A : activation energy
- G : free energy

Appendix B Symbols

- $I_{\nu_2-acc,t_{rh}}$: intensity of the ν_2 peak at 863 cm^{-1}
- $I_{\nu_2-cry,t_{rh}}$: intensity of the ν_2 peak at 874 cm^{-1}
- $I_{\nu_4,t_{rh}}$: sum of the intensities of the ν_4 peaks
- M_{ACC} : molar mass of ACC
- N_{NP} : number of ACC particles
- O/Ca : atomic ratio of O to Ca
- P_c : critical pressure for the pressure-induced crystallization
- R : average distance of coordination shells
- RH : relative humidity
- T_{cry} : critical temperature for the temperature-induced crystallization
- V : volume of drops
- $V(t)$: volume of drops at time t
- $c_{Ca^{2+}}$: concentration of Ca^{2+}
- c_{mono} : concentration of monomers
- c_v : concentration of saturated vapor
- d_{NP} : diameter of ACC particles
- d_{cl} : diameter of contact line
- d_{disc} : diameter of discs
- k : spatial frequency
- k_c : crystallization rate coefficient for the humidity-induced crystallization
- l : distance over which the ion concentration gradients exists
- $m(t)$: mass of water at at time t
- n : degree of hydration of ACC, $CaCO_3 \cdot nH_2O$

- q : scattering vector
- r_{cl} : radius of contact line
- $r_{cl}(t)$: radius of contact line at time t
- r_{dis} : dissolution rate of ACC particles
- t_0 : induction time for the humidity-induced crystallization
- t_c : critical time for the pressure-induced crystallization
- $t_{dis-cry}$: critical time required for the crystallization in bulk solutions
- t_{dry} : drying time of drops
- t_{form} : formation time of ACC particles
- t_p : pressing time
- t_{rh} : exposure time in the humid environment

Appendix C. List of Figures

1.1	Examples of natural CaCO_3 -based materials	3
1.2	Schematic illustration of proposed mechanisms of the CaCO_3 formation	5
1.3	Formation of ACC through non-classical routes	7
1.4	Growth of ACC particles in aqueous solutions	9
1.5	Characterizations of the structure of ACC	13
1.6	Hydration of ACC and its influence on the short- and medium- range order of ACC	15
1.7	Solid-state transformation of ACC.	19
1.8	Crystallization of ACC through a dissolution-reprecipitation pathway	22
1.9	Influence of Mg^{2+} on the formation of CaCO_3	24
1.10	Influence of other low molecular weight additives on the formation of CaCO_3	28
1.11	Influence of high molecular weight additives on the formation of CaCO_3	31
1.12	Synergistic effects of multiple types of additives on the formation and composition of ACC	33
1.13	Influence of insoluble organic scaffolds on the formation and composi- tion of ACC	35
2.1	Schematic illustration of the production of ACC nanoparticles using a microfluidic spray dryer	40
2.2	Chemical structures of the additives used to functionalize ACC	46
2.3	Optical image of a section of the microfluidic millipede device in oper- ation	49

2.4	Schematic illustration of the formation of hexagonal prismatic granular hydrogel sheets	50
3.1	Characterization of the morphology and composition of the spray-dried CaCO_3 nanoparticles	56
3.2	Characterization of the structure of the spray-dried CaCO_3 nanoparticles	58
3.3	Influence of the drying time of drops on the size of the spray-dried ACC nanoparticles	59
3.4	Influence of the size of ACC nanoparticles on their morphology	61
3.5	Influence of the size on the morphology of ACC nanoparticles produced by co-spray-drying CaCl_2 and Na_2CO_3	62
3.6	Atomic ratio of O to Ca and the degree of hydration of ACC nanoparticles	63
3.7	Influence of the degree of hydration of ACC particles on their structures	64
3.8	Surface roughness of ACC particles	65
3.9	Influence of the degree of hydration of ACC particles on their morphology	66
3.10	Kinetic stability of ACC particles against the electron beam-induced decomposition	67
3.11	Kinetic stability of ACC particles against the temperature-induced crystallization	69
3.12	Spray-dried PAA-functionalized ACC particles	70
3.13	Schematic illustration of the formation of ACC particles and their transformation into crystals	72
4.1	Kinetic stability of CIT-functionalized ACC particles (CIT: $\text{Ca}^{2+} = 1:10$)	78
4.2	Characterization of the structure of as-synthesized ACC particles . . .	79
4.3	Structural evolution of ACC particles if exposed to a RH around 95% .	81
4.4	Kinetics of the humidity-induced crystallization of ACC particles . . .	83
4.5	Crystallization kinetics of CIT-functionalized ACC particles (CIT: $\text{Ca}^{2+} = 1:30$)	84
4.6	Degrees of hydration of as-synthesized ACC particles	85
4.7	Size of as-synthesized ACC particles	86
4.8	Evolution of n and morphology of ACC particles in a RH around 95% .	87
4.9	Evolution of the morphology of unfunctionalized ACC particles in a RH around 95%	88
4.10	Structure of CaCO_3 crystals after the humidity-induced crystallization	89
4.11	Size, morphology and orientation of CaCO_3 crystals after the humidity-induced crystallization	90

4.12	Kinetics of the pressure-induced crystallization of ACC particles	92
4.13	Comparison of the pressure-induced crystallization kinetics	93
4.14	Evolution of n and morphology of ACC particles at a pressure of 738 MPa.	94
4.15	Crystallization kinetics of unfunctionalized ACC in a RH around 50% .	95
4.16	Kinetic stability of annealed ACC particles functionalized with PSS-70K at a pressure of 738 MPa	96
4.17	Structure of CaCO_3 crystals after the pressure-induced crystallization	98
4.18	Size and morphology of CaCO_3 crystals after the pressure-induced crystallization	99
4.19	Schematic illustration of the crystallization pathways for the humidity- and pressure-induced crystallization	100
4.20	$I_{v_{vat}} / I_{v_{cal}}$ as a function of the exposure time	101
5.1	Production of drop templates and hydrogel particles	108
5.2	Assembly of hydrogel particles in the wet and dry state	109
5.3	Self-assembly process of drops during the evaporation of oil.	110
5.4	Morphology of individual hydrogel particles and granular hydrogel sheets produced on a hydrophilic glass slide	111
5.5	Morphology of granular hydrogel sheets produced on a hydrophobic PDMS substrate	112
5.6	Mechanical properties of hydrogel sheets	113
5.7	Arrangement of microparticles within granular hydrogel sheets.	114
5.8	Controlling the surface morphology of granular hydrogel sheets	115
5.9	Varying the local composition of granular hydrogel sheets.	116

Appendix D. Curriculum Vitae

HUACHUAN DU

PERSONAL INFORMATION

Email	dhcsg88@gmail.com	Date of Birth	April 10, 1992
Phone No.	+41788632696	Nationality	China

EDUCATION

04/2015 - Present	PhD Studies at Institute of Materials in Ecole Polytechnique Fédérale de Lausanne (EPFL), Switzerland
09/2013 - 02/2015	Master Studies at Department of Materials Science and Engineering in EPFL
09/2011 - 06/2012	Exchange Studies at Department of Chemical Engineering in Pohang University of Science and Technology (Postech), South Korea
09/2009 - 07/2013	Bachelor Studies at Department of Polymer Materials and Engineering in Harbin Institute of Technology (HIT), China

SCHOLARSHIP AND AWARDS

SCNAT/SCS Chemistry Travel Award	2019
Best Poster Nominee for MRS Fall Meeting and Best Poster Award for BM09 Symposium	2018
Oversea Exchange Scholarship for HIT Undergraduates	2013
First Prize of National Innovation Experiment Program for Undergraduate	2012
National Scholarship	(Top 1%) 2010
Merit Student of HIT	2010
Individual Scholarship	2010
First Prize Scholarship	2009, 2010, 2011

RESEARCH EXPERTISE

Crystallization, Microfluidics, Hydrogel, Nanocomposite, Materials Characterizations.

RESEARCH AND WORK EXPERIENCE

04/2015-Present	PhD thesis at Soft Materials Laboratory (SMaL) in EPFL, supervised by Prof. Esther Amstad <i>Water: its influence on the formation and crystallization of amorphous calcium carbonate</i> Supervisor for 4 master thesis students, 1 master intern and 6 master semester project students.
10/2014 -02/2015	Master thesis at SMaL in EPFL, supervised by Prof. Esther Amstad <i>Tuning the wettability of surfaces with micro-sized hydrogel particles</i>
7/2013 – 9/2014	Internship in ABB Corporate Research Switzerland, supervised by Dr. Sergey Pancheshnyi <i>Physical modifications of polymer insulators using strong electrical fields</i>
10/2013 – 6/2014	Student research assistant and semester project at Supramolecular Nanomaterials and Interfaces Laboratory in EPFL, supervised by Prof. Francesco Stellacci and Dr. Javier Reguera <i>Co-precipitation of mixtures of oppositely-charged gold nanoparticles with surface nanostructure</i>
12/2011 - 06/2012	Student research assistant at Polymer Surface and Organic Electronics Laboratory in Postech, supervised by Prof. Kilwon Cho and Dr. Hyun Ho Choi <i>Interface engineering of organic thin film transistors with self-assembled monolayer</i>

12/2012 - 06/2013
&
10/2010 - 04/2011

Semester project and bachelor thesis at State Key Laboratory of Urban Water Resource and Environment in HIT, supervised by Prof. Lu Shao

Investigation of photocatalytic properties of TiO₂/Carbon Nanotube nanocomposites fabricated via Sol-Gel method & Surface functionalization of graphene and multi-walled carbon nanotubes

PUBLICATIONS

• Journal Papers

1. Xto, J., Du, H., Borca, C., Amstad, E., van Bokhoven, J., & Huthwelker, T. Salt impurity assisted crystallization of amorphous calcium carbonate in humid environment. *Submitted*
2. Du, H., Courrégelongue, C., Xto, J., Böhlen, A., Steinacher, M., Huthwelker, T., Amstad, E. Additives: Their influence on the humidity- and pressure- induced crystallization of amorphous CaCO₃. *Submitted*
3. Xto, J., Du, H., Borca, C., Amstad, E., van Bokhoven, J., & Huthwelker, T. (2019) Tuning the incorporation of magnesium into calcite during its crystallization from additive-free aqueous solution. *Cryst. Growth Des.*, 19(8), 4385-4394
4. Du, H., Amstad, E. (2019) Water: How does it influence the CaCO₃ formation? *Angew. Chem. Int. Ed.*, In press, 10.1002/anie.201903662
5. Steinacher, M., Du, H., Gilbert, D., & Amstad, E. (2019) Production of additive-free amorphous nanoparticles with SAW-based microfluidic spray-dryer. *Adv. Mater. Technol.*, 4(6), 1800665.
6. Du, H., Steiner, U., & Amstad, E. (2019) Nacre-inspired hard and tough materials. *CHIMIA*, 73(1), 29-34.
7. Du, H., Steinacher, M., Borca, C., Huthwelker, T., Murello, A., Stellacci, F., & Amstad, E. (2018). Amorphous CaCO₃: Influence of the formation time on its degree of hydration and stability. *J. Am. Chem. Soc.*, 140(43), 14289-14299
8. Du, H.[†], Cont, A.[†], Steinacher, M., & Amstad, E. (2018) Fabrication of hexagonal-prismatic granular hydrogel sheets. *Langmuir*, 34(11), 3459-3466. ([†]Equally contributed)
9. Shao, L., Mu, C., Du, H., Czech, Z., Du, H., & Bai, Y. (2011) Covalent marriage of multi-walled carbon nanotubes (MWNTs) and β -cyclodextrin (β -CD) by silicon coupling reagents. *Appl. Surf. Sci.*, 258(5), 1682-1688.

• Conference Papers and Patents

1. Du, H., Pancheshnyi, S., Krivda, A. (2015) Deformation of air and water bubbles in mineral oil under electric field. *22nd International Symposium on Plasma Chemistry, Antwerp, Belgium*
2. Amstad, E., Du, H. (2018) Polymeric structures. WO2019048571/EP2018074059
3. Shao, L., Mu, C., Ding, X., Du, H., Huang, Y. & Bai, Y. (2011) A new method to graft multi-walled carbon nanotubes by β -cyclodextrin. CN201110025742.6

PRESENTATIONS

Oral presentation at Bioinspired Materials Conference, Monte Verita, Switzerland	10/2019
Invited oral presentation at EDMX Research Day, Lausanne, Switzerland	12/2018
Invited oral presentation at MEGA. Seminar (MEchanics GATHERing Seminar Series), Lausanne, Switzerland	05/2018
Oral presentation at 14th International Symposium on Biomineralization, Tsukuba, Japan	10/2017
Invited oral presentation at Frontiers on NanoBioEngineering and Medicine, Lausanne, Switzerland	11/2016
Poster presentation at GRC Supramolecular Chemistry and Self-Assembly over Multiple Scales and Forms, Les Diablerets, Switzerland	05/2019
Poster presentation at MRS fall meeting, Boston, United States	11/2018
Poster presentation at 47th Annual Conference of BACG, Leeds, U.K.	06/2016

Bibliography

- [1] H. Du and E. Amstad, “Water: how does it influence the CaCO_3 formation?,” *Angewandte Chemie International Edition*, May 2019.
- [2] H. Du, U. Steiner, and E. Amstad, “Nacre-inspired hard and tough materials,” *CHIMIA International Journal for Chemistry*, vol. 73, pp. 29–34, Feb. 2019.
- [3] M. Eder, S. Amini, and P. Fratzl, “Biological composites—complex structures for functional diversity,” *Science*, vol. 362, pp. 543–547, Nov. 2018.
- [4] R. O. Ritchie, “The conflicts between strength and toughness,” *Nature Materials*, vol. 10, pp. 817–822, Nov. 2011.
- [5] U. G. K. Wegst, H. Bai, E. Saiz, A. P. Tomsia, and R. O. Ritchie, “Bioinspired structural materials,” *Nature Materials*, vol. 14, pp. 23–36, Jan. 2015.
- [6] F. C. Meldrum, “Calcium carbonate in biomineralisation and biomimetic chemistry,” *International Materials Reviews*, vol. 48, pp. 187–224, June 2003.
- [7] H. Cölfen, “Precipitation of carbonates: recent progress in controlled production of complex shapes,” *Current Opinion in Colloid & Interface Science*, vol. 8, pp. 23–31, Mar. 2003.
- [8] L. B. Gower, “Biomimetic model systems for investigating the amorphous precursor pathway and its role in biomineralization,” *Chemical Reviews*, vol. 108, pp. 4551–4627, Nov. 2008.
- [9] F. C. Meldrum and H. Cölfen, “Controlling mineral morphologies and structures in biological and synthetic systems,” *Chemical Reviews*, vol. 108, pp. 4332–4432, Nov. 2008.
- [10] N. A. J. M. Sommerdijk and G. d. With, “Biomimetic CaCO_3 mineralization using designer molecules and interfaces,” *Chemical Reviews*, vol. 108, pp. 4499–4550, Nov. 2008.
- [11] Z. Zou, W. J. E. M. Habraken, G. Matveeva, A. C. S. Jensen, L. Bertinetti, M. A. Hood, C.-Y. Sun, P. U. P. A. Gilbert, I. Polishchuk, B. Pokroy, J. Mahamid, Y. Politi,

- S. Weiner, P. Werner, S. Bette, R. Dinnebier, U. Kolb, E. Zolotoyabko, and P. Fratzl, "A hydrated crystalline calcium carbonate phase: calcium carbonate hemihydrate," *Science*, vol. 363, pp. 396–400, Jan. 2019.
- [12] C. E. Killian, R. A. Metzler, Y. U. T. Gong, I. C. Olson, J. Aizenberg, Y. Politi, F. H. Wilt, A. Scholl, A. Young, A. Doran, M. Kunz, N. Tamura, S. N. Coppersmith, and P. U. P. A. Gilbert, "Mechanism of calcite co-orientation in the sea urchin tooth," *Journal of the American Chemical Society*, vol. 131, pp. 18404–18409, Dec. 2009.
- [13] L. Addadi, D. Joester, F. Nudelman, and S. Weiner, "Mollusk shell formation: a source of new concepts for understanding biomineralization processes," *Chemistry - A European Journal*, vol. 12, pp. 980–987, Jan. 2006.
- [14] E. Beniash, J. Aizenberg, L. Addadi, and S. Weiner, "Amorphous calcium carbonate transforms into calcite during sea urchin larval spicule growth," *Proceedings of the Royal Society B: Biological Sciences*, vol. 264, pp. 461–465, Mar. 1997.
- [15] Y. Politi, "Sea urchin spine calcite forms via a transient amorphous calcium carbonate phase," *Science*, vol. 306, pp. 1161–1164, Nov. 2004.
- [16] L. Addadi, S. Raz, and S. Weiner, "Taking Advantage of Disorder: Amorphous Calcium Carbonate and Its Roles in Biomineralization," *Advanced Materials*, vol. 15, pp. 959–970, June 2003.
- [17] Y. U. T. Gong, C. E. Killian, I. C. Olson, N. P. Appathurai, A. L. Amasino, M. C. Martin, L. J. Holt, F. H. Wilt, and P. U. P. A. Gilbert, "Phase transitions in biogenic amorphous calcium carbonate," *Proceedings of the National Academy of Sciences*, vol. 109, pp. 6088–6093, Apr. 2012.
- [18] Y. Politi, R. A. Metzler, M. Abrecht, B. Gilbert, F. H. Wilt, I. Sagi, L. Addadi, S. Weiner, and P. U. P. A. Gilbert, "Transformation mechanism of amorphous calcium carbonate into calcite in the sea urchin larval spicule," *Proceedings of the National Academy of Sciences*, vol. 105, pp. 17362–17366, Nov. 2008.
- [19] C. E. Killian, R. A. Metzler, Y. Gong, T. H. Churchill, I. C. Olson, V. Trubetskoy, M. B. Christensen, J. H. Fournelle, F. D. Carlo, S. Cohen, J. Mahamid, A. Scholl, A. Young, A. Doran, F. H. Wilt, S. N. Coppersmith, and P. U. P. A. Gilbert, "Self-sharpening mechanism of the sea urchin tooth," *Advanced Functional Materials*, vol. 21, no. 4, pp. 682–690, 2011.
- [20] A. Sato, S. Nagasaka, K. Furihata, S. Nagata, I. Arai, K. Saruwatari, T. Kogure, S. Sakuda, and H. Nagasawa, "Glycolytic intermediates induce amorphous calcium carbonate formation in crustaceans," *Nature Chemical Biology*, vol. 7, pp. 197–199, Apr. 2011.

- [21] A. Akiva-Tal, S. Kababya, Y. S. Balazs, L. Glazer, A. Berman, A. Sagi, and A. Schmidt, "In situ molecular NMR picture of bioavailable calcium stabilized as amorphous CaCO_3 biomineral in crayfish gastroliths," *Proceedings of the National Academy of Sciences of the United States of America*, vol. 108, pp. 14763–14768, Sept. 2011.
- [22] T. Mass, A. J. Giuffre, C.-Y. Sun, C. A. Stifler, M. J. Frazier, M. Neder, N. Tamura, C. V. Stan, M. A. Marcus, and P. U. P. A. Gilbert, "Amorphous calcium carbonate particles form coral skeletons," *Proceedings of the National Academy of Sciences*, vol. 114, pp. E7670–E7678, Sept. 2017.
- [23] R. T. DeVol, C.-Y. Sun, M. A. Marcus, S. N. Coppersmith, S. C. B. Myneni, and P. U. Gilbert, "Nanoscale transforming mineral phases in fresh nacre," *Journal of the American Chemical Society*, vol. 137, pp. 13325–13333, Oct. 2015.
- [24] H.-B. Yao, J. Ge, L.-B. Mao, Y.-X. Yan, and S.-H. Yu, "25th anniversary article: Artificial carbonate nanocrystals and layered structural nanocomposites inspired by nacre: synthesis, fabrication and applications," *Advanced Materials*, vol. 26, pp. 163–188, Jan. 2014.
- [25] M. Rousseau, E. Lopez, P. Stempflé, M. Brendlé, L. Franke, A. Guette, R. Naslain, and X. Bourrat, "Multiscale structure of sheet nacre," *Biomaterials*, vol. 26, pp. 6254–6262, Nov. 2005.
- [26] X. Li, W.-C. Chang, Y. J. Chao, R. Wang, and M. Chang, "Nanoscale structural and mechanical characterization of a natural nanocomposite material: the shell of red abalone," *Nano Letters*, vol. 4, pp. 613–617, Apr. 2004.
- [27] X. Li, Z.-H. Xu, and R. Wang, "In situ observation of nanograin rotation and deformation in nacre," *Nano Letters*, vol. 6, pp. 2301–2304, Oct. 2006.
- [28] N. Koga, Y. Nakagoe, and H. Tanaka, "Crystallization of amorphous calcium carbonate," *Thermochimica Acta*, vol. 318, pp. 239–244, Sept. 1998.
- [29] P. Bots, L. G. Benning, J.-D. Rodriguez-Blanco, T. Roncal-Herrero, and S. Shaw, "Mechanistic insights into the crystallization of amorphous calcium carbonate (ACC)," *Crystal Growth & Design*, vol. 12, pp. 3806–3814, July 2012.
- [30] D. Pontoni, J. Bolze, N. Dingenouts, T. Narayanan, and M. Ballauff, "Crystallization of calcium carbonate observed *In-situ* by combined small- and wide-angle X-ray scattering," *The Journal of Physical Chemistry B*, vol. 107, pp. 5123–5125, June 2003.
- [31] M. H. Nielsen, S. Aloni, and J. J. D. Yoreo, "*In situ* TEM imaging of CaCO_3 nucleation reveals coexistence of direct and indirect pathways," *Science*, vol. 345,

- pp. 1158–1162, May 2014.
- [32] E. Loste and F. C. Meldrum, “Control of calcium carbonate morphology by transformation of an amorphous precursor in a constrained volume,” *Chemical Communications*, no. 10, pp. 901–902, 2001.
 - [33] E. Loste, R. J. Park, J. Warren, and F. C. Meldrum, “Precipitation of calcium carbonate in confinement,” *Advanced Functional Materials*, vol. 14, pp. 1211–1220, Dec. 2004.
 - [34] Y.-Y. Kim, N. B. J. Hetherington, E. H. Noel, R. Kröger, J. M. Charnock, H. K. Christenson, and F. C. Meldrum, “Capillarity creates single-crystal calcite nanowires from amorphous calcium carbonate,” *Angewandte Chemie International Edition*, vol. 50, pp. 12572–12577, Dec. 2011.
 - [35] O. Grassmann, G. Müller, and P. Löbmann, “Organic-inorganic hybrid structure of calcite crystalline assemblies grown in a gelatin hydrogel matrix: relevance to biomineralization,” *Chemistry of Materials*, vol. 14, pp. 4530–4535, Nov. 2002.
 - [36] O. Grassmann and P. Löbmann, “Biomimetic nucleation and growth of CaCO_3 in hydrogels incorporating carboxylate groups,” *Biomaterials*, vol. 25, pp. 277–282, Jan. 2004.
 - [37] J. R. Dorvee, A. L. Boskey, and L. A. Estroff, “Rediscovering hydrogel-based double-diffusion systems for studying biomineralization,” *CrystEngComm*, vol. 14, no. 18, p. 5681, 2012.
 - [38] Y. Wen, L. Xiang, and Y. Jin, “Synthesis of plate-like calcium carbonate via carbonation route,” *Materials Letters*, vol. 57, pp. 2565–2571, May 2003.
 - [39] K. Wang, Y. J. Wang, G. G. Chen, G. S. Luo, and J. D. Wang, “Enhancement of mixing and mass transfer performance with a microstructure minireactor for controllable preparation of CaCO_3 nanoparticles,” *Industrial & Engineering Chemistry Research*, vol. 46, pp. 6092–6098, Sept. 2007.
 - [40] C. Rodriguez-Navarro, K. Kudłacz, Cizer, and E. Ruiz-Agudo, “Formation of amorphous calcium carbonate and its transformation into mesostructured calcite,” *CrystEngComm*, vol. 17, no. 1, pp. 58–72, 2015.
 - [41] M. G. Page and H. Cölfen, “Improved control of CaCO_3 precipitation by direct carbon dioxide diffusion: application in mesocrystal assembly,” *Crystal Growth & Design*, vol. 6, pp. 1915–1920, Aug. 2006.
 - [42] J. Ihli, P. Bots, A. Kulak, L. G. Benning, and F. C. Meldrum, “Elucidating mechanisms of diffusion-based calcium carbonate synthesis leads to controlled mesocrystal formation,” *Advanced Functional Materials*, vol. 23, pp. 1965–1973,

Apr. 2013.

- [43] P. J. M. Smeets, K. R. Cho, R. G. E. Kempen, N. A. J. M. Sommerdijk, and J. J. De Yoreo, "Calcium carbonate nucleation driven by ion binding in a biomimetic matrix revealed by in situ electron microscopy," *Nature Materials*, vol. 14, pp. 394–399, Apr. 2015.
- [44] L. B. Gower and D. J. Odom, "Deposition of calcium carbonate films by a polymer-induced liquid-precursor (PILP) process," *Journal of Crystal Growth*, vol. 210, no. 4, pp. 719–734, 2000.
- [45] Y. Kitano, K. Park, and D. W. Hood, "Pure aragonite synthesis," *Journal of Geophysical Research*, vol. 67, no. 12, pp. 4873–4874, 1962.
- [46] S. E. Wolf, J. Leiterer, M. Kappl, F. Emmerling, and W. Tremel, "Early homogeneous amorphous precursor stages of calcium carbonate and subsequent crystal growth in levitated droplets," *Journal of the American Chemical Society*, vol. 130, pp. 12342–12347, Sept. 2008.
- [47] J. Rudloff and H. Cölfen, "Superstructures of temporarily stabilized nanocrystalline CaCO_3 particles: morphological control via water surface tension variation," *Langmuir*, vol. 20, pp. 991–996, Feb. 2004.
- [48] E. M. Pouget, P. H. H. Bomans, J. A. C. M. Goos, P. M. Frederik, G. de With, and N. A. J. M. Sommerdijk, "The initial stages of template-controlled CaCO_3 formation revealed by Cryo-TEM," *Science*, vol. 323, pp. 1455–1458, Mar. 2009.
- [49] K. J. Davis, "The role of Mg^{2+} as an impurity in calcite growth," *Science*, vol. 290, pp. 1134–1137, Nov. 2000.
- [50] A. E. Stephenson, J. J. DeYoreo, L. Wu, K. J. Wu, J. Hoyer, and P. M. Dove, "Peptides enhance magnesium signature in calcite: insights into origins of vital effects," *Science*, vol. 322, pp. 724–727, Oct. 2008.
- [51] Q. Hu, M. H. Nielsen, C. L. Freeman, L. M. Hamm, J. Tao, J. R. I. Lee, T. Y. J. Han, U. Becker, J. H. Harding, P. M. Dove, and J. J. D. Yoreo, "The thermodynamics of calcite nucleation at organic interfaces: Classical vs. non-classical pathways," *Faraday Discussions*, vol. 159, pp. 509–523, Mar. 2013.
- [52] Y.-W. Wang, Y.-Y. Kim, C. J. Stephens, F. C. Meldrum, and H. K. Christenson, "In situ study of the precipitation and crystallization of amorphous calcium carbonate (ACC)," *Crystal Growth & Design*, vol. 12, pp. 1212–1217, Mar. 2012.
- [53] J. Rieger, J. Thieme, and C. Schmidt, "Study of precipitation reactions by X-ray microscopy: CaCO_3 precipitation and the effect of polycarboxylates," *Langmuir*, vol. 16, pp. 8300–8305, Oct. 2000.

- [54] J. D. Rodriguez-Blanco, S. Shaw, and L. G. Benning, "The kinetics and mechanisms of amorphous calcium carbonate (ACC) crystallization to calcite, viavaterite.," *Nanoscale*, vol. 3, no. 1, pp. 265–271, 2011.
- [55] J. R. Clarkson, T. J. Price, and C. J. Adams, "Role of metastable phases in the spontaneous precipitation of calcium carbonate," *Journal of the Chemical Society, Faraday Transactions*, vol. 88, pp. 243–249, Jan. 1992.
- [56] D. Gebauer, M. Kellermeier, J. D. Gale, L. Bergström, and H. Cölfen, "Pre-nucleation clusters as solute precursors in crystallisation," *Chem. Soc. Rev.*, vol. 43, no. 7, pp. 2348–2371, 2014.
- [57] P. J. M. Smeets, A. R. Finney, W. J. E. M. Habraken, F. Nudelman, H. Friedrich, J. Laven, J. J. De Yoreo, P. M. Rodger, and N. A. J. M. Sommerdijk, "A classical view on nonclassical nucleation," *Proceedings of the National Academy of Sciences*, vol. 114, pp. E7882–E7890, Sept. 2017.
- [58] J. Rieger, M. Kellermeier, and L. Nicoleau, "Formation of nanoparticles and nanostructures-an industrial perspective on CaCO₃, cement, and polymers," *Angewandte Chemie International Edition*, vol. 53, pp. 12380–12396, Aug. 2014.
- [59] J. J. De Yoreo, P. U. P. A. Gilbert, N. A. J. M. Sommerdijk, R. L. Penn, S. Whitlam, D. Joester, H. Zhang, J. D. Rimer, A. Navrotsky, J. F. Banfield, A. F. Wallace, F. M. Michel, F. C. Meldrum, H. Colfen, and P. M. Dove, "Crystallization by particle attachment in synthetic, biogenic, and geologic environments," *Science*, vol. 349, pp. aaa6760–aaa6760, July 2015.
- [60] D. Gebauer, A. Völkel, and H. Cölfen, "Stable prenucleation calcium carbonate clusters," *Science*, vol. 322, pp. 1819–1822, Dec. 2008.
- [61] J. Rieger, T. Frechen, G. Cox, W. Heckmann, C. Schmidt, and J. Thieme, "Precursor structures in the crystallization/precipitation processes of CaCO₃ and control of particle formation by polyelectrolytes," *Faraday Discussions*, vol. 136, p. 265, 2007.
- [62] A. F. Wallace, L. O. Hedges, A. Fernandez-Martinez, P. Raiteri, J. D. Gale, G. A. Waychunas, S. Whitlam, J. F. Banfield, and J. J. De Yoreo, "Microscopic evidence for liquid-liquid separation in supersaturated CaCO₃ solutions," *Science*, vol. 341, pp. 885–889, Aug. 2013.
- [63] A. S. A. Mohammed, A. Carino, A. Testino, M. R. Andalibi, and A. Cervellino, "In-situ liquid SAXS studies on the early stage of amorphous calcium carbonate (ACC) formation," *arXiv:1810.11696 [cond-mat]*, Oct. 2018. arXiv: 1810.11696.
- [64] Y. Chao, O. Horner, P. Vallée, F. Meneau, O. Alos-Ramos, F. Hui, M. Turmine,

- H. Perrot, and J. Lédion, “*In situ* probing calcium carbonate formation by combining fast controlled precipitation method and small-angle X-ray scattering,” *Langmuir*, vol. 30, pp. 3303–3309, Apr. 2014.
- [65] R. Demichelis, P. Raiteri, J. D. Gale, D. Quigley, and D. Gebauer, “Stable prenucleation mineral clusters are liquid-like ionic polymers,” *Nature Communications*, vol. 2, p. 590, Sept. 2011.
- [66] M. Kellermeier, P. Raiteri, J. K. Berg, A. Kempter, J. D. Gale, and D. Gebauer, “Entropy drives calcium carbonate ion association,” *ChemPhysChem*, vol. 17, pp. 3535–3541, Nov. 2016.
- [67] K. Henzler, E. O. Fetisov, M. Galib, M. D. Baer, B. A. Legg, C. Borca, J. M. Xto, S. Pin, J. L. Fulton, G. K. Schenter, N. Govind, J. I. Siepmann, C. J. Mundy, T. Huthwelker, and J. J. De Yoreo, “Supersaturated calcium carbonate solutions are classical,” *Science Advances*, vol. 4, p. eaao6283, Jan. 2018.
- [68] A. Carino, A. Testino, M. R. Andalibi, F. Pilger, P. Bowen, and C. Ludwig, “Thermodynamic-kinetic precipitation modeling. a case study: the amorphous calcium carbonate (ACC) precipitation pathway unravelled,” *Crystal Growth & Design*, vol. 17, pp. 2006–2015, Apr. 2017.
- [69] A. Verch, I. E. Morrison, R. v. d. Loch, and R. Kröger, “*In situ* electron microscopy studies of calcium carbonate precipitation from aqueous solution with and without organic additives,” *Journal of Structural Biology*, vol. 183, pp. 270–277, Aug. 2013.
- [70] M. Faatz, F. Gröhn, and G. Wegner, “Amorphous calcium carbonate: synthesis and potential intermediate in biomineralization,” *Advanced Materials*, vol. 16, no. 12, pp. 996–1000, 2004.
- [71] F. Sebastiani, S. L. P. Wolf, B. Born, T. Q. Luong, H. Cölfen, D. Gebauer, and M. Havenith, “Water dynamics from THz spectroscopy reveal the locus of a liquid-liquid binodal limit in aqueous CaCO_3 solutions,” *Angewandte Chemie International Edition*, vol. 56, pp. 490–495, Jan. 2017.
- [72] X. Cheng, P. L. Varona, M. J. Olszta, and L. B. Gower, “Biomimetic synthesis of calcite films by a polymer-induced liquid-precursor (PILP) process,” *Journal of Crystal Growth*, vol. 307, pp. 395–404, Sept. 2007.
- [73] M. A. Bewernitz, D. Gebauer, J. Long, H. Cölfen, and L. B. Gower, “A metastable liquid precursor phase of calcium carbonate and its interactions with polyaspartate,” *Faraday Discussions*, vol. 159, p. 291, 2012.
- [74] S. E. Wolf, J. Leiterer, V. Pipich, R. Barrea, F. Emmerling, and W. Tremel, “Strong

- stabilization of amorphous calcium carbonate emulsion by ovalbumin: gaining insight into the mechanism of 'Polymer-Induced Liquid Precursor' processes," *Journal of the American Chemical Society*, vol. 133, no. 32, pp. 12642–12649, 2011.
- [75] Y. Xu, K. C. H. Tijssen, P. H. H. Bomans, A. Akiva, H. Friedrich, A. P. M. Kentgens, and N. A. J. M. Sommerdijk, "Microscopic structure of the polymer-induced liquid precursor for calcium carbonate," *Nature Communications*, vol. 9, p. 2582, Dec. 2018.
- [76] F. M. Michel, J. MacDonald, J. Feng, B. L. Phillips, L. Ehm, C. Tarabrella, J. B. Parise, and R. J. Reeder, "Structural characteristics of synthetic amorphous calcium carbonate," *Chemistry of Materials*, vol. 20, pp. 4720–4728, July 2008.
- [77] J. Ihli, W. C. Wong, E. H. Noel, Y.-Y. Kim, A. N. Kulak, H. K. Christenson, M. J. Duer, and F. C. Meldrum, "Dehydration and crystallization of amorphous calcium carbonate in solution and in air," *Nature Communications*, vol. 5, p. 3169, Dec. 2014.
- [78] J. Liu, J. Rieger, and K. Huber, "Analysis of the nucleation and growth of amorphous CaCO_3 by means of time-resolved static light scattering," *Langmuir*, vol. 24, pp. 8262–8271, Aug. 2008.
- [79] D. Quigley and P. M. Rodger, "Free energy and structure of calcium carbonate nanoparticles during early stages of crystallization," *Journal of Chemical Physics*, vol. 128, no. 22, p. 221101, 2008.
- [80] P. Raiteri and J. D. Gale, "Water is the key to nonclassical nucleation of amorphous calcium carbonate," *Journal of the American Chemical Society*, vol. 132, pp. 17623–17634, Dec. 2010.
- [81] Z. Zou, L. Bertinetti, Y. Politi, A. C. S. Jensen, S. Weiner, L. Addadi, P. Fratzl, and W. J. E. M. Habraken, "Opposite particle size effect on amorphous calcium carbonate crystallization in water and during heating in air," *Chemistry of Materials*, vol. 27, pp. 4237–4246, June 2015.
- [82] A. Navrotsky, "Energetic clues to pathways to biomineralization: precursors, clusters, and nanoparticles," *Proceedings of the National Academy of Sciences*, vol. 101, pp. 12096–12101, Aug. 2004.
- [83] G. A. Tribello, F. Bruneval, C. Liew, and M. Parrinello, "A molecular dynamics study of the early stages of calcium carbonate growth," *The Journal of Physical Chemistry B*, vol. 113, pp. 11680–11687, Aug. 2009.
- [84] J. Bolze, D. Pontoni, M. Ballauff, T. Narayanan, and H. Cölfen, "Time-resolved

- SAXS study of the effect of a double hydrophilic block-copolymer on the formation of CaCO_3 from a supersaturated salt solution,” *Journal of Colloid and Interface Science*, vol. 277, pp. 84–94, Sept. 2004.
- [85] J. Bolze, B. Peng, N. Dingenouts, P. Panine, T. Narayanan, and M. Ballauff, “Formation and growth of amorphous colloidal CaCO_3 precursor particles as detected by time-resolved SAXS,” *Langmuir*, vol. 18, pp. 8364–8369, Oct. 2002.
- [86] M. Albéric, L. Bertinetti, Z. Zou, P. Fratzl, W. Habraken, and Y. Politi, “The crystallization of amorphous calcium carbonate is kinetically governed by ion impurities and water,” *Advanced Science*, vol. 5, p. 1701000, May 2018.
- [87] A. V. Radha, T. Z. Forbes, C. E. Killian, P. U. P. A. Gilbert, and A. Navrotsky, “Transformation and crystallization energetics of synthetic and biogenic amorphous calcium carbonate,” *Proceedings of the National Academy of Sciences*, vol. 107, pp. 16438–16443, Sept. 2010.
- [88] G. Wolf and C. Günther, “Thermophysical investigations of the polymorphous phases of calcium carbonate,” *Journal of Thermal Analysis and Calorimetry*, no. 65, pp. 687–698, 2001.
- [89] V. Pipich, M. Balz, S. E. Wolf, W. Tremel, and D. Schwahn, “Nucleation and growth of CaCO_3 mediated by the eg-white protein ovalbumin: a time-resolved *in situ* study using small-angle neutron scattering,” *Journal of the American Chemical Society*, vol. 130, pp. 6879–6892, May 2008.
- [90] M. Farhadi Khouzani, D. M. Chevrier, P. Güttlein, K. Hauser, P. Zhang, N. Hedin, and D. Gebauer, “Disordered amorphous calcium carbonate from direct precipitation,” *CrystEngComm*, vol. 17, no. 26, pp. 4842–4849, 2015.
- [91] C. C. Tester, R. E. Brock, C.-H. Wu, M. R. Krejci, S. Weigand, and D. Joester, “In vitro synthesis and stabilization of amorphous calcium carbonate (ACC) nanoparticles within liposomes,” *CrystEngComm*, vol. 13, pp. 3975–3978, May 2011.
- [92] D. Gebauer, P. N. Gunawidjaja, J. Y. P. Ko, Z. Bacsik, B. Aziz, L. Liu, Y. Hu, L. Bergström, C.-W. Tai, T.-K. Sham, M. Edén, and N. Hedin, “Proto-calcite and proto-vaterite in amorphous calcium carbonates,” *Angewandte Chemie International Edition*, vol. 49, pp. 8889–8891, Nov. 2010.
- [93] M. Farhadi-Khouzani, D. M. Chevrier, P. Zhang, N. Hedin, and D. Gebauer, “Water as the key to proto-aragonite amorphous CaCO_3 ,” *Angewandte Chemie International Edition*, vol. 55, pp. 8117–8120, July 2016.
- [94] D. J. Tobler, J. D. Rodriguez Blanco, H. O. Sørensen, S. L. S. Stipp, and K. Diderik-

- sen, "Effect of pH on amorphous calcium carbonate structure and transformation," *Crystal Growth & Design*, vol. 16, pp. 4500–4508, Aug. 2016.
- [95] J. H. E. Cartwright, A. G. Checa, J. D. Gale, D. Gebauer, and C. I. Sainz-Díaz, "Calcium carbonate polyamorphism and its role in biomineralization: How many amorphous calcium carbonates are there?," *Angewandte Chemie International Edition*, vol. 51, pp. 11960–11970, Nov. 2012.
- [96] A. L. Goodwin, F. M. Michel, B. L. Phillips, D. A. Keen, M. T. Dove, and R. J. Reeder, "Nanoporous structure and medium-range order in synthetic amorphous calcium carbonate," *Chemistry of Materials*, vol. 22, pp. 3197–3205, May 2010.
- [97] C. J. Stephens, S. F. Ladden, F. C. Meldrum, and H. K. Christenson, "Amorphous calcium carbonate is stabilized in confinement," *Advanced Functional Materials*, vol. 20, pp. 2108–2115, June 2010.
- [98] S. Weiner, Y. Levi-Kalishman, S. Raz, and L. Addadi, "Biologically formed amorphous calcium carbonate," *Connective Tissue Research*, vol. 44, pp. 214–218, Jan. 2003.
- [99] S. Gunasekaran, G. Anbalagan, and S. Pandi, "Raman and infrared spectra of carbonates of calcite structure," *Journal of Raman Spectroscopy*, vol. 37, no. 9, pp. 892–899, 2006.
- [100] H. Nebel, M. Neumann, C. Mayer, and M. Epple, "On the structure of amorphous calcium carbonate: a detailed study by solid-state NMR spectroscopy," *Inorganic Chemistry*, vol. 47, pp. 7874–7879, Sept. 2008.
- [101] S. Sun, D. M. Chevrier, P. Zhang, D. Gebauer, and H. Cölfen, "Distinct short-range order is inherent to small amorphous calcium carbonate clusters(<2 nm)," *Angewandte Chemie International Edition*, vol. 55, pp. 12206–12209, Sept. 2016.
- [102] I. Ben Shir, S. Kababya, I. Katz, B. Pokroy, and A. Schmidt, "Exposed and buried biomineral interfaces in the aragonitic shell of *Perna canaliculus* revealed by solid-state NMR," *Chemistry of Materials*, vol. 25, pp. 4595–4602, Nov. 2013.
- [103] S. Sen, D. C. Kaseman, B. Colas, D. E. Jacob, and S. M. Clark, "Hydrogen bonding induced distortion of CO₃ units and kinetic stabilization of amorphous calcium carbonate: results from 2D ¹³C NMR spectroscopy," *Physical Chemistry Chemical Physics*, vol. 18, no. 30, pp. 20330–20337, 2016.
- [104] A. Becker, U. Bismayer, M. Epple, H. Fabritius, B. Hasse, J. Shi, and A. Ziegler, "Structural characterisation of X-ray amorphous calcium carbonate (ACC) in sternal deposits of the crustacea *Porcellio scaber*," *Dalton Transactions*, vol. 0,

- pp. 551–555, Feb. 2003.
- [105] Y. Levi-Kalisman, S. Raz, S. Weiner, L. Addadi, and I. Sagi, “Structural differences between biogenic amorphous calcium carbonate phases using X-ray absorption spectroscopy,” *Advanced Functional Materials*, vol. 12, p. 43, Jan. 2002.
- [106] R. S. K. Lam, J. M. Charnock, A. Lennie, and F. C. Meldrum, “Synthesis-dependant structural variations in amorphous calcium carbonate,” *CrystEngComm*, vol. 9, no. 12, p. 1226, 2007.
- [107] C. Günther, A. Becker, G. Wolf, and M. Eppele, “In vitro synthesis and structural characterization of amorphous calcium carbonate,” *Zeitschrift für anorganische und allgemeine Chemie*, vol. 631, no. 13-14, pp. 2830–2835, 2005.
- [108] M. P. Schmidt, A. J. Illott, B. L. Phillips, and R. J. Reeder, “Structural changes upon dehydration of amorphous calcium carbonate,” *Crystal Growth & Design*, vol. 14, pp. 938–951, Mar. 2014.
- [109] J. W. Singer, A. Yazaydin, R. J. Kirkpatrick, and G. M. Bowers, “Structure and transformation of amorphous calcium carbonate: a solid-state ^{43}Ca NMR and computational molecular dynamics investigation,” *Chemistry of Materials*, vol. 24, pp. 1828–1836, May 2012.
- [110] R. Innocenti Malini, Y. G. Bushuev, S. A. Hall, C. L. Freeman, P. M. Rodger, and J. H. Harding, “Using simulation to understand the structure and properties of hydrated amorphous calcium carbonate,” *CrystEngComm*, vol. 18, no. 1, pp. 92–101, 2016.
- [111] G. Cobourne, G. Mountjoy, J. D. Rodriguez-Blanco, L. G. Benning, A. C. Hannon, and J. R. Plaisier, “Neutron and X-ray diffraction and empirical potential structure refinement modelling of magnesium stabilised amorphous calcium carbonate,” *Journal of Non-Crystalline Solids*, vol. 401, pp. 154–158, Oct. 2014.
- [112] A. C. Jensen, S. Imberti, S. F. Parker, E. Schneck, Y. Politi, P. Fratzl, L. Bertinetti, and W. J. Habraken, “Hydrogen bonding in amorphous calcium carbonate and molecular reorientation induced by dehydration,” *Journal of Physical Chemistry C*, vol. 122, no. 6, pp. 3591–3598, 2018.
- [113] A. Fernandez-Martinez, Y. Hu, B. Lee, Y.-S. Jun, and G. A. Waychunas, “*In Situ* determination of interfacial energies between heterogeneously nucleated CaCO_3 and quartz substrates: thermodynamics of CO_2 mineral trapping,” *Environmental Science & Technology*, vol. 47, pp. 102–109, Jan. 2013.
- [114] M. Saharay, A. O. Yazaydin, and R. J. Kirkpatrick, “Dehydration-induced amorphous phases of calcium carbonate,” *Journal of Physical Chemistry B*, vol. 117,

- no. 12, pp. 3328–3336, 2013.
- [115] M. Saharay and R. James Kirkpatrick, “Onset of orientational order in amorphous calcium carbonate (ACC) upon dehydration,” *Chemical Physics Letters*, vol. 591, pp. 287–291, Jan. 2014.
- [116] H. Tomono, H. Nada, F. Zhu, T. Sakamoto, T. Nishimura, and T. Kato, “Effects of magnesium ions and water molecules on the structure of amorphous calcium carbonate: a molecular dynamics study,” *The Journal of Physical Chemistry B*, vol. 117, pp. 14849–14856, Nov. 2013.
- [117] J. Ihli, A. N. Kulak, and F. C. Meldrum, “Freeze-drying yields stable and pure amorphous calcium carbonate (ACC),” *Chemical Communications*, vol. 49, no. 30, p. 3134, 2013.
- [118] Y. G. Bushuev, A. R. Finney, and P. M. Rodger, “Stability and structure of hydrated amorphous calcium carbonate,” *Crystal Growth & Design*, vol. 15, pp. 5269–5279, Nov. 2015.
- [119] M. Saharay and R. J. Kirkpatrick, “Water dynamics in hydrated amorphous materials: a molecular dynamics study of the effects of dehydration in amorphous calcium carbonate,” *Physical Chemistry Chemical Physics*, vol. 19, no. 43, pp. 29594–29600, 2017.
- [120] N. Koga and Y. Yamane, “Thermal behaviors of amorphous calcium carbonates prepared in aqueous and ethanol media,” *Journal of Thermal Analysis and Calorimetry*, vol. 94, pp. 379–387, Nov. 2008.
- [121] X. Xu, J. T. Han, D. H. Kim, and K. Cho, “Two modes of transformation of amorphous calcium carbonate films in air,” *The Journal of Physical Chemistry B*, vol. 110, pp. 2764–2770, Feb. 2006.
- [122] J. Ihli, Y.-Y. Kim, E. H. Noel, and F. C. Meldrum, “The effect of additives on amorphous calcium carbonate (ACC): Janus behavior in solution and the solid state,” *Advanced Functional Materials*, vol. 23, pp. 1575–1585, Mar. 2013.
- [123] F. Konrad, F. Gallien, D. E. Gerard, and M. Dietzel, “Transformation of amorphous calcium carbonate in air,” *Crystal Growth & Design*, vol. 16, pp. 6310–6317, Nov. 2016.
- [124] A. Fernandez-Martinez, B. Kalkan, S. M. Clark, and G. A. Waychunas, “Pressure-induced polyamorphism and formation of ‘aragonitic’ amorphous calcium carbonate,” *Angewandte Chemie International Edition*, vol. 52, pp. 8354–8357, Aug. 2013.
- [125] E. M. Pouget, P. H. H. Bomans, A. Dey, P. M. Frederik, G. de With, and N. A.

- J. M. Sommerdijk, "The development of morphology and structure in hexagonal vaterite," *Journal of the American Chemical Society*, vol. 132, pp. 11560–11565, Aug. 2010.
- [126] F. Nudelman, E. Sonmezler, P. H. H. Bomans, G. de With, and N. A. J. M. Sommerdijk, "Stabilization of amorphous calcium carbonate by controlling its particle size," *Nanoscale*, vol. 2, no. 11, p. 2436, 2010.
- [127] E. H. Noel, Y.-Y. Kim, J. M. Charnock, and F. C. Meldrum, "Solid state crystallization of amorphous calcium carbonate nanoparticles leads to polymorph selectivity," *CrystEngComm*, vol. 15, no. 4, pp. 697–705, 2013.
- [128] S. Kababya, A. Gal, K. Kahil, S. Weiner, L. Addadi, and A. Schmidt, "Phosphate–water interplay tunes amorphous calcium carbonate metastability: spontaneous phase separation and crystallization vs stabilization viewed by solid state NMR," *Journal of the American Chemical Society*, vol. 137, pp. 990–998, Jan. 2015.
- [129] T. Yoshino, K. Maruyama, H. Kagi, M. Nara, and J. C. Kim, "Pressure-induced crystallization from amorphous calcium carbonate," *Crystal Growth & Design*, vol. 12, pp. 3357–3361, July 2012.
- [130] K. Maruyama, H. Kagi, T. Inoue, H. Ohfuji, and T. Yoshino, "*In situ* observation of pressure-induced crystallization from amorphous calcium carbonate by time-resolved X-ray diffraction," *Chemistry Letters*, vol. 44, no. 4, pp. 434–436, 2015.
- [131] Y.-C. Huang, M. B. Gindele, J. Knaus, A. Rao, and D. Gebauer, "On mechanisms of mesocrystal formation: magnesium ions and water environments regulate the crystallization of amorphous minerals," *CrystEngComm*, vol. 20, no. 31, pp. 4395–4405, 2018.
- [132] J. M. Xto, C. N. Borca, J. A. van Bokhoven, and T. Huthwelker, "Aerosol-based synthesis of pure and stable amorphous calcium carbonate," *Chemical Communications*, vol. 55, no. 72, pp. 10725–10728, 2019.
- [133] A. Gal, W. Habraken, D. Gur, P. Fratzl, S. Weiner, and L. Addadi, "Calcite crystal growth by a solid-state transformation of stabilized amorphous calcium carbonate nanospheres in a hydrogel," *Angewandte Chemie International Edition*, vol. 52, pp. 4867–4870, Apr. 2013.
- [134] A. Gal, K. Kahil, N. Vidavsky, R. T. DeVos, P. U. P. A. Gilbert, P. Fratzl, S. Weiner, and L. Addadi, "Particle accretion mechanism underlies biological crystal growth from an amorphous precursor phase," *Advanced Functional Materials*, vol. 24,

- no. 34, pp. 5420–5426, 2014.
- [135] A. J. Giuffre, A. C. Gagnon, J. J. De Yoreo, and P. M. Dove, “Isotopic tracer evidence for the amorphous calcium carbonate to calcite transformation by dissolution–reprecipitation,” *Geochimica et Cosmochimica Acta*, vol. 165, pp. 407–417, Sept. 2015.
- [136] A. A. Noyes and W. R. Whitney, “The rate of solution of solid substances in their own solutions,” *Journal of the American Chemical Society*, vol. 19, pp. 930–934, Dec. 1897.
- [137] J. Rodriguez-Blanco, S. Shaw, P. Bots, T. Roncal-Herrero, and L. Benning, “The role of pH and Mg on the stability and crystallization of amorphous calcium carbonate,” *Journal of Alloys and Compounds*, vol. 536, pp. S477–S479, Sept. 2012.
- [138] X. R. Xu, A. H. Cai, R. Liu, H. H. Pan, R. K. Tang, and K. Cho, “The roles of water and polyelectrolytes in the phase transformation of amorphous calcium carbonate,” *Journal of Crystal Growth*, vol. 310, no. 16, pp. 3779–3787, 2008.
- [139] S.-F. Chen, H. Cölfen, M. Antonietti, and S.-H. Yu, “Ethanol assisted synthesis of pure and stable amorphous calcium carbonate nanoparticles,” *Chemical Communications*, vol. 49, no. 83, p. 9564, 2013.
- [140] M. L. Dundon and E. Mack, “The solubility and surface energy of calcium sulfate,” *Journal of the American Chemical Society*, vol. 45, pp. 2479–2485, Nov. 1923.
- [141] Y. Kojima, A. Kawanobe, T. Yasue, and Y. Arai, “Synthesis of amorphous calcium carbonate and its crystallization,” *Journal of the Ceramic Society of Japan*, vol. 101, pp. 1145–1152, Oct. 1993.
- [142] H. Cölfen and S. Mann, “Higher-order organization by mesoscale self-assembly and transformation of hybrid nanostructures,” *Angewandte Chemie International Edition*, vol. 42, pp. 2350–2365, May 2003.
- [143] D. Gebauer, H. Cölfen, A. Verch, and M. Antonietti, “The multiple roles of additives in CaCO_3 crystallization: a quantitative case study,” *Advanced Materials*, vol. 21, pp. 435–439, Jan. 2009.
- [144] D. Gebauer, “How can additives control the early stages of mineralisation?,” *Minerals*, vol. 8, no. 5, p. 179, 2018.
- [145] A. Verch, D. Gebauer, M. Antonietti, and H. Cölfen, “How to control the scaling of CaCO_3 : a “fingerprinting technique” to classify additives,” *Physical Chemistry Chemical Physics*, vol. 13, no. 37, p. 16811, 2011.

- [146] J. Aizenberg, L. Addadi, S. Weiner, and G. Lambert, "Stabilization of amorphous calcium carbonate by specialized macromolecules in biological and synthetic precipitates," *Advanced Materials*, vol. 8, no. 3, pp. 222–226, 1996.
- [147] F. Nudelman and N. A. J. M. Sommerdijk, "Biom mineralization as an inspiration for materials chemistry," *Angewandte Chemie International Edition*, vol. 51, pp. 6582–6596, July 2012.
- [148] A.-W. Xu, Y. Ma, and H. Cölfen, "Biomimetic mineralization," *Journal of Materials Chemistry*, vol. 17, pp. 415–449, Jan. 2007.
- [149] M. Zeng, Y.-Y. Kim, C. Anduix-Canto, C. Frontera, D. Laundy, N. Kapur, H. K. Christenson, and F. C. Meldrum, "Confinement generates single-crystal aragonite rods at room temperature," *Proceedings of the National Academy of Sciences*, vol. 115, pp. 7670–7675, July 2018.
- [150] Y.-Y. Kim, J. D. Carloni, B. Demarchi, D. Sparks, D. G. Reid, M. Kunitake, C. C. Tang, M. J. Duer, C. L. Freeman, B. Pokroy, K. Penkman, J. H. Harding, L. A. Estroff, S. P. Baker, and F. C. Meldrum, "Tuning hardness in calcite by incorporation of amino acids," *Nature Materials*, vol. 15, pp. 903–910, Aug. 2016.
- [151] L.-B. Mao, H.-L. Gao, H.-B. Yao, L. Liu, H. Colfen, G. Liu, S.-M. Chen, S.-K. Li, Y.-X. Yan, Y.-Y. Liu, and S.-H. Yu, "Synthetic nacre by predesigned matrix-directed mineralization," *Science*, vol. 354, pp. 107–110, Oct. 2016.
- [152] J. Aizenberg, D. A. Muller, J. L. Grazul, and D. R. Hamann, "Direct fabrication of large micropatterned single crystals," *Science*, vol. 299, pp. 1205–1208, Feb. 2003.
- [153] B. Cantaert, D. Kuo, S. Matsumura, T. Nishimura, T. Sakamoto, and T. Kato, "Use of amorphous calcium carbonate for the design of new materials," *ChemPlusChem*, vol. 82, pp. 107–120, Jan. 2017.
- [154] T. Sakamoto, A. Oichi, T. Nishimura, A. Sugawara, and T. Kato, "Calcium carbonate/ polymer thin-film hybrids: induction of the formation of patterned aragonite crystals by thermal treatment of a polymer matrix," *Polymer Journal*, vol. 41, no. 7, pp. 522–523, 2009.
- [155] A. Finnemore, P. Cunha, T. Shean, S. Vignolini, S. Guldin, M. Oyen, and U. Steiner, "Biomimetic layer-by-layer assembly of artificial nacre," *Nature Communications*, vol. 3, Jan. 2012.
- [156] J. Xiao and S. Yang, "Bio-inspired synthesis: understanding and exploitation of the crystallization process from amorphous precursors," *Nanoscale*, vol. 4, no. 1, pp. 54–65, 2012.

Bibliography

- [157] E. Loste, R. M. Wilson, R. Seshadri, and F. C. Meldrum, "The role of magnesium in stabilising amorphous calcium carbonate and controlling calcite morphologies," *Journal of Crystal Growth*, vol. 254, pp. 206–218, June 2003.
- [158] B. Purgstaller, V. Mavromatis, A. Immenhauser, and M. Dietzel, "Transformation of Mg-bearing amorphous calcium carbonate to Mg-calcite – *In situ* monitoring," *Geochimica et Cosmochimica Acta*, vol. 174, pp. 180–195, Feb. 2016.
- [159] C. Blue, A. Giuffrè, S. Mergelsberg, N. Han, J. De Yoreo, and P. Dove, "Chemical and physical controls on the transformation of amorphous calcium carbonate into crystalline CaCO_3 polymorphs," *Geochimica et Cosmochimica Acta*, vol. 196, pp. 179–196, Jan. 2017.
- [160] H. Yang, S. Chai, Y. Zhang, and Y. Ma, "A study on the influence of sodium carbonate concentration on the synthesis of high Mg calcites," *CrystEngComm*, vol. 18, pp. 157–163, Dec. 2015.
- [161] A. V. Radha, A. Fernandez-Martinez, Y. Hu, Y.-S. Jun, G. A. Waychunas, and A. Navrotsky, "Energetic and structural studies of amorphous $\text{Ca}_{1-x}\text{Mg}_x\text{CO}_3 \cdot n\text{H}_2\text{O}$ ($0 \leq x \leq 1$)," *Geochimica et Cosmochimica Acta*, vol. 90, pp. 83–95, Aug. 2012.
- [162] R. M. Noyes, "Thermodynamics of ion hydration as a measure of effective dielectric properties of water," *Journal of the American Chemical Society*, vol. 84, pp. 513–522, Feb. 1962.
- [163] A. Mucci and J. W. Morse, "The incorporation of Mg^{2+} and Sr^{2+} into calcite overgrowths: influences of growth rate and solution composition," *Geochimica et Cosmochimica Acta*, vol. 47, pp. 217–233, Feb. 1983.
- [164] Z. Zhang, Y. Xie, X. Xu, H. Pan, and R. Tang, "Transformation of amorphous calcium carbonate into aragonite," *Journal of Crystal Growth*, vol. 343, pp. 62–67, Mar. 2012.
- [165] A. Koishi, A. Fernandez-Martinez, B. Ruta, M. Jimenez-Ruiz, R. Poloni, D. di Tommaso, F. Zontone, G. A. Waychunas, and G. Montes-Hernandez, "Role of impurities in the kinetic persistence of amorphous calcium carbonate: a nanoscopic dynamics view," *The Journal of Physical Chemistry C*, vol. 122, pp. 16983–16991, July 2018.
- [166] E. Dimasi, S. Y. Kwak, F. F. Amos, M. J. Olszta, D. Lush, and L. B. Gower, "Complementary control by additives of the kinetics of amorphous CaCO_3 mineralization at an organic interface: *in-situ* synchrotron X-ray observations," *Physical Review Letters*, vol. 97, no. 4, p. 45503, 2006.

- [167] J. Jiang, M.-R. Gao, Y.-H. Qiu, and S.-H. Yu, "Gram-scale, low-cost, rapid synthesis of highly stable Mg-ACC nanoparticles and their long-term preservation," *Nanoscale*, vol. 2, pp. 2358–2361, Nov. 2010.
- [168] S.-Y. Yang, H.-H. Chang, C.-J. Lin, S.-J. Huang, and J. C. C. Chan, "Is Mg-stabilized amorphous calcium carbonate a homogeneous mixture of amorphous magnesium carbonate and amorphous calcium carbonate?," *Chemical Communications*, vol. 52, no. 77, pp. 11527–11530, 2016.
- [169] D. D. Tommaso and N. H. d. Leeuw, "Structure and dynamics of the hydrated magnesium ion and of the solvated magnesium carbonates: insights from first principles simulations," *Physical Chemistry Chemical Physics*, vol. 12, pp. 894–901, Jan. 2010.
- [170] Z. Zou, I. Polishchuk, L. Bertinetti, B. Pokroy, Y. Politi, P. Fratzl, and W. J. E. M. Habraken, "Additives influence the phase behavior of calcium carbonate solution by a cooperative ion-association process," *Journal of Materials Chemistry B*, vol. 6, no. 3, pp. 449–457, 2018.
- [171] Y. Politi, D. R. Batchelor, P. Zaslansky, B. F. Chmelka, J. C. Weaver, I. Sagi, S. Weiner, and L. Addadi, "Role of magnesium ion in the stabilization of biogenic amorphous calcium carbonate: a structure function investigation," *Chemistry of Materials*, vol. 22, pp. 161–166, Jan. 2010.
- [172] J. D. Rodriguez-Blanco, S. Shaw, P. Bots, T. Roncal-Herrero, and L. G. Benning, "The role of Mg in the crystallization of monohydrocalcite," *Geochimica et Cosmochimica Acta*, vol. 127, Feb.
- [173] P.-T. Yu, C. Tsao, C.-C. Wang, C.-Y. Chang, C.-H. Wang, and J. C. C. Chan, "High-magnesium calcite mesocrystals: formation in aqueous solution under ambient conditions," *Angewandte Chemie International Edition*, vol. 56, pp. 16202–16206, Dec. 2017.
- [174] M. E. Kunitake, S. P. Baker, and L. A. Estroff, "The effect of magnesium substitution on the hardness of synthetic and biogenic calcite," *MRS Communications*, vol. 2, pp. 113–116, Sept. 2012.
- [175] C.-J. Lin, S.-Y. Yang, S.-J. Huang, and J. C. C. Chan, "Structural characterization of mg-stabilized amorphous calcium carbonate by mg-25 solid-state nmr NMR spectroscopy," *The Journal of Physical Chemistry C*, vol. 119, pp. 7225–7233, Apr. 2015.
- [176] D. J. Tobler, J. D. Rodriguez-Blanco, K. Dideriksen, N. Bovet, K. K. Sand, and S. L. S. Stipp, "Citrate effects on amorphous calcium carbonate (ACC) structure,

Bibliography

- stability, and crystallization,” *Advanced Functional Materials*, vol. 25, pp. 3081–3090, May 2015.
- [177] D. J. Tobler, J. D. R. Blanco, K. Dideriksen, K. K. Sand, N. Bovet, L. G. Benning, and S. L. S. Stipp, “The effect of aspartic acid and glycine on amorphous calcium carbonate (ACC) structure, stability and crystallization,” *Procedia Earth and Planetary Science*, vol. 10, pp. 143–148, Jan. 2014.
- [178] D. C. Green, J. Ihli, Y.-Y. Kim, S. Y. Chong, P. A. Lee, C. J. Empson, and F. C. Meldrum, “Rapid screening of calcium carbonate precipitation in the presence of amino acids: kinetics, structure, and composition,” *Crystal Growth & Design*, vol. 16, pp. 5174–5183, Sept. 2016.
- [179] W. Jiang, M. S. Pacella, D. Athanasiadou, V. Nelea, H. Vali, R. M. Hazen, J. J. Gray, and M. D. McKee, “Chiral acidic amino acids induce chiral hierarchical structure in calcium carbonate,” *Nature Communications*, vol. 8, p. 15066, Apr. 2017.
- [180] A.-W. Xu, Q. Yu, W.-F. Dong, M. Antonietti, and H. Cölfen, “Stable amorphous CaCO_3 microparticles with hollow spherical superstructures stabilized by phytic acid,” *Advanced Materials*, vol. 17, pp. 2217–2221, Sept. 2005.
- [181] S. Bentov, S. Weil, L. Glazer, A. Sagi, and A. Berman, “Stabilization of amorphous calcium carbonate by phosphate rich organic matrix proteins and by single phosphoamino acids,” *Journal of Structural Biology*, vol. 171, pp. 207–215, Aug. 2010.
- [182] L. Plant and W. House, “Precipitation of calcite in the presence of inorganic phosphate,” *Colloids and Surfaces A: Physicochemical and Engineering Aspects*, vol. 203, pp. 143–153, Apr. 2002.
- [183] H. J. Meyer, “The influence of impurities on the growth rate of calcite,” *Journal of Crystal Growth*, vol. 66, pp. 639–646, May 1984.
- [184] G. Montanari, L. Z. Lakshtanov, D. J. Tobler, K. Dideriksen, K. N. Dalby, N. Bovet, and S. L. S. Stipp, “Effect of aspartic acid and glycine on calcite growth,” *Crystal Growth & Design*, vol. 16, pp. 4813–4821, Sept. 2016.
- [185] C. Orme, A. Noy, A. Wierzbicki, M. T. McBride, M. Grantham, H. Teng, P. Dove, and J. DeYoreo, “Formation of chiral morphologies through selective binding of amino acids to calcite surface steps,” *Nature*, vol. 411, pp. 775–779, June 2001.
- [186] G. Montanari, J. D. Rodriguez-Blanco, N. Bovet, S. L. S. Stipp, and D. J. Tobler, “Impact of citrate ions on the nucleation and growth of anhydrous CaCO_3 ,” *Crystal Growth & Design*, vol. 17, pp. 5269–5275, Oct. 2017.
- [187] S. Wolf, N. Loges, B. Mathiasch, M. Panthöfer, I. Mey, A. Janshoff, and W. Tremel,

- “Phase selection of calcium carbonate through the chirality of adsorbed amino acids,” *Angewandte Chemie International Edition*, vol. 46, pp. 5618–5623, July 2007.
- [188] S. Sun, L.-B. Mao, Z. Lei, S.-H. Yu, and H. Cölfen, “Hydrogels from amorphous calcium carbonate and polyacrylic acid: bio-inspired materials for ‘mineral plastics’,” *Angewandte Chemie International Edition*, vol. 55, pp. 11765–11769, Sept. 2016.
- [189] D. J. Schupp, X. Zhang, S. Sun, and H. Cölfen, “Mineral plastic hydrogels from the cross-linking of polyacrylic acid and alkaline earth or transition metal ions,” *Chemical Communications*, vol. 55, pp. 4913–4916, Apr. 2019.
- [190] M. Kellermeier, E. Melero-García, F. Glaab, R. Klein, M. Drechsler, R. Rachel, J. M. García-Ruiz, and W. Kunz, “Stabilization of amorphous calcium carbonate in inorganic silica-rich environments,” *Journal of the American Chemical Society*, vol. 132, pp. 17859–17866, Dec. 2010.
- [191] T. Wang, M. Antonietti, and H. Cölfen, “Calcite mesocrystals: ‘morphing’ crystals by a polyelectrolyte,” *Chemistry – A European Journal*, vol. 12, no. 22, pp. 5722–5730, 2006.
- [192] B. Cantaert, Y.-Y. Kim, H. Ludwig, F. Nudelman, N. A. J. M. Sommerdijk, and F. C. Meldrum, “Think positive: phase separation enables a positively charged additive to induce dramatic changes in calcium carbonate morphology,” *Advanced Functional Materials*, vol. 22, pp. 907–915, Mar. 2012.
- [193] V. Dmitrovic, G. J. M. Habraken, M. M. R. M. Hendrix, W. J. E. M. Habraken, A. Heise, G. De With, and N. A. J. M. Sommerdijk, “Random poly(amino acid)s synthesized by ring opening polymerization as additives in the biomimetic mineralization of CaCO_3 ,” *Polymers*, vol. 4, pp. 1195–1210, June 2012.
- [194] A. Rao, P. Vásquez-Quitral, M. S. Fernández, J. K. Berg, M. Sánchez, M. Drechsler, A. Neira-Carrillo, J. L. Arias, D. Gebauer, and H. Cölfen, “pH-dependent schemes of calcium carbonate formation in the presence of alginates,” *Crystal Growth & Design*, vol. 16, pp. 1349–1359, Mar. 2016.
- [195] E. Weber, I. M. Weiss, H. Cölfen, and M. Kellermeier, “Recombinant perlucin derivatives influence the nucleation of calcium carbonate,” *CrystEngComm*, vol. 18, no. 43, pp. 8439–8444, 2016.
- [196] Z. Zou, L. Bertinetti, Y. Politi, P. Fratzl, and W. J. E. M. Habraken, “Control of polymorph selection in amorphous calcium carbonate crystallization by poly(aspartic acid): two different mechanisms,” *Small*, vol. 13, p. 1603100, June 2017.

- 2017.
- [197] M. Kellermeier, D. Gebauer, E. Melero-García, M. Drechsler, Y. Talmon, L. Kienle, H. Cölfen, J. M. García-Ruiz, and W. Kunz, "Colloidal stabilization of calcium carbonate prenucleation clusters with silica," *Advanced Functional Materials*, vol. 22, pp. 4301–4311, Oct. 2012.
 - [198] S. Elhadj, E. A. Salter, A. Wierzbicki, J. J. De Yoreo, N. Han, and P. M. Dove, "Peptide controls on calcite mineralization: polyaspartate chain length affects growth kinetics and acts as a stereochemical switch on morphology," *Crystal Growth & Design*, vol. 6, pp. 197–201, Jan. 2006.
 - [199] T. Wang, H. Cölfen, and M. Antonietti, "Nonclassical crystallization: mesocrystals and morphology change of CaCO_3 crystals in the presence of a polyelectrolyte additive," *Journal of the American Chemical Society*, vol. 127, pp. 3246–3247, Mar. 2005.
 - [200] S. L. P. Wolf, K. Jähme, and D. Gebauer, "Synergy of Mg^{2+} and poly(aspartic acid) in additive-controlled calcium carbonate precipitation," *CrystEngComm*, vol. 17, no. 36, pp. 6857–6862, 2015.
 - [201] D. Wang, A. F. Wallace, J. J. De Yoreo, and P. M. Dove, "Carboxylated molecules regulate magnesium content of amorphous calcium carbonates during calcification," *Proceedings of the National Academy of Sciences*, vol. 106, pp. 21511–21516, Dec. 2009.
 - [202] Y. Ma, S. R. Cohen, L. Addadi, and S. Weiner, "Sea urchin tooth design: an 'all-calcite' polycrystalline reinforced fiber composite for grinding rocks," *Advanced Materials*, vol. 20, pp. 1555–1559, Apr. 2008.
 - [203] N. Hosoda and T. Kato, "Thin-film formation of calcium carbonate crystals: effects of functional groups of matrix polymers," *Chemistry of Materials*, vol. 13, pp. 688–693, Feb. 2001.
 - [204] A. Sugawara, T. Ishii, and T. Kato, "Self-organized calcium carbonate with regular surface-relief structures," *Angewandte Chemie*, vol. 115, pp. 5457–5461, Nov. 2003.
 - [205] A. Sugawara and T. Kato, "Aragonite CaCO_3 thin-film formation by cooperation of Mg^{2+} and organic polymer matrices," *Chemical Communications*, no. 6, pp. 487–488, 2000.
 - [206] J. K. Berg, T. Jordan, Y. Binder, H. G. Börner, and D. Gebauer, " Mg^{2+} tunes the wettability of liquid precursors of CaCO_3 : toward controlling mineralization sites in hybrid materials," *Journal of the American Chemical Society*, vol. 135,

- pp. 12512–12515, Aug. 2013.
- [207] T. Kato, A. Sugawara, and N. Hosoda, “Calcium carbonate-organic hybrid materials,” *Advanced Materials*, vol. 14, p. 869, June 2002.
- [208] T. Kato, “Polymer/calcium carbonate layered thin-film composites,” *Advanced Materials*, vol. 12, pp. 1543–1546, Oct. 2000.
- [209] T. Kato, T. Suzuki, T. Amamiya, T. Irie, M. Komiyama, and H. Yui, “Effects of macromolecules on the crystallization of CaCO_3 the formation of organic/inorganic composites,” *Supramolecular Science*, vol. 5, pp. 411–415, July 1998.
- [210] T. Sakamoto, A. Oichi, Y. Oaki, T. Nishimura, A. Sugawara, and T. Kato, “Three-dimensional relief structures of CaCO_3 crystal assemblies formed by spontaneous two-step crystal growth on a polymer thin film,” *Crystal Growth & Design*, vol. 9, pp. 622–625, Jan. 2009.
- [211] H. Zhang, J. J. De Yoreo, and J. F. Banfield, “A unified description of attachment-based crystal growth,” *ACS Nano*, vol. 8, pp. 6526–6530, July 2014.
- [212] Y. Han, T. Nishimura, and T. Kato, “Morphology tuning in the formation of vaterite crystal thin films with thermoresponsive poly(N-isopropylacrylamide) brush matrices,” *CrystEngComm*, vol. 16, pp. 3540–3547, Feb. 2014.
- [213] S. Matsumura, S. Kajiyama, T. Nishimura, and T. Kato, “Chitin: formation of helically structured chitin/ CaCO_3 hybrids through an approach inspired by the biomineralization processes of crustacean cuticles,” *Small*, vol. 11, pp. 5126–5126, Oct. 2015.
- [214] A. S. Schenk, E. J. Albarracin, Y.-Y. Kim, J. Ihli, and F. C. Meldrum, “Confinement stabilises single crystal vaterite rods,” *Chem. Commun.*, vol. 50, no. 36, pp. 4729–4732, 2014.
- [215] S. Tugulu, M. Harms, M. Fricke, D. Volkmer, and H.-A. Klok, “Polymer brushes as ionotropic matrices for the directed fabrication of microstructured calcite thin films,” *Angewandte Chemie International Edition*, vol. 45, no. 44, pp. 7458–7461, 2006.
- [216] B. Yeom and K. Char, “Nanostructured CaCO_3 thin films formed on the urease multilayers prepared by the layer-by-layer deposition,” *Chemistry of Materials*, vol. 22, no. 1, pp. 101–107, 2009.
- [217] D. C. Popescu, E. N. van Leeuwen, N. A. Rossi, S. J. Holder, J. A. Jansen, and N. A. Sommerdijk, “Shaping amorphous calcium carbonate films into 2d model substrates for bone cell culture,” *Angewandte Chemie International Edition*, vol. 45, no. 11, pp. 1762–1767, 2006.

Bibliography

- [218] R. J. Park and F. C. Meldrum, "Synthesis of single crystals of calcite with complex morphologies," *Advanced Materials*, vol. 14, no. 16, pp. 1167–1169, 2002.
- [219] X. Cheng and L. B. Gower, "Molding mineral within microporous hydrogels by a polymer-induced liquid-precursor (PILP) process," *Biotechnology progress*, vol. 22, no. 1, pp. 141–149, 2006.
- [220] A. S. Finnnemore, M. R. Scherer, R. Langford, S. Mahajan, S. Ludwigs, F. C. Meldrum, and U. Steiner, "Nanostructured calcite single crystals with gyroid morphologies," *Advanced Materials*, vol. 21, no. 38-39, pp. 3928–3932, 2009.
- [221] S. Matsumura, S. Kajiyama, T. Nishimura, and T. Kato, "Formation of helically structured chitin/CaCO₃ hybrids through an approach inspired by the biomineralization processes of crustacean cuticles," *Small*, vol. 11, pp. 5127–5133, Oct. 2015.
- [222] N. Gehrke, N. Nassif, N. Pinna, M. Antonietti, H. S. Gupta, and H. Cölfen, "Retrosynthesis of Nacre via Amorphous Precursor Particles," *Chemistry of Materials*, vol. 17, pp. 6514–6516, Dec. 2005.
- [223] C. J. Stephens, Y.-Y. Kim, S. D. Evans, F. C. Meldrum, and H. K. Christenson, "Early stages of crystallization of calciumcarbonate revealed in picoliter droplets," *Journal of the American Chemical Society*, vol. 133, pp. 5210–5213, Apr. 2011.
- [224] M. L. Whittaker, P. M. Dove, and D. Joester, "Nucleation on surfaces and in confinement," *MRS Bulletin*, vol. 41, pp. 388–392, May 2016.
- [225] H. Du, M. Steinacher, C. Borca, T. Huthwelker, A. Murello, F. Stellacci, and E. Amstad, "Amorphous CaCO₃: influence of the formation time on its degree of hydration and stability," *Journal of the American Chemical Society*, vol. 140, pp. 14289–14299, Oct. 2018.
- [226] H. Du, C. Courrégelongue, J. Xto, A. Böhlen, M. Steinacher, C. Borca, T. Huthwelker, and E. Amstad, "Additives: Their influence on the humidity- and pressure-induced crystallization of amorphous CaCO₃," *Submitted*, 2019.
- [227] H. Du, A. Cont, M. Steinacher, and E. Amstad, "Fabrication of hexagonal-prismatic granular hydrogel sheets," *Langmuir*, vol. 34, pp. 3459–3466, Mar. 2018.
- [228] G. Etienne, M. Kessler, and E. Amstad, "Influence of fluorinated surfactant composition on the stability of emulsion drops," *Macromolecular Chemistry and Physics*, vol. 218, p. 1600365, Jan. 2017.
- [229] E. Amstad, M. Gopinadhan, C. Holtze, C. O. Osuji, M. P. Brenner, F. Spaepen, and D. A. Weitz, "Production of amorphous nanoparticles by supersonic spray-

- drying with a microfluidic nebulator,” *Science*, vol. 349, no. 6251, pp. 956–960, 2015.
- [230] Y. Xia and G. M. Whitesides, “Soft lithography,” *Annual review of materials science*, vol. 28, no. 1, pp. 153–184, 1998.
- [231] B. Ravel and M. Newville, “Athena, Artemis, Hephaestus: data analysis for X-ray absorption spectroscopy using IFEFFIT,” *Journal of synchrotron radiation*, vol. 12, no. 4, pp. 537–541, 2005.
- [232] J. L. Fulton, Y. Chen, S. M. Heald, and M. Balasubramanian, “Hydration and contact ion pairing of Ca^{2+} with Cl^- in supercritical aqueous solution,” *The Journal of chemical physics*, vol. 125, no. 9, p. 094507, 2006.
- [233] M. Ni and B. D. Ratner, “Differentiating calcium carbonate polymorphs by surface analysis techniques—an XPS and TOF-SIMS study,” *Surface and Interface Analysis*, vol. 40, no. 10, pp. 1356–1361, 2008.
- [234] M. Seah, I. Gilmore, and S. Spencer, “Quantitative XPS: I. analysis of X-ray photoelectron intensities from elemental data in a digital photoelectron database,” *Journal of Electron Spectroscopy and Related Phenomena*, vol. 120, no. 1-3, pp. 93–111, 2001.
- [235] P. Klapetek and D. Necas, “Gwyddion: an open-source software for SPM data analysis,” *Eur. J. Phys*, vol. 10, p. 181, 2012.
- [236] E. Amstad, M. Chemama, M. Eggersdorfer, L. R. Arriaga, M. P. Brenner, and D. A. Weitz, “Robust scalable high throughput production of monodisperse drops,” *Lab on a Chip*, vol. 16, no. 21, pp. 4163–4172, 2016.
- [237] K. Sand, M. Yang, E. Makovicky, D. J. Cooke, T. Hassenkam, K. Bechgaard, and S. Stipp, “Binding of ethanol on calcite: the role of the OH bond and its relevance to biomineralization,” *Langmuir*, vol. 26, no. 19, pp. 15239–15247, 2010.
- [238] K. Sand, J. D. Rodriguez-Blanco, E. Makovicky, L. G. Benning, and S. L. S. Stipp, “Crystallization of CaCO_3 in water–alcohol mixtures: spherulitic growth, polymorph stabilization, and morphology change,” *Crystal Growth & Design*, vol. 12, pp. 842–853, Feb. 2012.
- [239] A. Dey, G. de With, and N. A. J. M. Sommerdijk, “*In situ* techniques in biomimetic mineralization studies of calcium carbonate,” *Chem. Soc. Rev.*, vol. 39, no. 2, pp. 397–409, 2010.
- [240] B. P. Pichon, P. H. H. Bomans, P. M. Frederik, and N. A. J. M. Sommerdijk, “A quasi-time-resolved CryoTEM study of the nucleation of CaCO_3 under langmuir monolayers,” *Journal of the American Chemical Society*, vol. 130, pp. 4034–4040,

- Mar. 2008.
- [241] Y. Politi, Y. Levi-Kalisman, S. Raz, F. Wilt, L. Addadi, S. Weiner, and I. Sagi, "Structural characterization of the transient amorphous calcium carbonate precursor phase in sea urchin embryos," *Advanced Functional Materials*, vol. 16, no. 10, pp. 1289–1298, 2006.
 - [242] H. Hu and R. G. Larson, "Evaporation of a Sessile Droplet on a Substrate," *The Journal of Physical Chemistry B*, vol. 106, pp. 1334–1344, Feb. 2002.
 - [243] R. D. Deegan, O. Bakajin, T. F. Dupont, G. Huber, S. R. Nagel, and T. A. Witten, "Capillary flow as the cause of ring stains from dried liquid drops," *Nature*, vol. 389, no. 6653, p. 827, 1997.
 - [244] J. Rodriguez-Blanco, S. Shaw, and L. Benning, "How to make 'stable' ACC: protocol and preliminary structural characterization," *Mineralogical Magazine*, vol. 72, no. 1, pp. 283–286, 2008.
 - [245] J. M. Grogan, N. M. Schneider, F. M. Ross, and H. H. Bau, "Bubble and pattern formation in liquid induced by an electron beam," *Nano letters*, vol. 14, no. 1, pp. 359–364, 2013.
 - [246] C. Rodriguez-Navarro, E. Ruiz-Agudo, A. Luque, A. B. Rodriguez-Navarro, and M. Ortega-Huertas, "Thermal decomposition of calcite: mechanisms of formation and textural evolution of CaO nanocrystals," *American Mineralogist*, vol. 94, no. 4, pp. 578–593, 2009.
 - [247] C. G. Sinn, R. Dimova, and M. Antonietti, "Isothermal titration calorimetry of the polyelectrolyte/water interaction and binding of Ca^{2+} : effects determining the quality of polymeric scale inhibitors," *Macromolecules*, vol. 37, pp. 3444–3450, May 2004.
 - [248] S. Raz, P. C. Hamilton, F. H. Wilt, S. Weiner, and L. Addadi, "The transient phase of amorphous calcium carbonate in sea urchin larval spicules: the involvement of proteins and magnesium ions in its formation and stabilization," *Advanced Functional Materials*, vol. 13, no. 6, pp. 480–486, 2003.
 - [249] A. S. Schenk, B. Cantaert, Y.-Y. Kim, Y. Li, E. S. Read, M. Semsarilar, S. P. Armes, and F. C. Meldrum, "Systematic study of the effects of polyamines on calcium carbonate precipitation," *Chemistry of Materials*, vol. 26, pp. 2703–2711, Apr. 2014.
 - [250] C. Ruiz-Agudo, J. Lutz, P. Keckeis, M. King, A. Marx, and D. Gebauer, "Ubiquitin designer proteins as a new additive generation toward controlling crystallization," *Journal of the American Chemical Society*, p. jacs.9b06473, July 2019.

- [251] A. Rao, M. Drechsler, S. Schiller, M. Scheffner, D. Gebauer, and H. Cölfen, "Stabilization of mineral precursors by intrinsically disordered proteins," *Advanced Functional Materials*, vol. 28, p. 1802063, Sept. 2018.
- [252] S.-C. Huang, K. Naka, and Y. Chujo, "Effect of molecular weights of poly(acrylic acid) on crystallization of calcium carbonate by the delayed addition method," *Polymer Journal*, vol. 40, pp. 154–162, Feb. 2008.
- [253] M. Jehannin, A. Rao, and H. Cölfen, "New horizons of non-classical crystallization," *Journal of the American Chemical Society*, June 2019.
- [254] Y. Politi, J. Mahamid, H. Goldberg, S. Weiner, and L. Addadi, "Asprich mollusk shell protein: in vitro experiments aimed at elucidating function in CaCO_3 crystallization," *CrystEngComm*, vol. 9, no. 12, p. 1171, 2007.
- [255] M. J. Olszta, X. Cheng, S. S. Jee, R. Kumar, Y.-Y. Kim, M. J. Kaufman, E. P. Douglas, and L. B. Gower, "Bone structure and formation: a new perspective," *Materials Science and Engineering: R: Reports*, vol. 58, pp. 77–116, Nov. 2007.
- [256] Y. Li, T. T. Thula, S. Jee, S. L. Perkins, C. Aparicio, E. P. Douglas, and L. B. Gower, "Biomimetic mineralization of woven bone-like nanocomposites: role of collagen cross-links," *Biomacromolecules*, vol. 13, pp. 49–59, Jan. 2012.
- [257] G. M. Whitesides and B. Grzybowski, "Self-assembly at all scales," *Science*, vol. 295, no. 5564, pp. 2418–2421, 2002.
- [258] N. Vogel, M. Retsch, C. A. Fustin, A. Del Campo, and U. Jonas, "Advances in colloidal assembly: the design of structure and hierarchy in two and three dimensions," *Chemical Reviews*, vol. 115, no. 13, pp. 6265–6311, 2015.
- [259] L. A. Lyon, J. D. Debord, S. B. Debord, C. D. Jones, J. G. McGrath, and M. J. Serpe, "Microgel colloidal crystals," *The Journal of Physical Chemistry B*, vol. 108, no. 50, pp. 19099–19108, 2004.
- [260] J. D. Debord and L. A. Lyon, "Thermoresponsive photonic crystals," *The Journal of Physical Chemistry B*, vol. 104, no. 27, pp. 6327–6331, 2000.
- [261] S. Schmidt, T. Hellweg, and R. von Klitzing, "Packing density control in Poly(NIPAM-co-AAc) microgel monolayers: effect of surface charge, pH, and preparation technique," *Langmuir*, vol. 24, no. 21, pp. 12595–12602, 2008.
- [262] G. Zhang, D. Wang, Z.-Z. Gu, J. Hartmann, and H. Möhwald, "Two-dimensional non-close-packing arrays derived from self-assembly of biomineralized hydrogel spheres and their patterning applications," *Chemistry of materials*, vol. 17, no. 21, pp. 5268–5274, 2005.
- [263] D. Suzuki, J. G. McGrath, H. Kawaguchi, and L. A. Lyon, "Colloidal crystals of

- thermosensitive, core/shell hybrid microgels,” *The Journal of Physical Chemistry C*, vol. 111, no. 15, pp. 5667–5672, 2007.
- [264] J. Zhou, G. Wang, M. Marquez, and Z. Hu, “The formation of crystalline hydrogel films by self-crosslinking microgels,” *Soft Matter*, vol. 5, no. 4, pp. 820–826, 2009.
- [265] B. Zhou, J. Gao, and Z. Hu, “Robust polymer gel opals—an easy approach by inter-sphere cross-linking gel nanoparticle assembly in acetone,” *Polymer*, vol. 48, no. 10, pp. 2874–2881, 2007.
- [266] Z. Hu, X. Lu, and J. Gao, “Hydrogel opals,” *Advanced Materials*, vol. 13, no. 22, pp. 1708–1712, 2001.
- [267] G. Huang and Z. Hu, “Phase behavior and stabilization of microgel arrays,” *Macromolecules*, vol. 40, no. 10, pp. 3749–3756, 2007.
- [268] E. C. Cho, J.-W. Kim, A. Fernández-Nieves, and D. A. Weitz, “Highly responsive hydrogel scaffolds formed by three-dimensional organization of microgel nanoparticles,” *Nano letters*, vol. 8, no. 1, pp. 168–172, 2008.
- [269] E. C. Cho, J.-W. Kim, D. C. Hyun, U. Jeong, and D. A. Weitz, “Regulating volume transitions of highly responsive hydrogel scaffolds by adjusting the network properties of microgel building block colloids,” *Langmuir*, vol. 26, no. 6, pp. 3854–3859, 2010.
- [270] M. Kumoda, M. Watanabe, and Y. Takeoka, “Preparations and optical properties of ordered arrays of submicron gel particles: interconnected state and trapped state,” *Langmuir*, vol. 22, no. 9, pp. 4403–4407, 2006.
- [271] R. Liu, A. H. Milani, T. J. Freemont, and B. R. Saunders, “Doubly crosslinked ph-responsive microgels prepared by particle inter-penetration: swelling and mechanical properties,” *Soft Matter*, vol. 7, no. 10, pp. 4696–4704, 2011.
- [272] R. Liu, J. M. Saunders, T. J. Freemont, and B. R. Saunders, “Doubly crosslinked microgel–polyelectrolyte complexes: three simple methods to tune and improve gel mechanical properties,” *Soft Matter*, vol. 8, no. 42, pp. 10932–10940, 2012.
- [273] T. Lane, J. L. Holloway, A. H. Milani, J. M. Saunders, A. J. Freemont, and B. R. Saunders, “Double network hydrogels prepared from ph-responsive doubly crosslinked microgels,” *Soft Matter*, vol. 9, no. 33, pp. 7934–7941, 2013.
- [274] S. Tsuji and H. Kawaguchi, “Self-assembly of poly(N-isopropylacrylamide)-carrying microspheres into two-dimensional colloidal arrays,” *Langmuir*, vol. 21, no. 6, pp. 2434–2437, 2005.
- [275] L.-W. Xia, R. Xie, X.-J. Ju, W. Wang, Q. Chen, and L.-Y. Chu, “Nano-structured smart hydrogels with rapid response and high elasticity,” *Nature communica-*

- tions, vol. 4, p. 2226, 2013.
- [276] N. D. Denkov, O. D. Velev, P. A. Kralchevsky, I. B. Ivanov, H. Yoshimura, and K. Nagayama, "Two-dimensional crystallization," *Nature*, vol. 361, no. 6407, pp. 26–26, 1993.
- [277] Y. Xia, B. Gates, Y. Yin, and Y. Lu, "Monodispersed colloidal spheres: old materials with new applications," *Advanced Materials*, vol. 12, no. 10, pp. 693–713, 2000.
- [278] Y. Liu, S. Wang, J. W. Lee, and N. A. Kotov, "A floating self-assembly route to colloidal crystal templates for 3D cell scaffolds," *Chemistry of Materials*, vol. 17, no. 20, pp. 4918–4924, 2005.
- [279] Z. Cai, J.-T. Zhang, F. Xue, Z. Hong, D. Punihaole, and S. A. Asher, "2D photonic crystal protein hydrogel coulometer for sensing serum albumin ligand binding," *Analytical chemistry*, vol. 86, no. 10, pp. 4840–4847, 2014.
- [280] Z. Cai, D. H. Kwak, D. Punihaole, Z. Hong, S. S. Velankar, X. Liu, and S. A. Asher, "A photonic crystal protein hydrogel sensor for candida albicans," *Angewandte Chemie International Edition*, vol. 54, no. 44, pp. 13036–13040, 2015.
- [281] T. Nisisako and T. Hatsuzawa, "A microfluidic cross-flowing emulsion generator for producing biphasic droplets and anisotropically shaped polymer particles," *Microfluidics and Nanofluidics*, vol. 9, no. 2-3, pp. 427–437, 2010.
- [282] Z. Drira and V. K. Yadavalli, "Nanomechanical measurements of polyethylene glycol hydrogels using atomic force microscopy," *Journal of the mechanical behavior of biomedical materials*, vol. 18, pp. 20–28, 2013.
- [283] P. F. Becher, "Microstructural design of toughened ceramics," *Journal of the American Ceramic Society*, vol. 74, no. 2, pp. 255–269, 1991.
- [284] R. W. Rice, S. W. Freiman, and P. F. Becher, "Grain-size dependence of fracture energy in ceramics: I, experiment," *Journal of the American ceramic society*, vol. 64, no. 6, pp. 345–350, 1981.
- [285] L. Manukyan, S. A. Montandon, A. Fofonjka, S. Smirnov, and M. C. Milinkovitch, "A living mesoscopic cellular automaton made of skin scales," *Nature*, vol. 544, pp. 173–179, Apr. 2017.
- [286] W. J. E. M. Habraken, J. Tao, L. J. Brylka, H. Friedrich, L. Bertinetti, A. S. Schenk, A. Verch, V. Dmitrovic, P. H. H. Bomans, P. M. Frederik, J. Laven, P. van der Schoot, B. Aichmayer, G. de With, J. J. DeYoreo, and N. A. J. M. Sommerdijk, "Ion-association complexes unite classical and non-classical theories for the biomimetic nucleation of calcium phosphate," *Nature Communications*, vol. 4,

Dec. 2013.

- [287] F. Nudelman, K. Pieterse, A. George, P. H. Bomans, H. Friedrich, L. J. Brylka, P. A. Hilbers, G. de With, and N. A. Sommerdijk, "The role of collagen in bone apatite formation in the presence of hydroxyapatite nucleation inhibitors," *Nature materials*, vol. 9, no. 12, p. 1004, 2010.
- [288] E. Ruiz-Agudo, A. Burgos-Cara, C. Ruiz-Agudo, A. Ibañez-Velasco, H. Cölfen, and C. Rodriguez-Navarro, "A non-classical view on calcium oxalate precipitation and the role of citrate," *Nature communications*, vol. 8, no. 1, p. 768, 2017.
- [289] J. Ihli, Y.-W. Wang, B. Cantaert, Y.-Y. Kim, D. C. Green, P. H. Bomans, N. A. Sommerdijk, and F. C. Meldrum, "Precipitation of amorphous calcium oxalate in aqueous solution," *Chemistry of Materials*, vol. 27, no. 11, pp. 3999–4007, 2015.
- [290] Y.-W. Wang, Y.-Y. Kim, H. K. Christenson, and F. C. Meldrum, "A new precipitation pathway for calcium sulfate dihydrate (gypsum) via amorphous and hemihydrate intermediates," *Chemical Communications*, vol. 48, no. 4, pp. 504–506, 2012.
- [291] A. Saha, J. Lee, S. M. Pancera, M. F. Bräeu, A. Kempter, A. Tripathi, and A. Bose, "New insights into the transformation of calcium sulfate hemihydrate to gypsum using time-resolved cryogenic transmission electron microscopy," *Langmuir*, vol. 28, no. 30, pp. 11182–11187, 2012.
- [292] K. Yanagisawa and J. Ovenstone, "Crystallization of anatase from amorphous titania using the hydrothermal technique: effects of starting material and temperature," *The Journal of Physical Chemistry B*, vol. 103, no. 37, pp. 7781–7787, 1999.
- [293] E. Ylhäinen, M. Nunes, A. Silvestre, and O. Monteiro, "Synthesis of titanate nanostructures using amorphous precursor material and their adsorption/photocatalytic properties," *Journal of Materials Science*, vol. 47, no. 10, pp. 4305–4312, 2012.
- [294] C. C. Carcouët, M. W. Van De Put, B. Mezari, P. C. Magusin, J. Laven, P. H. Bomans, H. Friedrich, A. C. C. Esteves, N. A. Sommerdijk, R. A. Van Benthem, *et al.*, "Nucleation and growth of monodisperse silica nanoparticles," *Nano letters*, vol. 14, no. 3, pp. 1433–1438, 2014.
- [295] A. E. Van Driessche, M. Kellermeier, L. G. Benning, and D. Gebauer, *New perspectives on mineral nucleation and growth: from solution precursors to solid materials*. Springer, 2016.

- [296] S. Sun, D. Gebauer, and H. Cölfen, “Alignment of amorphous iron oxide clusters: a non-classical mechanism for magnetite formation,” *Angewandte Chemie International Edition*, vol. 56, no. 14, pp. 4042–4046, 2017.

Bibliography
